A Magneto-Optic Investigation Of Flux Penetration In High Temperature Superconductors.

by

Michael W. Gardner

M.Sc., University of British Columbia, 1994
B.Sc.(hons.), Simon Fraser Univsersity, 1991

A DISSERTATION SUBMITTED IN PARTIAL FULFILLMENT OF
THE REQUIREMENTS FOR THE DEGREE OF

Doctor of Philosophy

in

THE FACULTY OF GRADUATE STUDIES

(Department of Physics & Astronomy)

We accept this dissertation as conforming
to the required standard

THE UNIVERSITY OF BRITISH COLUMBIA

Nov 1999

In presenting this thesis in partial fulfilment of the requirements for an advanced degree at the University of British Columbia, I agree that the Library shall make it freely available for reference and study. I further agree that permission for extensive copying of this thesis for scholarly purposes may be granted by the head of my department or by his or her representatives. It is understood that copying or publication of this thesis for financial gain shall not be allowed without my written permission.

Department of _physics & astronomy_

The University of British Columbia
Vancouver, Canada

Date _April 27 2000_

Abstract

An efficient non-destructive magneto-optic imaging system was developed that employs special iron-garnet indicator films to image magnetic fields in high temperature superconductors. The flexibility of the system allows the investigation of many different types of samples having different sizes and characteristics.

Two very high quality, low pinning, thin, flat $YBa_2Cu_3O_{6.95}$ single crystals are imaged using this system to observe field penetration dynamics. Slightly different pinning characteristics of both samples enable a comparison to be made between the different flux penetration dynamics observed. In one ultra low pinning crystal, penetrating flux is found to accumulate in the sample's central regions while avoiding the inner edges and in the other higher pinning crystal flux tends to initially avoid both the central regions and sample's inner edges. These results compare favourably with a theoretical model of Zeldov et al.[21] that characterizes penetration phenomenon in low pinning superconductors.

Field penetration of a $Tl_2Ba_2CaCu_2$ thin film is also observed for different sample temperatures up to the sample's superconducting transition temperature. A new computational technique is employed to calculate the critical current of the film using imaged field strengths. A comparison of the imaged fields and calculated currents is made with a theoretical model devised to characterize field penetration in superconductors having a thin circular geometry. From these results the critical current temperature dependence is established and is fitted to a simple phenomenological model. A small discontinuity in the data 10K below the sample's transition temperature is also noted and is examined.

Contents

List of Figures

Acknowledgements

I am enormously grateful to Dr. S. A. Govorkov whose work and contributions proved to be invaluable in the initial phases of this project. I would also like to thank Dr. B. Heinrich of the surface science lab at Simon Fraser University for his generosity in allowing the use of the iron-garnet films which made this project possible. I also appreciate the special contribution of Dr. R. Liang who made the very high quality superconducting crystals and Dr. D. A. Bonn for his skill at detwinning the crystals and for his contributions. I thank Dr. J. F. Carolan for being my supervisor and thank my supervising committee members, Dr. D. A. Bonn, Dr. D. Ll. Williams and Dr. B. Bergersen. In addition I would like to also acknowledge all the technicians and research associates whose help was greatly appreciated. Finally, I gratefully acknowledge the initial financial support from C.T.F. systems and the support from The Natural Sciences and Engineering Research Council of Canada through its strategic and collaborative grant programs.

MICHAEL W. GARDNER

The University of British Columbia
Nov 1999

Chapter 1

Introduction

1.1 Introduction

Superconductivity has over the years proven to be a fascinating and very rich field of science providing an impetus for a wide range of theoretical and experimental research. First discovered by H. Kamerlingh Onnes in 1911[1] it has evolved further with the discovery by Bednorz and Müller[2] in 1986 of the new and even more intriguing materials called the ceramic oxides or high temperature superconductors. These new materials have further stimulated development of novel research techniques used to study fundamental as well as practical aspects of superconductivity. One such area of research utilizes the method of field imaging which enables the direct visualization of magnetic fields that are trapped in superconducting materials. This is an especially useful branch of inquiry as it provides a means of studying phenomenon that would otherwise be difficult if not impossible to characterize with other techniques. The processes and technology used in the imaging of magnetic fields have also evolved over the years. As a result techniques vary greatly within this branch of science and can range from simple decorative processes where fine ferromagnetic particles are deposited on the surface of a superconductor[3, 4, 5, 6] to very sophisticated techniques involving the use of scanning tunneling microscopy [7, 8] and micro scanning Hall probes[9, 10, 11, 12]. Another unique system that is used to

observe dynamic processes in superconductivity utilizes the Faraday effect[13] and is called magneto-optic imaging. With this technique a magneto-optically active layer is usually placed just above a superconductor where it induces a rotation of polarized light in response to a local magnetic field. Local light intensity variations caused by viewing the rotated polarized light through a cross polarizer enables the direct observation of local field strengths. Of course there have been new developments in this technique with the introduction of new types of magneto-optic sensing materials. Early magneto-optic visualization of magnetic flux was conducted using paramagnetic glasses on both type-I[14] and type-II[15] superconductors. A refinement of this technique was accomplished with the introduction of a thin film method employing layers of europium chalcogenides[16]. With this method it is possible to get much better resolution since very thin films are used. Generally imaging resolution is limited by the thickness of the active magneto-optic layer. There are, however, certain limitations with this process. In order to enhance imaging resolution the magneto-optic layer is usually deposited directly on top of a sample which limits a superconductor's future usefulness. Another major problem with this class of imaging material is its inability to function over a wide range of temperature. The maximum temperature that these materials can perform magneto-optically is generally 20K which limits the range of experiments that can be conducted especially on the high temperature superconductors. This problem was overcome more recently by the introduction of the iron-garnet indicator films[17, 18]. It was originally proposed by A.A. Polyanskii et al.[19] that such films, which are also used in the imaging of digital information on magnetic tapes and magnetic fields produced by micromagnets, could also be used in the detection of fields trapped in high temperature superconductors. Unlike the earlier magneto-optic materials, these films remain active up to room temperature and have a high field sensitivity. In general iron-garnet films have a field sensitivity of 10μT(Tesla) while the thin film europium chalcogenides can detect fields of approximately 5mT, see [20]. The films can also be

deposited on a substrate which can then be placed directly on top of a sample. The advantage of this technique is that a garnet film can be used repeatedly for different samples and imaging is completely non-destructive. There are two different classes of iron-garnet films which are available for use in the imaging of magnetic fields. There are films that have a bubble-like domain and films that have an in-plane magnetic anisotropy. With bubble indicator films imaging resolution can be limited by the size of the bubble domains, which appear as black and white randomly distributed striped patterns. In-plane anisotropic indicator films do not have this problem and as a result have a better resolution capability. It has been discovered by the author that these films also have some limitations when they are used for imaging very weak magnetic fields. This problem and the characteristics of both types of films and their applicability to the present study is discussed further in the next chapter.

The purpose of this work is to image and study the penetration of two types of high temperature superconductors by a constant magnetic field using iron-garnet indicator films. In one case two very high quality $YBa_2Cu_3O_{6.95}$ single crystals are imaged, see chapter 4 while in the other case a high quality $Tl_2Ba_2CaCu_2O_y$ circular thin film that had been deposited on a MgO substrate is observed, see chapter 5. The single crystals were made by the superconductivity group at the University of British Columbia(UBC) while the thin film sample was commercially processed by Superconducting Technologies Incorporated of Santa Barbara California, (STI). Penetration of a high quality single crystal by a magnetic field can have some interesting characteristics that can be viewed by a field imaging system such as the one developed for this work. One such characteristic is the presence of a barrier, called a geometrical barrier, that delays the onset of flux penetration in a flat rectangular sample that has a very low degree of pinning. Pinning is an important feature of superconductors as its presence defines characteristics such as the critical current J_c and sample homogeneity. It can, however, mask certain phenomenon such as the

geometrical barrier effect. As a result in order to facilitate the observation of this phenomenon it is necessary to use superconductors that exhibit very low pinning characteristics. It is primarily due to high pinning that geometrical barrier effects have never been observed in $YBa_2Cu_3O_y$ single crystal superconductors while it has been studied, although in a limited manner, in the naturally low pinning superconductor $Bi_2Sr_2CaCu_2O_x$[21]. Through the development of very high quality single crystals of $YBa_2Cu_3O_y$ at UBC it has been possible to eliminate high pinning effects and thus, to observe for the first time the barrier effect in this material[22]. By also employing the present magneto-optic system to observe the barrier effect it has been possible to correlate experimental observations with predictions made from a theoretical model proposed by Zeldov et al.[21] that addresses the geometrical barrier effect. This model describes the phenomenon in detail for a continuum of pinning strengths, from absolutely no pinning to moderate pinning in flat superconductors having rectangular cross sections. The advantage of using $YBa_2Cu_3O_y$ for this experiment is the availability of other samples that have slightly different yet still low pinning characteristics. As a result it has also been possible for the first time, to clearly observe the barrier effect in two superconducting crystals, with one having almost no pinning and the other low pinning[22]. This has never been successfully done in the low pinning superconductor $Bi_2Sr_2CaCu_2O_x$. As a result, it has also been possible to conduct a more thorough comparison of the experimental observations of flux penetration in a thin flat superconductor with the predictions made by Zeldov et al[21]. Another important feature of the present investigation of a geometrical barrier is the ability of the imaging system to detect flux dynamics at temperatures near Tc. For the present experiment this temperature ranged from 78K to 80K. At significantly lower temperatures small defects along the edges of a superconductor tend to act as easy points of penetration for an applied field, thus destroying the geometrical barrier effect. This is because the edges of a superconductor are not easily penetrated at very low temperatures unless small defects are

present to enhance the local strength of the applied field enough to allow some penetration. At higher temperatures, magnetic fields are not as efficiently screened by a superconductor allowing a small amount of penetration along the edge regions. In this case, small edge defects no longer aid field penetration and no longer interfere with the geometrical barrier effect.

Observing field penetration of the circular thin film superconductor also provided some insights into the effect that sample geometry can have on penetrating flux dynamics when the field is applied perpendicular to the surface of such a sample. In this case the superconductor in question was thin enough to enable the modeling of local currents using a special iterative technique that is described in chapter 3. In using this technique local currents, which are assumed to be two dimensional, are calculated through iteration using experimental field values that are determined with calibrated field images. These calculated local currents were then compared with theoretical current distributions calculated using a model developed by P.N. Mikheenko et al.[23] for a circular thin film geometry. This model also predicts the degree and manner in which field penetration occurs in a circular thin film and, as a result, it is also possible to make comparisons with flux penetration observed magneto-optically in the thin film. While observations of penetration of a circular thin film have been conducted before at 4.2K with EuSe deposited directly on top of $YBa_2Cu_3O_y$[24], it was possible to take advantage of the ability of the iron-garnet films to remain active up to much higher temperatures and to observe for the first time penetration just below the superconducting transition temperature of a high quality thallium-based circular thin film. The low temperature used in the previous study was necessary since the magneto-optic material would have been only active up to very low temperatures. Certain assumptions in Mikheenko's model concerning the field dependence of the supercurrent in penetrated areas of a film are also checked using currents calculated from the magneto-optically imaged fields. Comparisons of the local currents with those expected using the model for various sample

5

temperatures are also conducted. The calculated local current strength is then used to determine the temperature dependence of the thallium film's critical current on sample temperature and is fitted to a phenomenological power law model.

Overall the system used for this research is thought to be more flexible than many imaging techniques in use today. By employing a special zoom microscope and versatile optics it was possible to observe superconductors of many different sizes. Such a task can be difficult to achieve in commercial systems that use fixed microscopic equipment. The system was also setup in such a way as to make observation of a sample a quick and efficient task. The specifications of this system are given in detail in chapter 2.

1.2 Thesis Layout

The magneto-optic system and the processing software are described in detail in chapter 2. Some of the programs used for the experiment are also listed in the appendices. In chapter 3 the iterative method used to determine local currents in the thin film superconductor is described along with a special augmented version that is specifically designed to decrease the amount of time needed to find a current solution. The results of observing flux penetration of two $YBa_2Cu_3O_{6.95}$ low pinning single crystals is discussed at length in chapter 4. Comparisons are made with a theoretical model developed by Zeldov et al.[21] that predicts the presence of a barrier to field penetration in flat very low pinning superconductors that have rectangular cross sections. A comparison between experimental observations and theoretical predictions of flux penetration is also conducted in chapter 5 for a $Tl_2Ba_2CaCu_2O_y$ circular thin film. Critical current values predicted by a model devised by Mikheenko et al.[23] for a circular thin film geometry are checked using currents calculated with the iteration described in chapter 3. The temperature dependence of the critical current of the thin film is also established using currents values calculated iteratively for different sample temperatures.

Chapter 2

Experimental Apparatus and Procedure

2.1 Experimental Apparatus

2.1.1 Garnet Indicator Films

Imaging of the magnetic fields was achieved by detecting the polarized light intensity variations produced by iron-garnet indicator films in response to local magnetic fields. In general, two types of garnet films are available, those called bubble films and those with an in-plane anisotropy[20]. With the bubble film type, observation of local fields is conducted indirectly through imaging the changes of the local domain structure. When viewed under polarized light, the domain structure of these films consists of black and white areas which change shape and size in response to a magnetic field. Depending on the direction and strength of the field, the size of either domain type increases or decreases resulting in observable polarized light intensity variations. The domains of one of the bubble films used are shown in Fig.(2.1) and the effects of applying a constant magnetic field in opposite directions can be seen in Fig.(2.2). Under normal operating conditions, where magnetic structures of interest are usually at least several microns in size, magnification of the garnet film surface is reduced, effectively causing the domains the blend together. This results in what appears to be a uniform garnet film intensity response to a sample's local fields. Alternatively, local magnetic fields can be imaged directly with ferromag-

Figure 2.1: Domain structure of a bubble iron-garnet indicator film viewed under polarized light with crossed polarizers. This view is significantly magnified to resolve the domains.
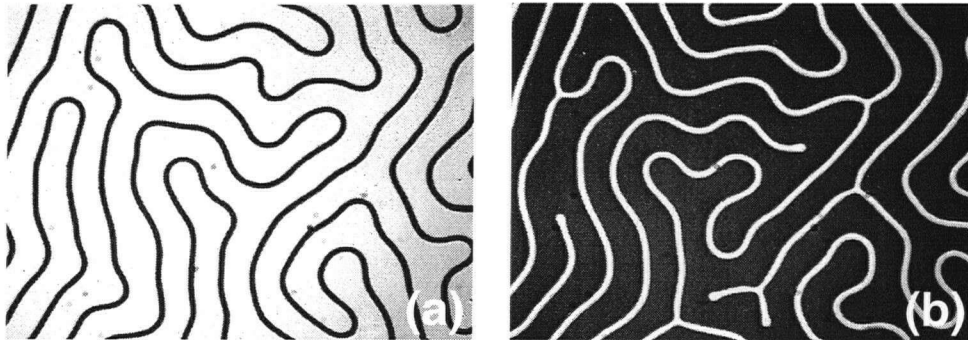
Figure 2.2: The effects of a magnetic field applied in opposite directions on the domain structure of a bubble film. The field in (a) has the same strength as the field in (b) except it is applied in the opposite direction. In both cases the field is applied perpendicular to the surface of the garnet film.

netic garnet films that have an in-plane anisotropy. The advantage of these films is that the imaging resolution is not limited to a domain size as it is in bubble films. In our experience, when viewing samples that have very low pinning or viewing large samples, in-plane films frequently have a domain structure that can be very noticeable which cannot be easily eliminated even when a large amount of image averaging is employed. Consequently, we opted to use bubble garnet films which limited our best resolution to around 5μm, corresponding to the width of the black and white bubble domains. An additional limitation to the resolution of our system was caused by thickness of the film's active sensing layer which was approximately 3μm. This resulted in the observation of local fields not directly on the surface of a sample, but at an effective height above a sample which caused a further reduction in image resolution. As a result, because of these two factors the overall resolution of our system was estimated to be around 8μm. Another feature of garnet films and many of the materials used in magneto-optic investigations is the limit in the strength of the fields that can be imaged. Fields above a certain value can saturate a film, resulting in a loss of data. In our case, however, most of the fields observed were well below the saturation levels. Field saturation levels in our case ranged from 125 G to 500 G depending on the particular garnet film used. A major advantage over past magneto-optical techniques is the ability of garnet films to remain active over a very large temperature range, right up to room temperature. In contrast, techniques which utilize Eu chalcogenides, are severely limited by a maximum working temperature of no more than 20K. Due to the wide working temperature range which was made possible with garnet films we were able to observe flux dynamics at significantly higher temperatures, right up to the superconducting transition temperature termed the T_c of all the samples.

2.1.2 Experimental Setup

Imaging of the samples was conducted using a standard technique common to magneto-optic experiments. A regulated polarized light source illuminated the surface of the garnet films and an analyzer was placed before the imaging optics and CCD camera. In this way local field variations could be instantly captured and digitized with a frame grabber in a computer, enabling the use of digital enhancement techniques. In Fig.(2.3) component (c) comprises the CCD camera and zoom microscope. The BP-M1C digital camera produced 256 grey scale images from a 2/3 inch charged coupled device which had a pixel array of 768 X 493. The camera itself was Peltier cooled to maintain the life and ensure the proper functioning of the CCD. A zoom microscope capable of 50-350X magnification was fitted on the end of the camera. This particular component significantly enhanced the flexibility of the system. Unlike setups that use commercial polarization microscopes, our microscope could be easily and quickly adapted to accommodate a wide variety of sample sizes, from 2X2cm down to 100X100μm without significant loss of image resolution. For our purposes, the very high imaging resolution achievable with commercial microscopes was unnecessary since we were using bubble domain garnet films which, as previously mentioned, ultimately limited the overall imaging resolution. Also, the microscope provided us with a large and flexible working distance above the samples, from 9cm for the highest magnification up to 18cm for the lowest magnification. Images were captured in the computer, device (a) displayed in Fig.(2.3) with a Matrox Meteor frame grabber. This particular component was supported with a library of C-language functions which could be used as part of any data analysis program developed by the user. The computer, which came with a 17" colour monitor, (b) in Fig.(2.3), and Matrox Millenium video card, had a 166Mhz Pentium processor and 82Mbytes of RAM. A large amount of processor memory was required to support some of the software applications that had been either written or installed on the computer. The computer not only controlled the functioning of
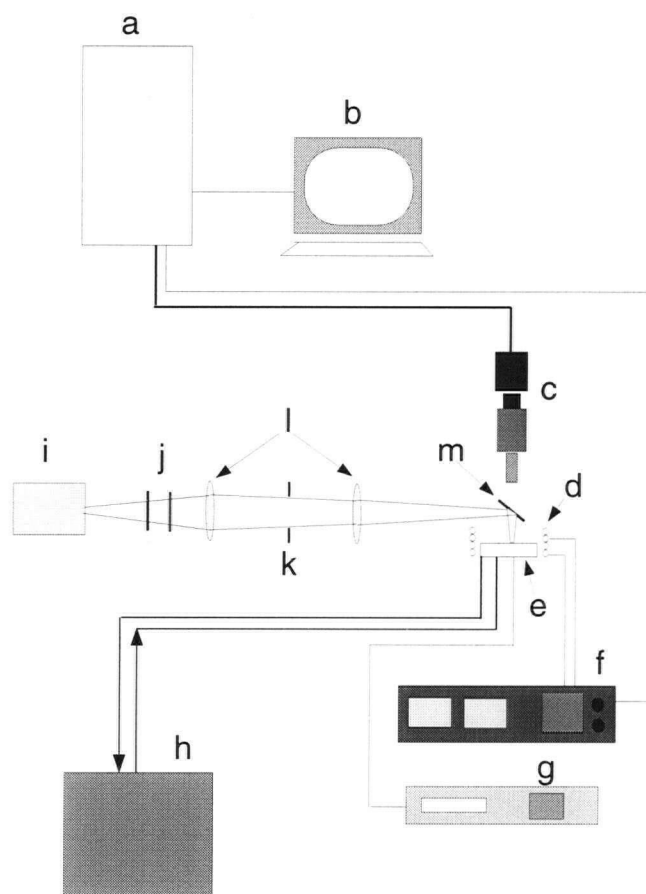
Figure 2.3: A schematic diagram of the magneto-optical setup. The overall system consists of a CCD camera and microscope with zoom optics (c), a flow cryostat (e) attached to a liquid nitrogen pump (h), a solenoid (d) and DC power supply (f) used to apply a magnetic field to the samples, a DC regulated light source (i) with blue filter and polarizer (j) and collimating optics (l) and a temperature monitor and controller (g). A beam splitter (m) was placed beneath the microscope to allow simultaneous illumination and imaging of the samples. The images were processed with a computer (a) and observed with a monitor (b).
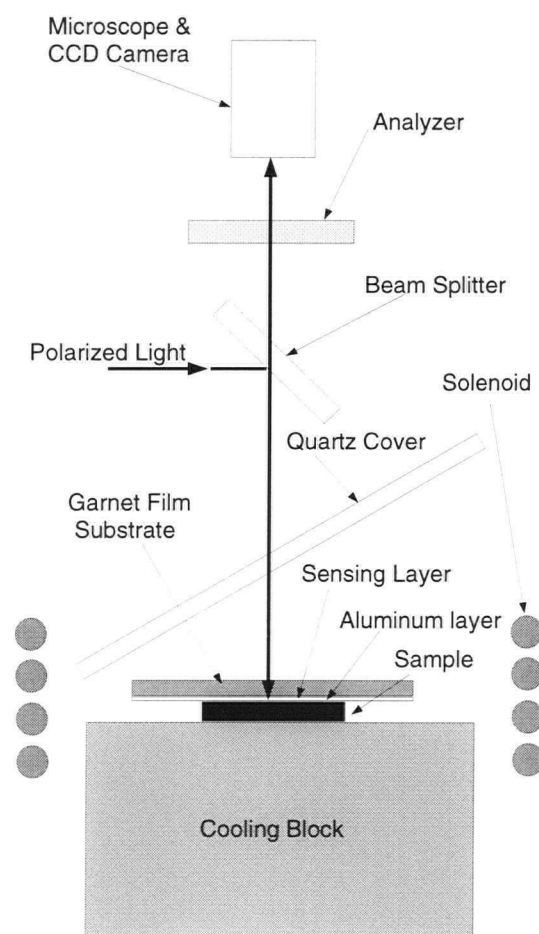
Figure 2.4: Basic cryostat setup showing the typical position of a garnet indicator film with respect to a sample and other components. The films sensing layer, which was coated with 100nm of aluminum, was placed on top of the sample's surface. A sample was placed in thermal contact on top a copper cooling block inside the cryostat. Garnet film and sample were in a vacuum sealed with a clear quartz cover.

the CCD camera but also the application of the magnetic field. The field produced by the solenoid in Fig.(2.3) (d) was supplied with DC current from a Kepco bipolar operational power supply (f) which was controlled with an analog signal from a Advantech 12-bit PCL-728 isolated 2-channel digital-to-analog board installed in the computer. This made it possible to automatically apply a preprogrammed magnetic field to a sample as well as imaging and capturing the resulting field dynamics. The imaging processes developed for this system are described in detail in the next section and some of the corresponding programs are listed in appendices. The samples were illuminated using a 150 Watt, infra-red filtered, regulated DC light source from Fostec, device (i) in Fig.(2.3). A light blue filter along with a polarizer were placed in front of the light source and two lenses (l) were used to collimate the light and adjust the area of illumination. The filter was used to correct for the light yellow colour of the garnet films which had a tendency to reduce the contrast of the grey scale images captured by the camera. An iris diaphragm placed between the lenses served to further collimate the light and also significantly reduced blurring caused by stray light. A 50-50 beam splitter, placed at (m), was used to illuminate the surfaces of the garnet films with the polarized light. Throughout the imaging process samples were held in a flow cryostat, (e) of Fig.(2.3), and maintained at constant temperature. Liquid nitrogen was pumped through the cryostat with a liquid nitrogen pump, component (h), while the cryostat's temperature was monitored and regulated with a Conductus LTC-20 temperature controller and monitor, device (g) of Fig.(2.3). The typical position of a garnet film in relation to the sample and some of the other components is shown in Fig.(2.4). It should be noted that the garnet films used had approximately 100nm of aluminum deposited directly on top of their sensing surfaces. This was done to reflect light through the film and back up to a cross polarizer or analyzer and CCD camera. Typically, a sensing film was placed upsidedown on top of a sample, with the aluminum layer placed next to the sample's surface so that the garnet film's sensing layer was placed as closely as possible to a

13
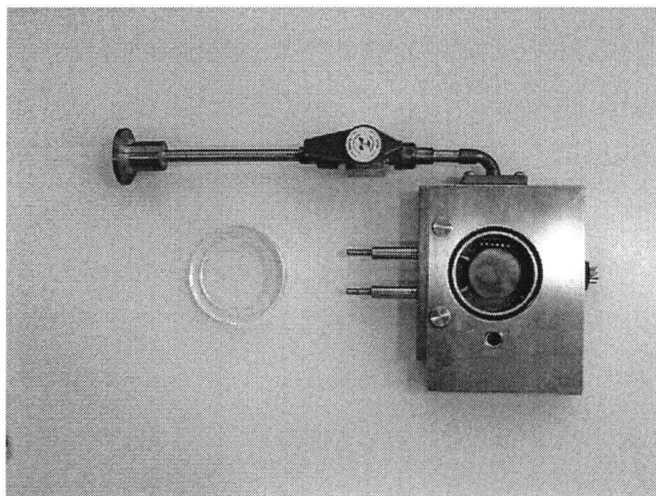
Figure 2.5: Top view of cryostat with quartz cover removed. Inside is the copper cooling block on which the samples are placed. The cryostat was evacuated through the narrow tube shown in the upper part of the picture. The two tubes in the middle of the apparatus allowed liquid nitrogen to be pumped through the cryostat for cooling down to 77K.

sample. As a result, light had to pass through the upper transparent substrate of the film before it was acted on by its lower magneto-optic layer and reflected back up through the film by the bottom aluminum layer. As indicated in the same figure, samples were placed on top of a copper cooling block in the cryostat. Samples were either stuck directly on top of the block with silicon grease as was the case for easier to manage larger superconducting thin films, or in the case of small single crystals, stuck with GE varnish to small silicon wafers which were then glued with silicon grease to the cooling block. A clear quartz cover that sealed the top of the cryostat was placed intentionally at an angle as is indicated in Fig.(2.4). This was done to eliminate reflection off the surface of the cover, reducing glare and providing better quality images. The actual cryostat may be seen in Fig.(2.5) where the quartz cover has been removed to reveal the inner chamber and the copper cooling block on which the samples were placed. By placing the quartz cover on top of a O-ring encircling the top opening of the chamber an effective seal could be formed when the

14
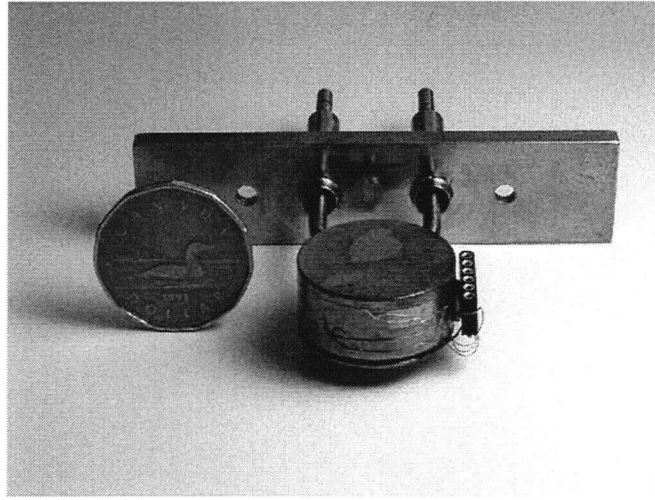
Figure 2.6: View of copper cooling block removed from the cryostat. Its actual size is demonstrated by comparing it to a dollar. The diameter of the copper block is 1-inch. The small plug glued on its side is a connection for a thermometer and heater wire. The thermometer, which was stuck on the facing end of the block, is too small to be seen clearly in this image.

cryostat was evacuated. Air was pumped out of the system through the long thin tube connected to the side of the cryostat shown in Fig.(2.5) where the small valve in the upper part of the image was used to seal the cryostat's chamber. By doing this we were able to turn off the vacuum pump when a sufficiently low vacuum was reached, reducing the amount of vibration imparted to the system during imaging. The outer body of the cryostat was composed of aluminum and was 5 inches by 4 inches in size and 3/4 inches thick. The inner chamber was made by drilling out a sufficiently large hole in the side of the aluminum block to accommodate the copper cooling block. The cooling block was positioned in the center of the chamber by two hollow insulated stainless steel tubes which were fixed to a rectangular copper strip, screwed to the side of the cryostat and sealed with an O-ring. These tubes not only positioned the cooling block but were also used to carry liquid nitrogen to and from the block which itself was hollow. The cryostat was designed in such a way as to allow easy removal of the inner cooling block. This could be done by simply

unscrewing the copper strip from the side of the cryostat and pulling the whole block assembly out of the inner chamber. This part of the cryostat is displayed in Fig.(2.6) along with a Canadian dollar to indicate its relative size. The cooling block was 1 inch in diameter and had a small 1/4 inch deep notch machined around its bottom rim where heater wire was glued in place with Stycast. A calibrated Cernox thermometer from Lakeshore was glued to the facing end of the copper block of Fig.(2.6). and the small plug on the side of the block was used to connect the heater wire and thermometer to the temperature controller and monitor.

2.2 Experimental Procedure

2.2.1 Image Types

Two types of images were produced by our system, in-field images and remnant field images. In-field images are produced by imaging the flux patterns of a sample while it is in a magnetic field. These types of images are useful for observing the flux penetration of samples and were used extensively to study geometrical barrier effects in extremely low pinning single crystals, see chapter 5. Producing a remnant field image requires applying a field only briefly to a sample then imaging the resulting flux dynamics when the applied field is removed. In this class of image, the flux observed has simply been trapped by local pinning structures in the superconductor. As a result, images of this type are useful for detecting local imperfections or pinning centers in a sample.

2.2.2 Basic Imaging Procedure

One of the most important processes used to acquire field images in our system involved a digital averaging and subtraction technique. This method involved capturing a series of images while the applied field was alternatively switched on and off. A single imaging cycle involved applying a magnetic field and, depending on the type of image required, either switching it off of leaving it on while the flux dynamics were captured by the CCD camera and then switching the field direction and repeating the process. Each cycle ended with a pair of flux images of the sample produced by two magnetic fields having equal strength yet opposite polarization. A series of these cycles would then be digitally stored and averaged as pairs during a run to reduce image noise, a significant factor when observing the small remnant fields of low pinning samples. At the end of a run, the two sets of averaged images were then subtracted from one another to digitally subtract out any stationary noise that might be present. This type of noise usually came in the form of small specks

(a)

Flux Structures   Stationary Noise

(b)

(c)

(d)
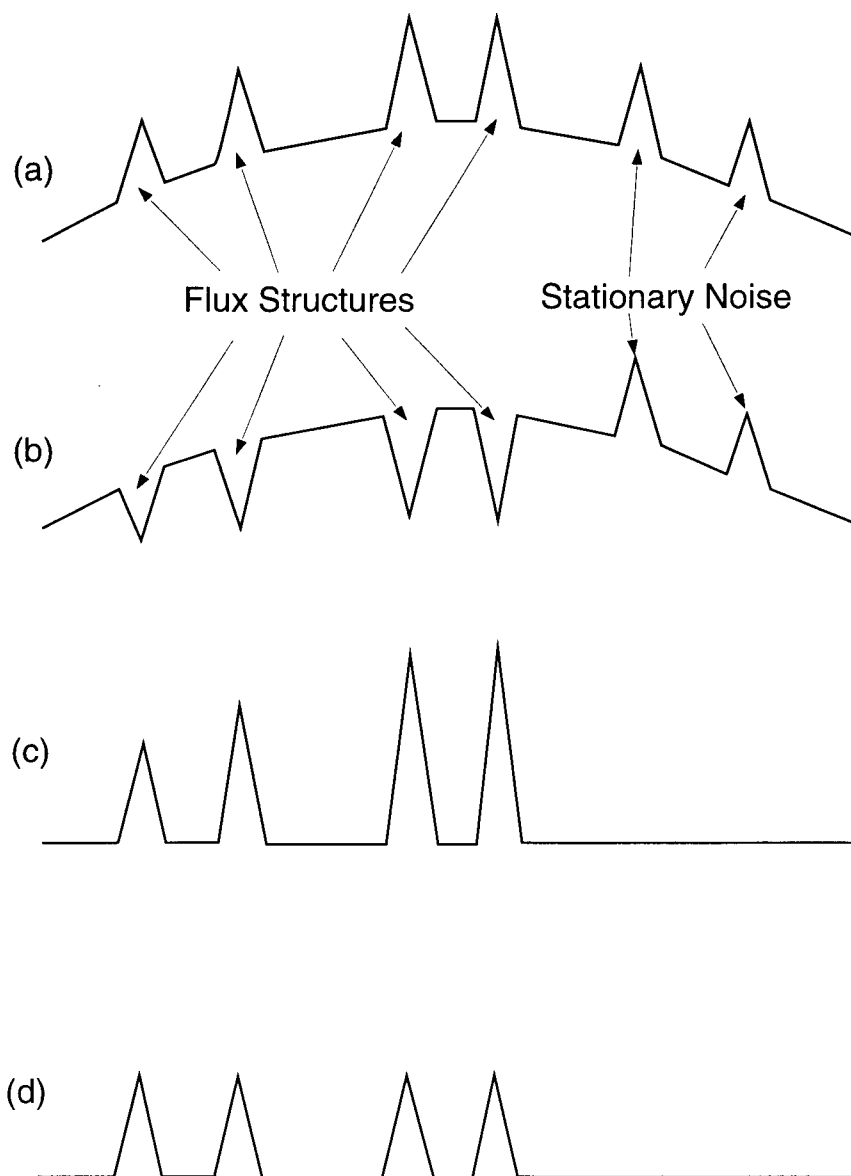
Figure 2.7: In (a) is a profile of six equally strong ideal structures, two of which are caused by stationary noise. The flux structures in (b) are inverted to represent the effect of applying a field of opposite polarity to the field applied in (a). Both upper profiles are curved to demonstrate the effects of uneven illumination. The effect of image subtraction is shown in profile (c) where stationary noise has been eliminated and the flux peaks enhanced. In (d), the uneven background illumination has been divided out producing a true representation of the flux peak strengths.

18

or imperfections on the surface of a garnet film or originated from dirt on the optics and remained constant during each alternation of the magnetic field. The whole process is outlined in Fig.(2.7) where the profiles of six equally strong sources are indicated. Plots (a) and (b) represent ideal profiles of the two flux images after averaging while profile (c) shows the benefits of digital subtraction. Both upper profiles in Fig.(2.7) are bent intentionally to show the effects of uneven illumination where the central region is curved upwards to indicate stronger illumination of the central regions of a sample. The effects of this experimental artifact are not eliminated by digital subtraction and can result in anomalous profile variations, such as enhanced central peak profiles, as indicated in profile (c). This problem is present in all microscopic systems to a certain degree and is best remedied by dividing the images digitally with a reference image taken of the illuminated garnet film's surface prior to an experimental run without applying a magnetic field. Since the reference image will have identical variations in illumination, dividing by this image will essentially eliminate any intensity variations in the final images that are not a product of local field variations from the sample.

2.2.3   Calibration process

The process of noise suppression and correction for spurious light intensity variations results in images that are an accurate representation of the local flux dynamics of a superconducting sample. This makes it possible to calibrate the garnet film field response prior to the data collection routine. The calibration method employed for this system initially required forcing the garnet film to exhibit a linear intensity response under a ramped magnetic field. This was easily achieved by rotating the analyzer on the end of the camera, ramping the field and repeating this process until a linear response was noted. This process ultimately involved a trade off between the linear characteristics required of the film and the amount of contrast present in an image. Generally, the more contrast required of an image, the less linear was the

response of the garnet films used. Next the calibration process required determining the average illuminated intensity of a garnet film's surface while it sat on a sample before an experimental run. Both garnet film and sample were in a vacuum in the cryostat with the sample temperature held just above the superconducting transition temperature. By doing this, the field dynamics produced by the sample, when it was superconducting, would not affect the calibration of the garnet film.

Once the average intensity was recorded a magnetic field of known strength was applied and alternately switched in direction, mimicking the primary routine used to capture images and subtract stationary noise. Two averages of the resulting intensity produced by the garnet film under the known field applied in both directions were then recorded. These two values were then averaged together and, along with the average intensity in the no-field case, used to provide a calibration factor of illumination intensity versus field strength. At the end of an experimental run, after the sample was lowered below its transition temperature and its fields imaged; a program was then used to analyze the fields using the calibration factor to convert the local grey scale intensity variations into local field strengths.

2.2.4 Primary Programming Routines

Five main programs were developed for the magneto-optic system and are listed in appendices A, B, C, D and E. An assortment of other programs were also developed to augment the experimental process which included a simple grey scale imaging program, a average brightness versus field strength indicator used to determine the real-time response of a garnet film in a pre-defined area, and a program for animating a series of images taken of a sample under changing applied fields or changing temperature. The first program listed in appendix A called V-MON monitored the brightness response of the garnet film within an imaging area defined by the user. This area consisted of a variable number of columns and rows of image pixels with no more than 650 columns and 480 rows for any one image. Within this

imaging area were two real-time light intensity profiles of the garnet film taken midway through the image. These profiles could be used to examine the uniformity of illumination as well as the intensity levels. Once a satisfactory viewing area was selected the coordinates were then stored by the program in a parameter file for future reference. The next program listed in appendix B called LIN was used to examine the linear response of the garnet film to an applied magnetic field over the defined imaging area. As previously noted in the last section this process was important in the initial calibration of the film. This program automatically ramped the applied field over a user defined range at user defined increments and plotted the intensity response of the garnet on the computer screen in real time. In this way the analyzer fixed on the end of the camera could be adjusted quickly and easily until a satisfactory result was obtained. Calibration of the film was then carried out using program REFF listed in appendix C and followed the process described in the previous section. After calibration, a sample's flux dynamics were then imaged by the program called SUBF in appendix D using the averaging and subtraction processes previously described. Both the REFF and SUBF programs were controlled with parameters files in which were listed the applied field strengths h0 and h1 in units of Gauss, where h0 was of opposite polarity to h1 along with the duration of their application, delay0 and delay1 in units of milliseconds. Other control parameters included the number of image pairs called frames required by the user for each field direction and also a looping number which increased the number of images averaged for each pair. Another small yet important parameter control involved the adjustment of the camera contrast. This feature proved to be very useful when imaging low pinning samples that had small remnant fields. In such samples any small defects in the garnet film, which were not eliminated by image subtraction, tended to overwhelm an image, resulting in very low contrasting pictures. It was discovered that this problem could be significantly reduced by lowering the digitizing contrast response of the CCD camera which tended to reduce the relative intensity

of garnet film defects. At the end of an experimental run several parameters were appended at the end of the final image file by the SUBF program for use by another imaging program called VG listed in appendix E. These parameters included the maximum and minimum grey scale intensities in a particular image, the intensity versus field strength calibration factor, and the average grey scale intensity of the garnet film in the absence of any fields. The program VG had several useful features which included a mouse controlled cursor that could be pointed at any part of an image to reveal a field strength, two x,y field strength profiles which could be easily moved by the mouse across the image by the user and image reversal which proved to be very useful when examining many small flux structures. Both SUBF and VG programs together provided almost real time imaging of flux dynamics. Typically, images were captured in no more that a few minutes and after an experimental run local field strengths could be quickly viewed and analyzed. Field strengths were provided by the VG program through a calculation that converted grey scale intensities into local field strengths where:

$$fieldstrength = \frac{slope \times intensity + min - zro}{pslope} \qquad (2.1)$$

and:

$$slope = max - min/255 \qquad (2.2)$$

where *max* and *min* were the maximum and minimum grey scale intensities of an image with 255 being the maximum intensity, where *pslope* was the illumination intensity versus field strength calibration factor and where *zro* was the average illuminated intensity of the garnet film being used in the absence of any fields. A very useful feature common to many of the programs written for the magneto-optic setup was the ability to quickly grab and display images, providing real-time observations of light intensity fluctuations. A typical section of C-programming which made this possible is listed in Fig.(2.8), including the library functions used to control the frame grabber. The main part of the routine included a loop in which

22

```
                    . . . . . .
MdigControl(MilDigitizer,M_GRAB_MODE,M_ASYNCHRONOUS);  (a)
                    . . . . . . .
MdigGrab(MilDigitizer,MilImage[grabbuf]);  (b)
While(TRUE){
        if(grabbuf==0){
                grabbuf=1;
                procbuf=0;
        } else {
                grabbuf=0;
                procbuf=1;
        }
        MdigGrab(MilDigitizer,MilImage[grabbuf]);   (c)
        MbufCopy(MilImage[procbuf],MilImageDisp);   (d)
        MdigGrabWait(MilDigitizer,M_GRAB_END);   (e)
}
                    . . . . . .
```

Figure 2.8: General programming routine used for real time imaging. In command
(a) the digitizer grab mode has been set to asynchronous, enabling the program
to proceed without waiting for the completion of an image grab. Command lines
(b) and (c) are used to grab and store images in two buffers. The last image to
be buffered is copied and displayed by command (d) while another image in being
buffered by command (c). The last command labeled (e) instructs the system to
wait until all grabbing has finished before returning to the "while" loop.

two data buffers were used to alternatively display an image or to store an image

being grabbed from the CCD camera. This made it possible for an image to be

displayed while another image was in the process of being captured, significantly

enhancing the frame rate imaging speed. In the absence of any other routines,

this technique can produce a frame rate of 30 frames per second. For this to work

properly, however, it was necessary to control the frame grabbing synchronization

which was provided by the command labeled (a). In this command, image grabbing

has been defined to be asynchronous, meaning that an application, such as displaying

an image, does not have to be synchronized with the end of a grab operation, but

can run just after initiating another image grab. As a result a previously buffered

image loaded in either MilImage[0] or MilImage[1] depending on the while loop cycle, could then be displayed by command (d) while a new image was being stored in the other free buffer, ready for the next imaging cycle. The last command labeled (e) on the previous page then forced any applications to wait until all grabbing had been completed, before the next cycle of the while loop could be executed, preventing any programming anomalies caused by over buffering. This last command was not always necessary in larger programs, however, since many more commands were usually executed after the grab loop which tended to slow down the imaging cycle process.

Chapter 3

Surface Current Calculation

3.1 Introduction

Flux imaging is a useful technique in the examination of local inhomogeneities in a superconductor. The computational processes used to determine local currents directly from experimental flux imaging enhances the technique even further, providing valuable insights into some of the mechanisms involved in flux and current dynamics. Two methods are generally used in the determination of local currents in superconducting samples. One such method involves fitting calculated field distributions using a specific current model while the other is based on a more general use of the Biot-Savart law which provides the local currents directly from imaged fields. The latter technique has the advantage of being more general and can be utilized for a variety of sample shapes and sizes. This method, however, involves addressing a nontrivial problem requiring an inversion technique which can require a substantial amount of computer memory, depending on the type of technique used. Alternatively an iterative method which is less demanding as far as memory is concerned can be used but can require significant time for convergence to a solution. We opted to use the iterative method using an improved iterative technique recently developed to augment the convergence process that still provides accurate results[25].

3.2 Basic Theory

In theory it is possible to derive current density directly from gradient measurements of local magnetic induction, $\partial B_x/\partial z$ and $\partial B_y/\partial z$, where according to Ampère's law:

$$\mu_o \vec{j} = \vec{\nabla} \times \vec{B} \tag{3.1}$$

This is not a feasible option , however, in most magneto-optical experiments where only the B_z component of the fields is measured. As a result it is necessary to use an integral relation where the magnetic induction B_z is produced by a magnetic moment in a cell. The basic model we used was similar to the one developed by Xing and Grant et al.[26]. In this method a sample's remnant field is modeled using a two dimensional array of square cells on a grid, each with a local magnetic moment produced by two dimensional surface currents. In adopting this model it is assumed that the z-dependence of the surface current density across the surface of a sample can be neglected and that the current distribution of a sufficiently thin superconductor, such as a thin film, can be modeled adequately using just a two dimensional distribution of magnetic moment cells. The configuration of the model is indicated in Fig.(3.1) where the magnetic moment centered in cell (u, v) is producing magnetic induction B_{0z} at the point (x, y, z). The corresponding integral relation involving both quantities can be written as:

$$B_{0z}(x, y, z, u, v) = \frac{\mu_o}{4\pi} M(u, v) \int_{S_{u,v}} \frac{3z^2 - r^2}{r^5} d\acute{x} d\acute{y} \tag{3.2}$$

where $M(u, v)$ is the magnetic moment of the unit cell at (u, v). It is important to note that, since a two dimensional model is being used the unit of magnetization is given in terms of Amps and not Amps/cm as is the case with three dimensions. Also it should noted that the z term in the integrand is a constant representing the height at which the fields are detected, a reasonable assumption considering that a garnet indicator film is always at a constant effective height above a sample due to its thickness. The integral in eq.(3.2) can be incorporated into a single term for

26
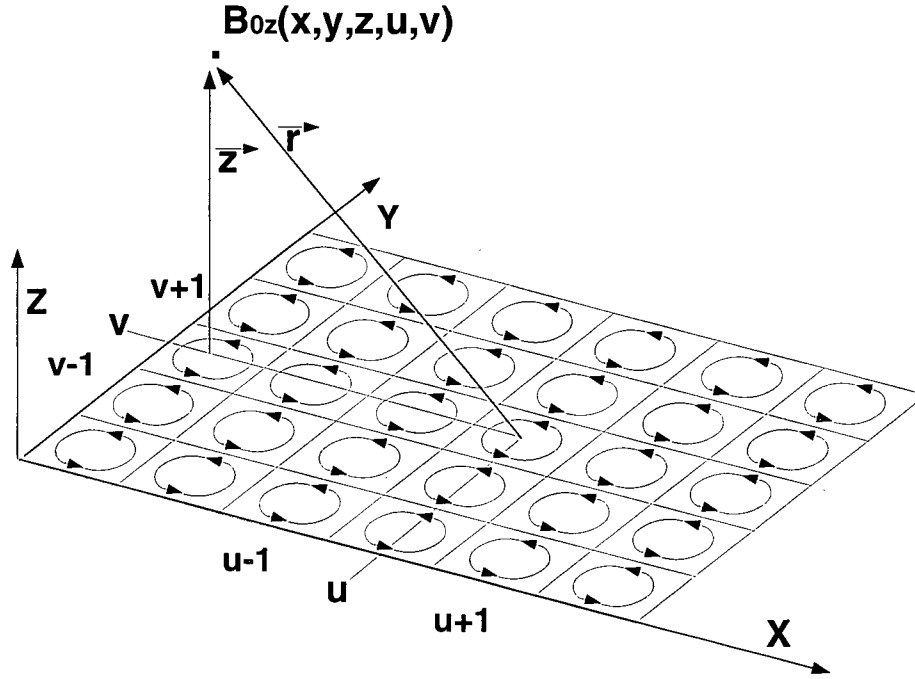
Figure 3.1: Representation of the two dimensional model used in the determination of surface or sheet currents. The z-component of the field produced by the surface current in cell (u, v) is measured at a constant height z.

simplicity so that:

$$B_z(x,y) = G(x,y,z,u,v)M(u,v) \tag{3.3}$$

where u and v are the cell coordinates, $G(x,y,z,u,v)$ is a coefficient which contains all its geometric properties including its position relative to the sensing garnet film. In reality the problem of determining local currents is significantly complicated by the fact that all the local moments present on the surface contribute by superposition to the B_{0z} field, where the effective field strength produced by each cell is position dependent. This feature can be included in the model by summing over all the local moments so that the field strength observed at each point is a superposition of all

the individual magnetic moments:

$$B_z(x,y) = \sum_{u=-N_1/2}^{N_1/2} \sum_{v=-N_2/2}^{N_2/2} G(x,y,z,u,v)M(u,v) \qquad (3.4)$$

where in general there are $N_1 \times N_2$ square cells with a corresponding number of B_z data points. This last equation is a set of linear equations for $M(u,v)$ which can be represented by the matrix equation:

$$\mathbf{G} \cdot \mathbf{M} = \mathbf{B_z} \qquad (3.5)$$

If we define the surface grid to be square so that $N_1 = N_2 = N$ then Eq.(3.5) is a system of N^2 unknowns in $M(u,v)$ with N^2 experimental $\mathbf{B_z}$ field points while $\mathbf{G}$ is a matrix of order $N^2 \times N^2$. It is then possible to determine the surface magnetization using numerical methods to solve for $M(x,y)$ exactly in Eq.(3.5) or by employing the iterative procedure. Once this quantity is found, local surface or sheet current density $\vec{\Lambda}$ can then be calculated using the the relation:

$$\vec{\Lambda} = \vec{\nabla} \times \vec{M} \qquad (3.6)$$

Since we are dealing with two dimensional sheet magnetization then the only non-vanishing components in Eq.(3.6) are (Λ_x, Λ_y) so that:

$$(\Lambda_x, \Lambda_y) = \left(\frac{\partial M}{\partial y}, -\frac{\partial M}{\partial x} \right) \qquad (3.7)$$

where Λ_x, Λ_y are in units of Amps/cm.

3.3 Matrix Solution of Surface Magnetization

Determination of the surface sheet magnetization using the matrix relation, Eq.(3.5) requires solving a set of linear algebraic equations in Eq.(3.5) for $\mathbf{M}$. One useful technique commonly employed is called LU-decomposition. This method requires writing $\mathbf{G}$ as a product of two matrices to facilitate a solution:

$$\mathbf{L} \cdot \mathbf{U} = \mathbf{G} \tag{3.8}$$

where $\mathbf{L}$ is a lower triangular matrix and where $\mathbf{U}$ is an upper triangular matrix. Substituting Eq.(3.8) in Eq.(3.5) for $\mathbf{G}$ we get:

$$\mathbf{G} \cdot \mathbf{M} = (\mathbf{L} \cdot \mathbf{U}) \cdot \mathbf{M} = \mathbf{L} \cdot (\mathbf{U} \cdot \mathbf{M}) = \mathbf{B_z} \tag{3.9}$$

The motivation behind this substitution is that two matrix relations are formed, each having a triangular set of equations which are easily solved where:

$$\mathbf{L} \cdot \mathbf{V} = \mathbf{B_z} \tag{3.10}$$

is solved for $\mathbf{V}$ and where:

$$\mathbf{U} \cdot \mathbf{M} = \mathbf{V} \tag{3.11}$$

is solved for $\mathbf{M}$, the sheet magnetization. Numerical packages are available which use LU-decomposition as a means of determining the solutions to a set of linear equations. While these algorithms can solve large numbers of equations they eventually become impractical because of the very large number of equations usually needed to solve for even relatively small experimental $\mathbf{B_z}$ images. The problem with this technique originates from the excessive amount of computer random-access-memory needed to run the programs since the $\mathbf{G}$ matrix scales as N^4. In the author's experience, processing a simple 71X71 pixel image using LU-decomposition required over 100MBytes of RAM on a main frame computer. One way to lessen this problem is to simply find the inverse of the $\mathbf{G}$ matrix just once, using LU-decomposition.

By doing this, local sheet magnetization values can then be determined by performing a matrix multiplication of the experimental $\mathbf{B_z}$ values with the inverted $\mathbf{G}$ matrix elements. The advantage of this method is that the inverse matrix can be stored on a computer's hard drive memory and used repeatedly for all subsequent images. This technique, however, severely limits the versatility of an imaging system since the number of image cells used for each image must remain the same and the sensing film height must not vary. Also the images processed are still relatively small. Another algorithm investigated by the author and independently by Wijngaarden et al.[27] for use in this problem involves treating the $\mathbf{G}$ matrix as a symmetric Toeplitz matrix and finding a solution using a recursive algorithm called Levinson's method. A Toeplitz matrix is specified by $2N^2 - 1$ numbers g_k using the previous notation of $N_1 = N_2 = N$ for the number of square cells, where $k = -N^2 - 1, \cdots - 1, 0, 1, \cdots N^2 - 1$ and where the matrix has the form[28]:

$$\mathbf{G} = \begin{pmatrix} g_0 & g_{-1} & g_{-2} & \cdots & g_{-N^2+2} & g_{-N^2+1} \\ g_1 & g_0 & g_{-1} & \cdots & g_{-N^2+3} & g_{-N^2+2} \\ g_2 & g_1 & g_0 & \cdots & g_{-N^2+4} & g_{-N^2+3} \\ \cdots & & & \cdots & & \cdots \\ g_{N^2-2} & g_{N^2-3} & g_{N^2-4} & \cdots & g_0 & g_{-1} \\ g_{N^2-1} & g_{N^2-2} & g_{N^2-3} & \cdots & g_1 & g_0 \end{pmatrix} \tag{3.12}$$

and is symmetric if $g_k = g_{-k}$ for all k. This technique has the rather useful feature of significantly reducing the amount of computer memory needed in finding a solution where in this case the matrix $\mathbf{G}$ scales as N^2. This is so because a symmetric Toeplitz matrix is comprised of N^2 independent elements the minimum number needed to solve for the N^2 $\mathbf{M}$ unknowns. As a result only this number of $\mathbf{G}$ matrix elements ever need to be computed. In the author's experience, however, this method proved to be quite slow in providing a solution compared to the iterative techniques using

30

similar image sizes. The problem of inverting the **G** matrix has been addressed more recently by Joss et al.[24] exploiting the translational invariance of the Biot-Savart's law, enabling the application of the convolution theorem. This method is a significant improvement over other techniques in that it can be used on much larger images, having a greater numbers of image cells. One problem with the technique, however, is the presence of a significant degree of image noise which must be reduced by low-pass-filtering. Without filtering, it is reported that the resulting current distributions are dominated by noise which is worsened by an increase in measurement height above a sample. This ultimately limits the spatial resolution that can be achieved with this method.

3.4 Basic Iterative Technique

The local magnetic moments can also be calculated using an iterative procedure which avoids the problem of using an excessive amount of computer RAM. The memory required for this application is proportional to N^2, similar to the amount required by the Toeplitz matrix method. In the author's experience, however, iteration provides the same results in far less time using available numerical routines. The process begins with assigning values to the local magnetic moments determined directly from the measured fields and from the geometrical coefficient without any summation of local moments $G(x, y, z, u, v)$ in Eq.(3.3) where:

$$M_0(x, y) = B_z(x, y)/G(x, y, z, u, v) \qquad (3.13)$$

and $x, y = 1, 2, 3, \cdots, N$. Initially it is assumed that the most significant contribution to the magnetic induction originates from the local moment situated directly beneath the experimental field point, thus ignoring all the contributions from the neighbouring cell moments. The $M_0(x, y)$ values are then substituted into Eq.(3.4) for $M(u, v)$ and summed with the geometrical coefficient $G(x, y, z, u, v)$ to calculate

31

the induction contributed by all the cells having this magnetization.

$$B_{z0}(x,y) = \sum_{u=-N_1/2}^{N_1/2} \sum_{v=-N_2/2}^{N_2/2} G(x,y,z,u,v)M_0(u,v) \qquad (3.14)$$

Essentially an approximation to the magnetic induction is calculated across the surface of a sample using the initial local sheet moments $M_0(x,y)$. An attempt to correct this approximation is then made by taking the difference between the experimental induction values and the calculated values, $\triangle B_z = B_z - B_{z0}$ and substituting them into Eq.(3.13) to give:

$$\triangle M(x,y) = \triangle B_z(x,y)/G(x,y,z,x,y) \qquad (3.15)$$

This correction to the calculated local sheet moments is then added to the original estimate so that:

$$M_1(x,y) = M_0(x,y) + \triangle M(x,y) \qquad (3.16)$$

The new values of $M_1(x,y)$ are then substituted into Eq.(3.4) to calculate the magnetic induction produced by the new corrected local moments. The whole process of calculating new local moments and using the difference between the calculated local magnetic induction and the experimental induction to produce further corrections to the local moments is repeated until convergence to a solution is noted. This occurs when the difference between the measured and calculated magnetic induction is considered to be insignificant compared with experimental error, usually $<$ 0.01%. After completion of this process, the local current distribution is determined by taking the curl of the final magnetization distribution numerically for each point on the sample's surface. It has been observed from repeated use of this technique that convergence to a solution only occurs when the height at which B_z is measured is no greater than 1.1 cell widths above the surface of an imaged sample. In other words, a large image must have its pixel number first reduced by averaging so that the surface cell width between each pixel is not less than 0.91 units of the garnet film height above a sample.

3.5 Augmented iteration

One of the greatest drawbacks in using the iterative process is the amount of time needed for the iteration to converge to a solution when processing larger images. Depending on the image size and the speed of the computer system used, the time required for convergence can take from hours to several days. The duration of convergence is mainly dependent on the amount of summation required in Eq.(3.14). As a result, the time required for a solution scales approximately as N^4. For this reason, a modified version of the technique described in the last section was developed which significantly reduced the computation time. In this method the number of pixels in an image was reduced initially to take advantage of this scaling effect. For example, decreasing the field points to a quarter of their initial number would result in a 4^4 increase in the iteration speed. An additional time saving feature was the calculation of B_z, using Eq.(3.14), to sum over only nearest neighbouring cells, termed a limited iteration. This resulted in an even shorter iteration cycle and yet provided results as accurate as those calculated using the full summation. Field contributions from the more distant moments were simply added to each point during each iteration. These fields were calculated before the main iterative cycle was initiated using just one iteration that included the field contributions from all cell moments. These distant fields were not changed during the rest of the iterative process, until convergence was achieved and were, therefore, an approximation. This approximation, however, did not effect the final result significantly since the field effects from distant neighbours were relatively small and had only an average contribution which did not change significantly after each iteration. The number of nearest neighbouring cells used could be adjusted by the user to optimize the process so as to get the most accurate results in the least amount of time. It was determined from trial and error, that for an average sized image of 150X150 pixels, the field contributions from only 32 nearest neighbouring cell moments were needed to get the best results. Part of the augmented process, involving cell reduction by

(Bz-field)   Reduce cell number down to 1/16 by averaging   (Bz-field)

20x20 cells   (1)   5x5 cells   Perform iteration (2)

(M-Sheet)   double cell number   (M-Sheet)

10x10 cells   (3)   5x5 cells

use in next iteration cycle
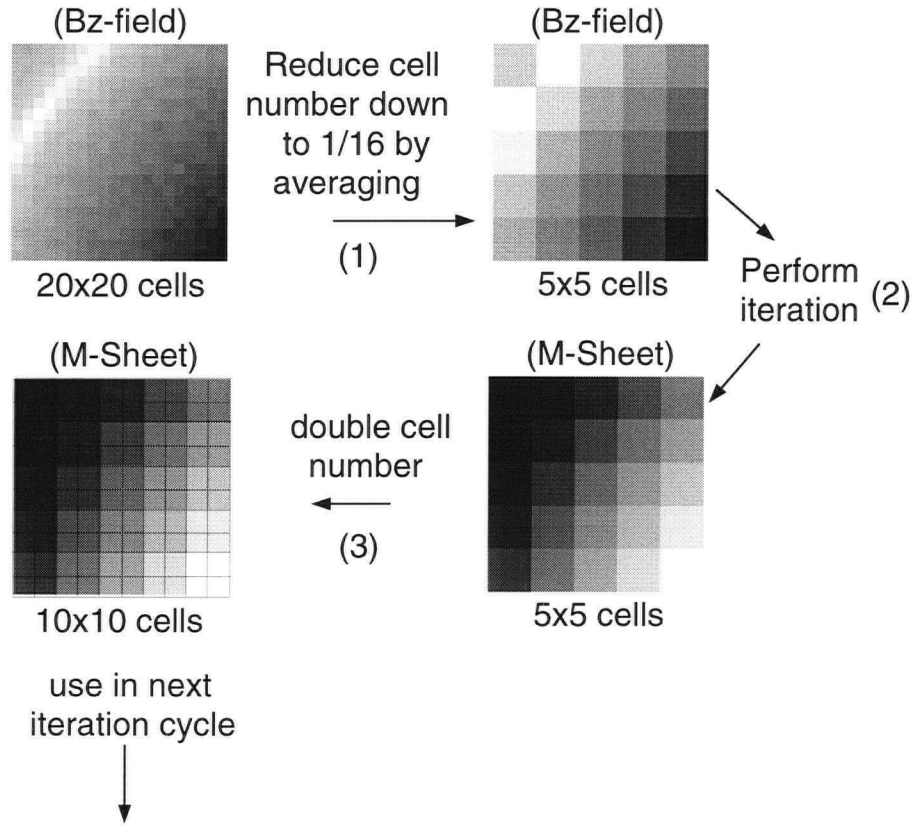
Figure 3.2: Small section of image processed from a circular thin film using the augmented iterative process described. The augmented process involves a series of steps that include reducing the cell numbers step 1, to increase the speed of convergence, step 2. Cell magnetization numbers are increased, step 3 to augment the next cycle, Fig.(3.3)

averaging is outlined in Figs.(3.2) and (3.3) for a 20X20 cell segment of an experimental in-field image of a 4mm wide superconducting circular thin film at 90K. The results from processing this image may be seen near the end of this chapter, while details concerning flux penetration of the thin film at various temperatures can be seen in chapter 5. The whole augmented process involved a series of iterative stages, usually three, using reduced cell numbers. Initially, the number of field points in a B_z field image was reduced to 1/16th of their original number by averaging as indicated in Fig(3.2) in step 1. This involved taking the average of sixteen near-

est neighbouring field cells to produce one cell that covered the same surface area as the sixteen original cells, or equivalently a cell having four times the original cell size. By doing this the resulting image covered the same surface area as the original image, but had substantially less field pixels and consequently less resolution. An initial iteration was performed to calculate approximately the moments and field contributions from distant neighbouring cells. The process of applying limited iteration to the reduced image was then performed as indicated in step 2 of Fig.(3.2) until convergence to a solution which provided a sheet magnetization image having the same size and pixel number as the reduced image. Due to the reduced field point numbers this part of the process always concluded very quickly. Next, the number of pixels in the magnetization image was increased by repeating each magnetization point four times producing blocks of four nearest neighbours with identical values, step 3 of Fig.(3.2). This produced a new image with the same magnetization values and resolution as the reduced image but with four times the number of pixels. The purpose for doing this was to then repeat the iteration using these values in a new reduced pixel field image. As indicated in Fig.(3.3) step 4, the field point number was once again reduced, only this time to 1/4 of their original numbers to match the new magnetization image and again, a preliminary iteration was performed to calculate distance cell moment field contributions for the new cell number. A limited iteration was then applied to the reduced field image, see step 5 Fig.(3.3), only this time including the magnetization values calculated in step 3. While convergence would have been substantially slower since the number of cells, while reduced, were 4 times greater than those used in the first cycle, the inclusion of the magnetization values from the first cycle substantially reduced the amount of time needed to acquire a solution. Once again, the number of cells was increased by four times in the resulting magnetization image. The final cycle was then performed in step 6 of Fig.(3.3) employing the same process as that used in step 3 of Fig.(3.2) which included a preliminary iteration to determine the distant

35
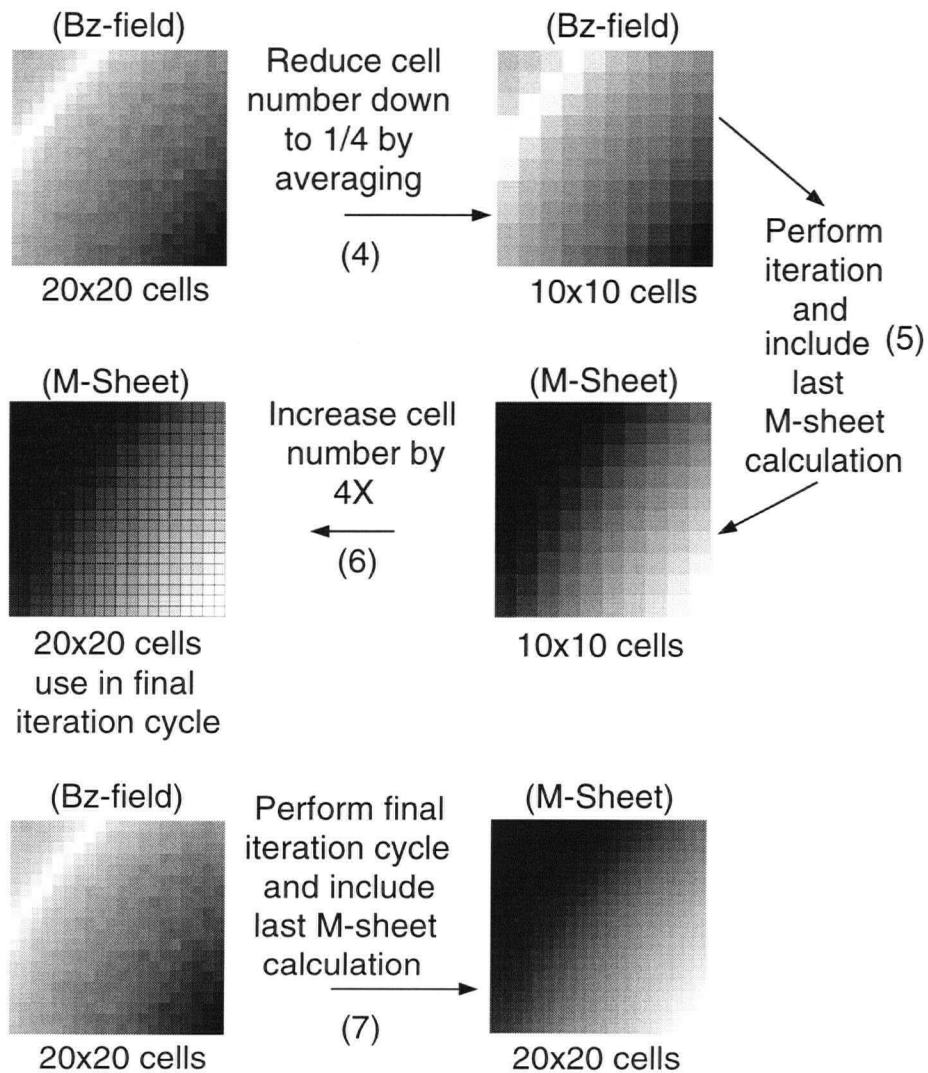
Figure 3.3: Cell magnetization values calculated in steps 2 and 3 in Fig.(3.2) are used in step 5 to decrease the time needed to achieve convergence to a solution. The final magnetization image produced in step 6 is then used to augment the final iteration of step 7

magnetic moment cell contributions to the local surface fields. Also magnetization values were again included in the final calculation, which resulted in a substantial decrease in the number of iterations needed to acquire a solution. Finally, in step 7 of Fig.(3.3) only a few limited iterations, over 32 nearest neighbours were needed to acquire a final image having the same resolution and pixel numbers as the original experimental field image. In short, reduced cell images were used to quickly calculate local magnetization moments which were used in the higher resolution field images to augment the iteration. The advantage of using reduced cell images is a substantial reduction in the time required for convergence to a solution. The amount of time needed is actually quite flexible and is dependent on the amount of accuracy required by the user. Optimization of the convergence process is discussed at the end of this chapter.

3.6 Local Moments of Circular Thin Film

In order to determine local sheet moments of a superconductor in an applied magnetic field, it is necessary to subtract numerically the applied field from the imaged local magnetic induction. Doing this leaves the self-induction response of the sample which is the quantity needed to determine local surface currents dynamics using iterative processing. This must be done to all in-field images if the self-induction is required, otherwise the applied field itself would contribute anomalous currents that would be present even outside a sample's perimeter. In Fig.(3.4) (a) is a 156X134 in-field image of a superconducting circular thin film at 90K in an applied field of 10 Gauss along with (b) the local sheet magnetization image calculated with the augmented iteration. The largest Bz-fields or greatest local magnetization surface response is depicted by the lightest areas in either image (a) or (b), while the smallest or zero values, are indicated by the darkest areas. The diamagnetic response of the film is noticeable as a dark region in the center of the in-field image. There is a corresponding change in the surface magnetization in this region as indicated
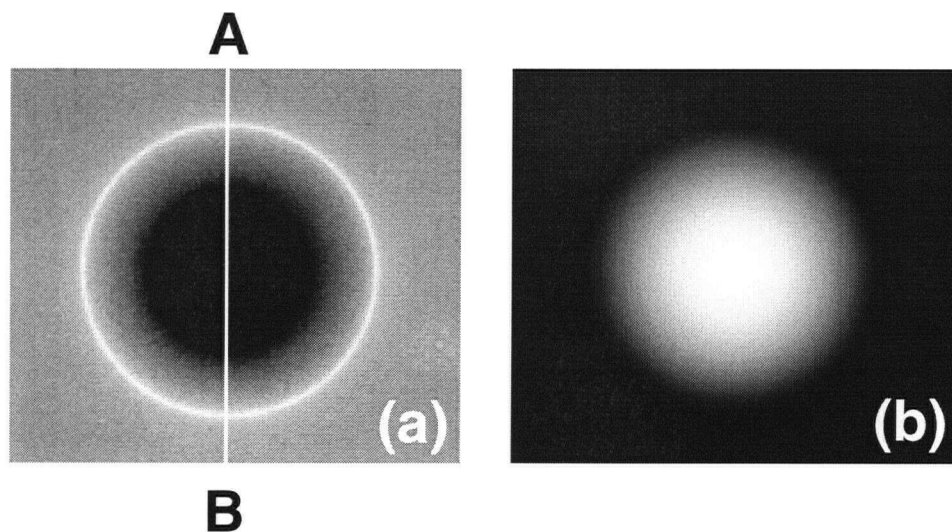
Figure 3.4: (a)156 x 134 cell in-field image of circular thin film and (b) sheet magnetization image calculated with the iterative technique. Cross sections of both images my be seen in the next figure. The A-B line through the in-field image indicates where the cross section was taken relative to the sample position.

in the accompanying (b) image of Fig.(3.4); a reasonable result since larger surface currents are needed to expel the applied field. Outside the sample, surface moments are virtually absent, observable as darkest regions in the same figure. Cross sections were taken along the A-B line in Fig.(3.4) of the samples local self fields and calculated sheet magnetization values and are displayed in Fig.(3.5). The diamagnetic response of the film is present in the upper image, producing a relatively flat field distribution of -10 Gauss in the center, while there is a noticeable response in the local sheet magnetization, with a corresponding minimum in the center. According to the lower plot there is a small amount of residual surface magnetization present outside the sample. This result, however, is an artifact caused by small experimental errors that produced negligible effects within an experimental uncertainty of ±5%. Additional results and observations of the film response dynamics at different temperatures along with local currents calculated from the local surface moments are discussed further in chapter 5.
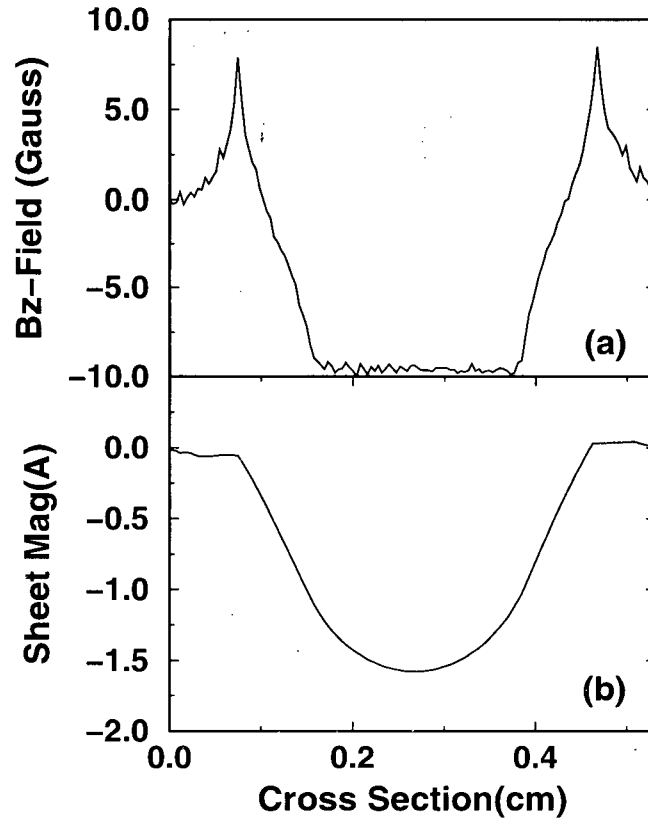
Figure 3.5: (a) Cross section along the A-B line of Fig.(3.4) indicating the thin films self-induction response found by subtracting the applied field from the imaged fields, (b) same section taken across the film of the local sheet moments calculated using the augmented iteration.

3.6.1 Optimized Processing of Sheet Currents

Performing repeated iterations to speed up the final iterative cycle provides substantially faster results compared to the one cycle process. One of the keys to reducing the time needed for convergence originates with the number of limited iterations performed in the final cycle, when the image is at its highest resolution since this requires the greatest amount of computer processing. Consequently, it is necessary to reduce the number of limited iterations in this cycle as much as possible without significantly degrading image quality. The results of using different numbers
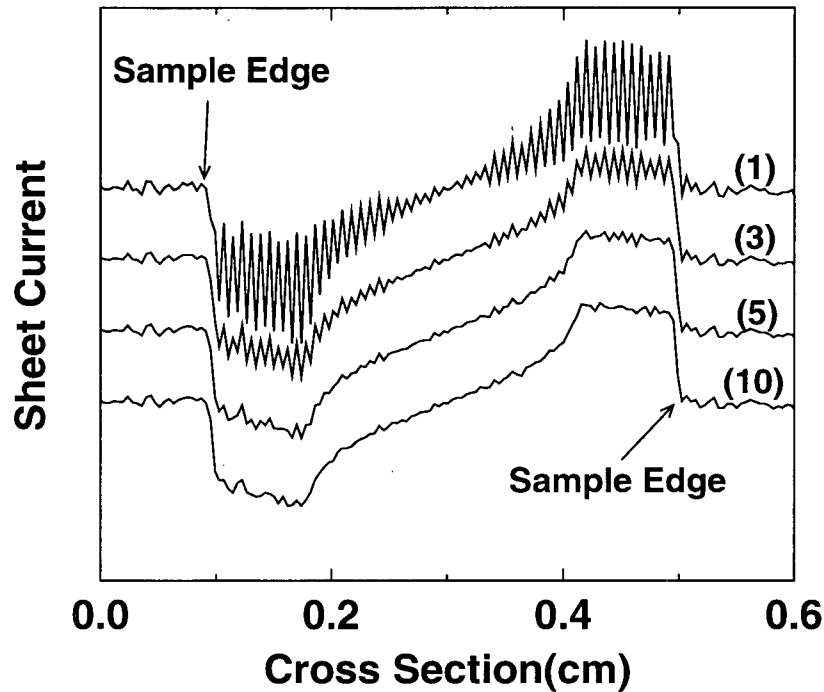
Figure 3.6: Sheet current profiles using four different numbers of final limited iterations. The best results, were produced with 10 final limited iterations which provided the fastest results with the least amount of processing error.

of limited iterations in the final cycle can be seen in Fig.(3.6) where the in-field data of Fig.(3.5) was used as a test image. In these profiles are displayed sheet current values, calculated from local moments, which tend to be more sensitive to data anomalies. Currents were greatest in the outer penetrated rim and substantially less near the center of the sample, dropping to zero at the center. Outside the sample, sheet currents were insignificant and only varied from image noise. The minimum peaks on the left in all four plots of Fig.(3.6) were of similar strength to the maximum peaks on the right, but were negative to indicate relative current flow. This implied that the surface currents tended to flow around the center of the sample, moving in opposited directions to each other through the displayed cross sections. Local surface moments were initially calculated using the pixel number reduction

technique previously described. This involved two cycles where the pixel number had been reduced by averaging to increase the processing speed while also employing limited iteration. The final third cycle was then performed using different numbers of limited iterations to observe the effect on the sheet current data. It is very apparent from the upper plot in Fig.(3.6) that one limited iteration was not sufficient. Significant data spikes were present wherever there were larger surface currents, a result of using the lower resolution magnetization image data to augment the final cycle. Increasing the number of limited iterations in the final cycle, however reduced this artifact. It was determined, for the type of in-field image being processed that 10 limited iterations produced the best results in the least amount of time. Any data noise present in the lowest plot of Fig.(3.6) originated with the in-field data and was not part of any processing anomalies. Also important was the amount of time used in calculating the reduced sheet magnetization images to augment the final iterative cycle. In this case it was found that more than 40 limited iterations in the first cycle and 40 limited iterations in the second cycle were the most efficient numbers to use to get images of good quality having relatively small errors compared to the images calculated using much larger numbers of iterations for each cycle. Using as many iterations as necessary to eliminate any data processing error produced images identical to those calculated using the one cycle process. In this case it was determined that the augmented iterative technique was at least 20 times faster at providing results. If data errors of $\pm 1\%$ can be tolerated then using the number of limited iterations suggested previously for each cycle will produce results 70 times faster than the one cycle method.

3.6.2 Sensing Film Height

One possible factor to consider in applying the iterative sequence to an experimental field picture is the estimation of the sensing iron-garnet film height. An estimate of $5\mu m$ is used in the determination of local currents in this work; see chapter 5. This

number has been carefully chosen to represent the typical effective sensing height of a garnet film above a superconductor and includes the thickness of the sensing layer and the space comprising the contact between the top of a sample and bottom of the garnet film where the sensing layer is placed in closest contact with a sample. Refer to chapter 2 for the details of this configuration. While great care was taken to prevent any significant errors in estimating the sensing film height various factors can ultimately affect this parameter. One possible source of error can originate directly from the sample itself where small surface irregularities can increase the space between the sensing film and sample surface. In addition to this microscopic dust particles on the surface of a sample can also also affect the sensing film height producing an additional source of error. In cases where this problem is significant imaging of the sample will immediately indicate a characteristic image blur, caused by an increase in the sample-sensing film spacing. In this case, measures can be taken to compensate for this problem by increasing the sensing film height parameter in the inversion algorithm or by cleaning the sample thoroughly or using a sample with a smoother surface. In much less severe cases, however, imaging may not indicate a problem since blurring will be much less noticeable. It is possible to determine the sensitivity of the inversion technique to this problem and, thereby, to qualitatively establish the amount of error that may be present in a typical current image. This was done by performing an iteration on the experimental fields from the circular thin film displayed in Fig.(3.4) (a) using a greatly exaggerated effective sensing film height of 20μm. The result is indicated in Fig.(3.7) where a comparison is made using the best estimated sensing film height of 5μm and the grossly over estimated height. As indicated by the dotted line in that figure over estimating the film height results in an increase in the apparent current image noise. It is also noticeable, however, that such a large error in the sensing film height does not appreciably affect the overall local surface current values. An iteration was also performed on the same field image using a more reasonable estimated height of 10μm. In this
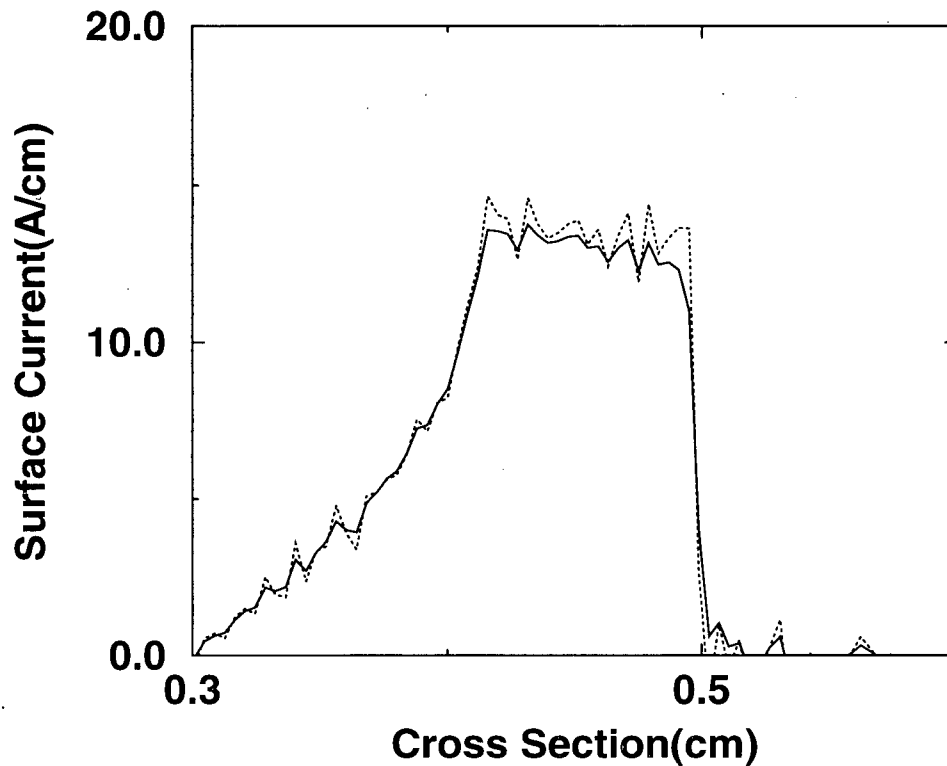
Figure 3.7: Comparison of different estimates of garnet film height above the surface of a sample. The solid line represents the best estimated effective height, 5μm while the dotted plot indicates the effects of over estimating this height up to 20μm.

case almost no difference was noted between the surface currents calculated using this height and the best estimated sensing film height of 5μm. Overall, it may be concluded that the inversion scheme is rather insensitive to small errors in sensing film height.

Another factor to consider is the degree to which a field or current image may change by physically increasing the sensing film height. This can be investigated experimentally by placing a spacer of known thickness between a sample and a sensing garnet film. This was accomplished for the present work using a small 5×5mm wide piece of aluminum that had been measured to be 10μm thick. To estimate the effective sensing film height in this case required including this thickness

43
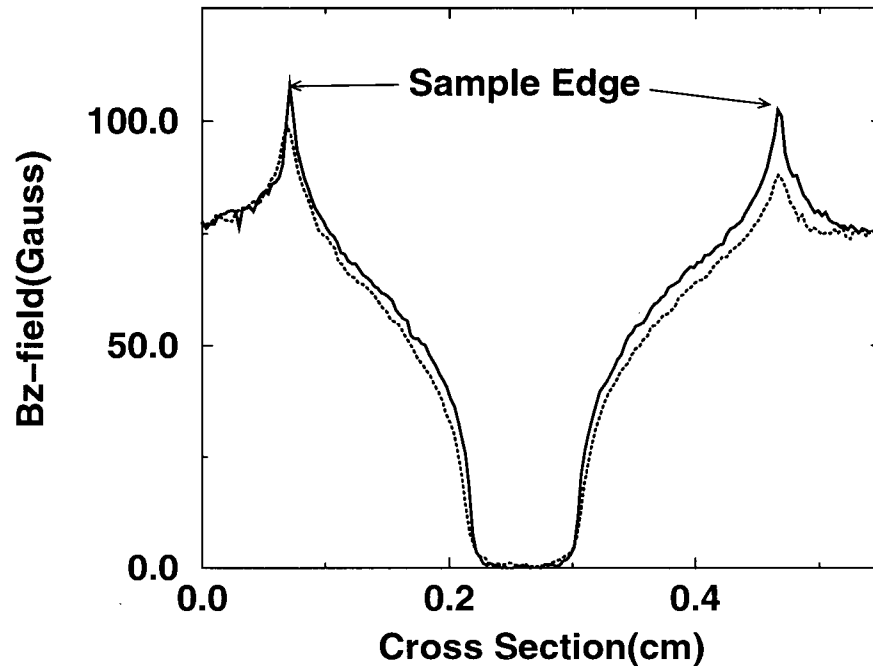
Figure 3.8: Comparison of local field strengths for a effective garnet film heights above the sample of 5μm, solid line, and 20μm, dotted line. In the latter case the local fields drop due to the increased sensing height.

along with the space that would have been present between the top surface of the sample and the bottom of the aluminum spacer and the top of the spacer and bottom of the garnet film. Each space was thought to contribute roughly an extra 5μm to the effective sensing height so that the total sensing height of the garnet film would have been approximately 20μm. In Fig.(3.8) a comparison is made between local field strengths measured using effective garnet film heights of 5μm, solid line, and 20μm, dotted line. In the former case, the sample was imaged without the spacer while in the latter case the spacer had been used to increase the garnet film height. It should be noted that in both cases the sample was held at 76K and was penetrated by a constant 75Gauss magnetic field. It is immediately apparent in Fig.(3.8) that increasing the garnet film height resulted in a small reduction in the measured local field strength, especially in areas where local field peaks were present. This is of

44
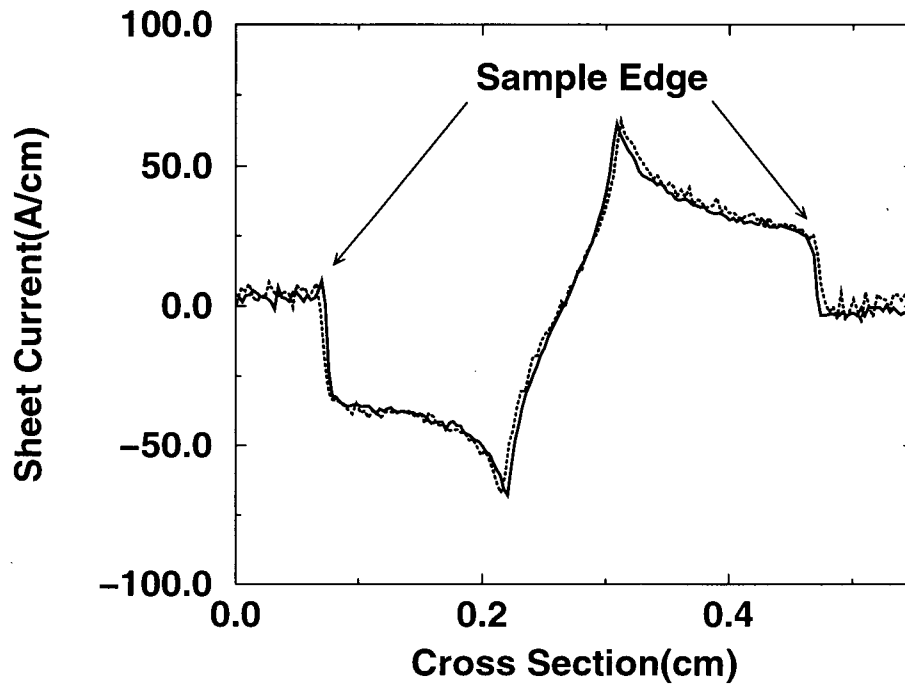
Figure 3.9: Comparison of calculated local sheet current for sensing garnet film heights of 5μm, solid line, and 20μm, dotted line. It is apparent that in this case no appreciable difference was observed in the current data for the two heights.

course to be expected since local fields would have been weaker further from the surface of the sample. A comparison is also made in Fig.(3.9) between the surface currents calculated from the local fields imaged using both heights. In this case the effective height parameter had been adjusted in the inversion scheme to compensate for the two heights used. This included the normal effective height 5μm, without the spacer, and the 20μm height associated with the use of the aluminum spacer. The results displayed in the cross sections of both figures indicate that while the increasing the height of the sensing film did affect the local measured fields it did not significantly affect the calculated local surface currents. This and the former results indicate that the calculation of local surface current is resistant to actual differences in sensing film height including errors that may be present in the estimation of the

film height parameter.

The field and current cross sections found without using the spacer are used in the further investigation of any current-field dependence and are thoroughly discussed in section 5.7 of chapter 5.

Chapter 4

Flux Penetration in Untwinned Crystals

4.1 Introduction

The magneto-optic technique has enabled the observation of flux dynamics that were previously hidden using other experimental methods. An interesting application of this technique is the study of flux penetration of thin rectangular superconductors. It has been established in the past that a barrier to flux penetration, called a geometrical barrier, is present when a steady magnetic field is applied perpendicular to a flat rectangular superconductor[21]. One way this phenomenon manifests itself is through the delay of flux penetration up to a penetrating field H_p. At applied field strengths below this value, no flux penetration is observed to occur, except along the outside edges of a sample. Applying a magnetic field larger than H_p, however, causes this barrier to disappear, allowing vortices to penetrate through the sample's edges. The dynamics of flux penetration in relation to this phenomenon also depend on the degree of pinning present in a superconductor. In the absence of pinning and above H_p, vortices accumulate in the center of a sample, leaving the inner edges flux free. In the presence of low to moderate pinning, vortices accumulate away from the center and as well as the inner edges. Similar dynamics associated with the no pinning case have been observed in in extremely low pinning $Bi_2Sr_2CaCu_2O_x$[21]. We have also observed, for the first time, evidence of a geometrical barrier in two

high quality $YBa_2Cu_3O_{6.95}$ single crystals. Normally, in this particular material, geometrical barrier effects are masked due to high pinning or heavy twinning which severely affects vortex motion. In this case, however, both crystals were grown in such a way as the reduce the presence of impurities, resulting in substantially few pinning centers[29]. One sample, a lightly twinned $YBa_2Cu_3O_{6.95}$ single crystal, originated from a batch of single crystals that exhibited ultra low pinning[30]. As a result, this enabled observation of the flux penetration dynamics associated with almost no pinning. The effects of higher pinning on flux penetration were also observed in the other untwinned $YBa_2Cu_3O_{6.95}$ single crystal, enabling a comparison of flux dynamics in relation to pinning. Reasonable agreement was established between these observations and a theoretical model of flux penetration in thin flat superconductors proposed by Zeldov et al[21].

4.2 Basic Theory of Flux Penetration in Relation to a Geometrical Barrier

Through the application of field perpendicular to the surface of a flat superconductor, a position dependent vortex potential is established. This position dependence, according to Zeldov, corresponds to the variation of the local fields in relation to sample geometry. Due to demagnetizing edge effects, local magnetic fields are enhanced near the edges of a sample; see Fig.(4.1). The result is a peak in the Lorentz forces exerted on penetrating vortices by Meissner surface currents producing a corresponding peak in the vortex potential and a barrier to flux penetration. In samples that have elliptical cross sections this position dependence is exactly compensated for by the variation of the vortex energy, caused by the variation of the sample thickness. This is not the case, however, in thin flat samples. Using a thin, rectangular superconducting strip model, Zeldov et al.[21] were able to show that vortex penetration will occur at substantially higher applied fields compared to penetration

(a) **(b)**
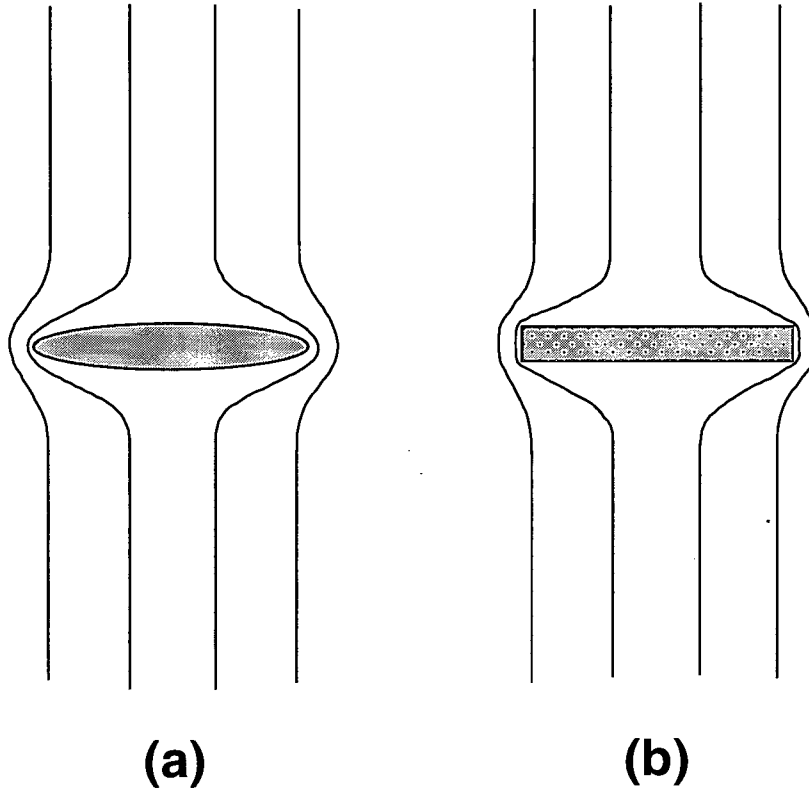
Figure 4.1: Representation of applied field distortion for (a) sample with elliptical cross section and (b) sample with rectangular cross section.

field strengths found in samples with elliptical cross sections. Due to the presence of a geometrical barrier, it was proposed that estimates of H_{c1} from penetration observations of a thin rectangular sample are overestimated by a factor of approximately $\sqrt{W/d}$, where $2W$ is the sample width and d its thickness. This will occur if the penetrating field strength is scaled by a standard demagnetizing factor without taking into account the flat rectangular geometry of the sample. The penetrating field in such a sample is actually $H_p = H_{c1}\sqrt{d/W}$ where H_{c1} is the bulk lower critical field for a type-II superconductor. Another feature associated with a geometrical barrier is a unique flux penetration pattern, present in flat rectangular samples that have moderate to almost no pinning. Below an applied field strength of H_p, vortices

will not penetrate beyond the sample edges due to the presence of the barrier. At or above this value, the barrier disappears and vortex penetration occurs, where the degree of penetration is largely dependent on the pinning present. In the absence of any pinning, Zeldov et al.[21] proposed that vortices will move directly to the central regions of a sample where the vortex potential is at a minimum. As the applied field is further increased, more vortices will enter the sample and accumulate in the center, resulting in a region of flux penetration that expands outwards towards the inner edges. This behaviour can be described by the function:

$$B_z(x) = \mu_o H_a \sqrt{\frac{b^2 - x^2}{W^2 - x^2}} \qquad (4.1)$$

where B_z is the z-component of the penetrating fields, $2b$ is the width of the flux penetrated region, H_a is the applied field strength and x is the cross section of the sample. The actual width of the penetrated region is given approximately by:

$$b \simeq W \sqrt{1 - (H_p/H_a)^2} \qquad (4.2)$$

for a sample with thickness d where $d \ll 2W$. The inner edges of such a sample will remain flux free up to an applied field strength of H_{c1}, the lower bulk critical field. At fields strengths above this value, vortices will cover the entire surface of the sample including its inner edges. In superconductors that have moderate to low pinning, the same dynamics associated with a geometrical barrier are present, except, in this case, pinning retards some of the inward vortex motion. Above H_p, vortices will once again enter the sample and move towards the inner regions. Basically, shielding currents with values greater than the critical current density J_c force entering vortices away from the edges of the superconductor and towards the center, where again the vortex potential is at a minimum. Unlike the no pinning case, however, vortices then become pinned further into the crystal where the shielding surface currents are weaker with intensities similar to the critical current density[21]. The result is flux free areas in the central regions as well as along the inner edges

of the sample. These penetrating field dynamics are described by the function:

$$B_z(x) = \mu_o H_{c1} \frac{J_c}{J_E} f(x) F(x) \qquad (4.3)$$

where:

$$F(x) = \sqrt{\frac{(x^2 - a^2)(b^2 - x^2)}{(e^2 - x^2)}} \qquad (4.4)$$

and where the term $f(x)$ is given by the integral:

$$f(x) = \frac{2x}{\pi} \left[\int_a^b \frac{ds/F(s)}{x^2 - s^2} + \frac{J_E}{J_c} \int_e^W \frac{ds/F(s)}{x^2 - s^2} \right] \qquad (4.5)$$

The first term of the integral expression is evaluated over the limits a and b which represent the inner and outer edges of the flux penetrated regions, respectively, while the second term is evaluated over the width the edge current J_E, postulated to be $d/2$, half the sample's thickness, where in the lower limit $e = W - d/2$. According to Zeldov[21] the penetrating flux forms symmetric regions of width $a < |x| < b$ that change size around the center of a low pinning sample in response to a changing applied field. Increasing the applied field causes these regions to expand symmetrically, represented by a decrease in a and a corresponding increase in b. Increasing the applied field forces more vortices to enter the sample, which in turn causes the regions of flux penetration to expand towards the central regions and outwards to the inner edges. These areas will eventually cover the entire sample surface when the applied field is increased beyond the bulk lower critical field H_{c1}. The degree to which the penetrating vortices initially accumulate away from the center of a sample is largely dependent on the sample's pinning or critical current density J_c in relation to the edge current J_E. The stronger the pinning or critical current J_c, the greater is the tendency for the vortices to become pinned before reaching the central regions. Consequently, the initial areas of flux concentration form further away from the center of a superconductor and nearer its edges as the amount of pinning increases. Eventually, the dynamics associated with strong pinning are recovered when $J_c \gg J_E$. In this case penetration starts on the edges of the sample and moves towards the center as the applied field is increased.

4.3 Samples and Experimental Procedure

Two samples were studied, both $YBa_2Cu_3O_{6.95}$ single crystals, grown by a CuO-BaO flux method[29]. The crystals had been detwinned and annealed with one becoming slightly twinned again in one corner after annealing. The slightly twinned crystal, sample A, happened to have the weakest pinning characteristics of either sample and had a significant twin boundary in one corner and one irregular edge. Its dimensions were $a= 722\mu m$, $b=740\mu m$ corresponding to the longest edge, and its thickness was $c=10\mu m$. The other sample, sample B, was completely untwinned and had rectangular dimensions, where $a=636\mu m$, $b=750\mu m$ and $c=11\mu m$. Both crystals had a superconducting transition temperature, Tc, of approximately 93K. Sample A was imaged at 78K and sample B was imaged at 80K. The crystals were glued with GE varnish to two silicon chips which in turn were placed in thermal contact with the copper cooling block with high vacuum silicon grease. Silicon grease has proven, in the past, to provide superior results under temperature cycling. It provides better contact between the sample and block during temperature cycling than does Apiezon grease which tends to crack under such conditions. Cool down and image processing followed the procedure described earlier in chapter 2. The usual image subtraction process was employed. Since the samples had relatively weak pinning characteristics, both were imaged with a larger than normal number of averaged images. In this case, 256 averaged images were used for each sample in order to properly resolve their local flux dynamics.

4.4 Critical Remnant Images of the Untwinned and Nearly Untwinned Crystal
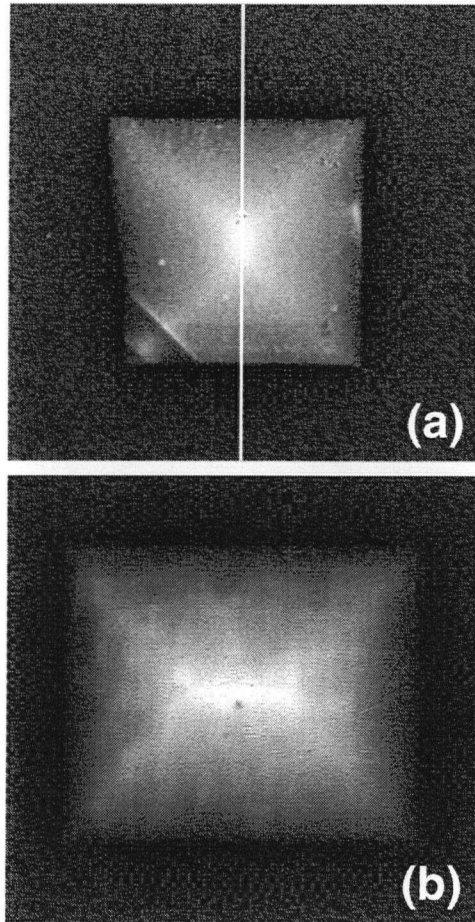
Figure 4.2: The critical remnant field distributions of crystals A and B are displayed in images (a) and (b), respectively. Field peaks were present in the centers of both samples. It is apparent in (a) that vortices were blocked by the single twin boundary in the bottom left corner of crystal A.

In Fig.(4.2) are shown the critical remnant state images (a) and (b) of samples A and B respectively. The gray scale intensities of both images represents the local remnant field strengths, where the lightest areas are of opposite polarity to the darkest areas. Both images were produced by momentarily applying a strong magnetic field above 200 G and then imaging the resulting local field distributions after
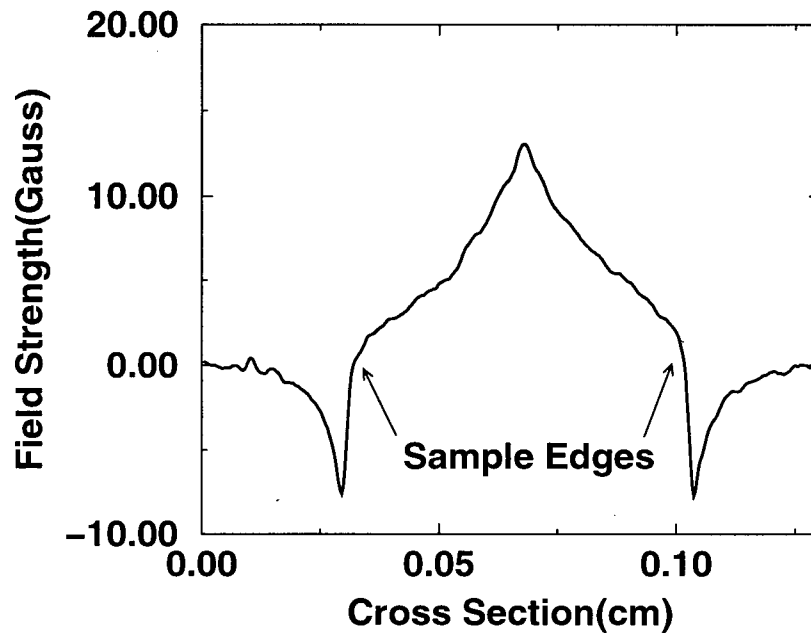
Figure 4.3: Vertical cross section, indicated by white line in Fig.(4.2), taken of sample (a) remnant fields. Demagnetizing effects are apparent in this graph, where significant fields were in the vicinity of the sample edges, indicated on graph. It can also be seen in this graph that the flux peaked in the center of the sample at 13 Guass.

the applied field was removed. Noticeably, peaks in the remnant fields were present in the centers of both samples as indicated by the lightest regions, where the field peak in sample A was 13 G and the peak in sample B, 35 G. The remnant fields in both samples also exhibited an X-like pattern, a result of their rectangular geometries. Another feature common to both images was a darkened area along the outer edges of both crystals which indicated the presence of fields of opposite polarity to the surface remnant fields. This effect was probably associated with the interaction of stray remnant fields with the edges. Since both crystals were relatively thin their edges would have had a significant demagnetizing effect on any local stray fields, producing significant edge fields. A cross section taken of the sample (a) remnant fields is displayed in Fig.(4.3), where significant edge fields are apparent. Noticeably,

these fields diminished quickly away from the sample, dropping to negligible values approximately 300μm from the edges. Another intriguing feature of the sample (a) image was the apparent influence that the twin boundary, in the lower left corner of the crystal, had on the local remnant field distribution. It is apparent, in this case, that the twin boundary acted like a barrier to transverse flux motion. This is indicated by the shadowed area which is closely accompanied by a light region along the twin boundary facing the central flux peak. The barrier-like behaviour of twin boundaries to transverse flux motion has been previously reported, where a buildup of flux on the sides of boundaries was observed in twinned $YBa_2Cu_3O_{6.95}$[31]. In our case, after the applied field was turned off, vortices traveled from the central regions of the sample, towards the outer edges. It appears in image (a) of Fig.(4.2) that the vortices were blocked by the twin boundary causing a buildup of flux on one side of the boundary and a corresponding lack of vortices on its opposite side, in effect producing a flux shadow. It was observed that the peak field intensity along the boundary was 9 G while the minimum field intensity in the shadowed area was 2 G. It should be noted that most of the noise present in both images, seen as small specks, was caused by the garnet film.

4.5 In-Field Images and their Remnant Counterparts
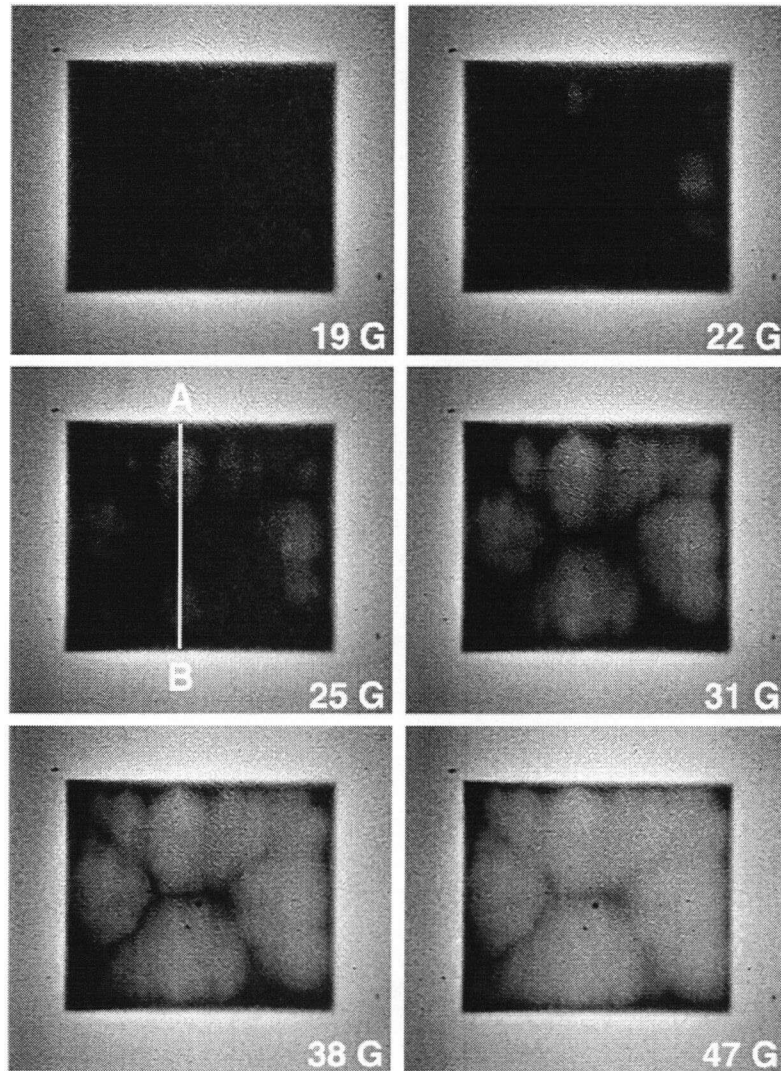
Figure 4.4: In-field behaviour of crystal B is shown for increasing applied fields. Penetrating vortices initially avoided the inside edges and central regions of the sample which is indicative of a geometrical barrier in a low pinning sample. Field profiles were taken along the A-B line shown on the 25 Guass image.

The in-field behaviour of the untwinned crystal, sample B, at six different applied field strengths is shown in Fig.(4.4). The strongest local fields are represented by the lightest areas and the weakest by the darkest regions. Initially, at an applied field of 19 G no flux penetration was observed to occur. Vortices only started to accumulate in regions near the inside edges at 22 G. Increasing the applied field further caused these areas to grow in size and to become more numerous until at 47 G they almost covered the entire surface of the sample. A persistent feature of the in-field images was the apparent tendency of the flux penetrated regions to avoid the inside edges and central regions of the crystal. As previously mentioned, this effect is a characteristic of a geometrical barrier in a moderate to low pinning sample. In this type of sample, penetrating vortices have a tendency to become pinned further into the crystal where the local shielding currents drop to values equivalent to the critical current density J_c. Flux penetration was also observed to occur more readily along the middle edges of the sample than through the corners. This is evidence of the discontinuity line effect, a phenomenon that is present when surface currents are forced to perform sharp bends by the corners of a sample[32]. Demagnetizing edge effects were also noticed in all six images manifested as light areas outside the sample edges, indicating an increase in the local fields in these regions. It is apparent that this phenomenon was strongest near the middle edges of the crystal, an effect expected for demagnetizing effects in a rectangular geometry. Remnant fields in sample B, produced by the same applied field strengths are displayed in Fig.(4.5). In this case, the images were captured immediately after removal of the specified applied field enabling the observation of remnant flux dynamics. Once again, the remnant fields and their intensities are represented by either light or dark regions, with the lightest areas being of opposite polarity to the darkest areas. Comparing both Figs.(4.4) and (4.5) it can be seen that there was an overall similarity between the in-field and remnant field images produced by the lower applied fields. This was especially true at 22 and 25 G where the remnant field patterns were virtually iden-
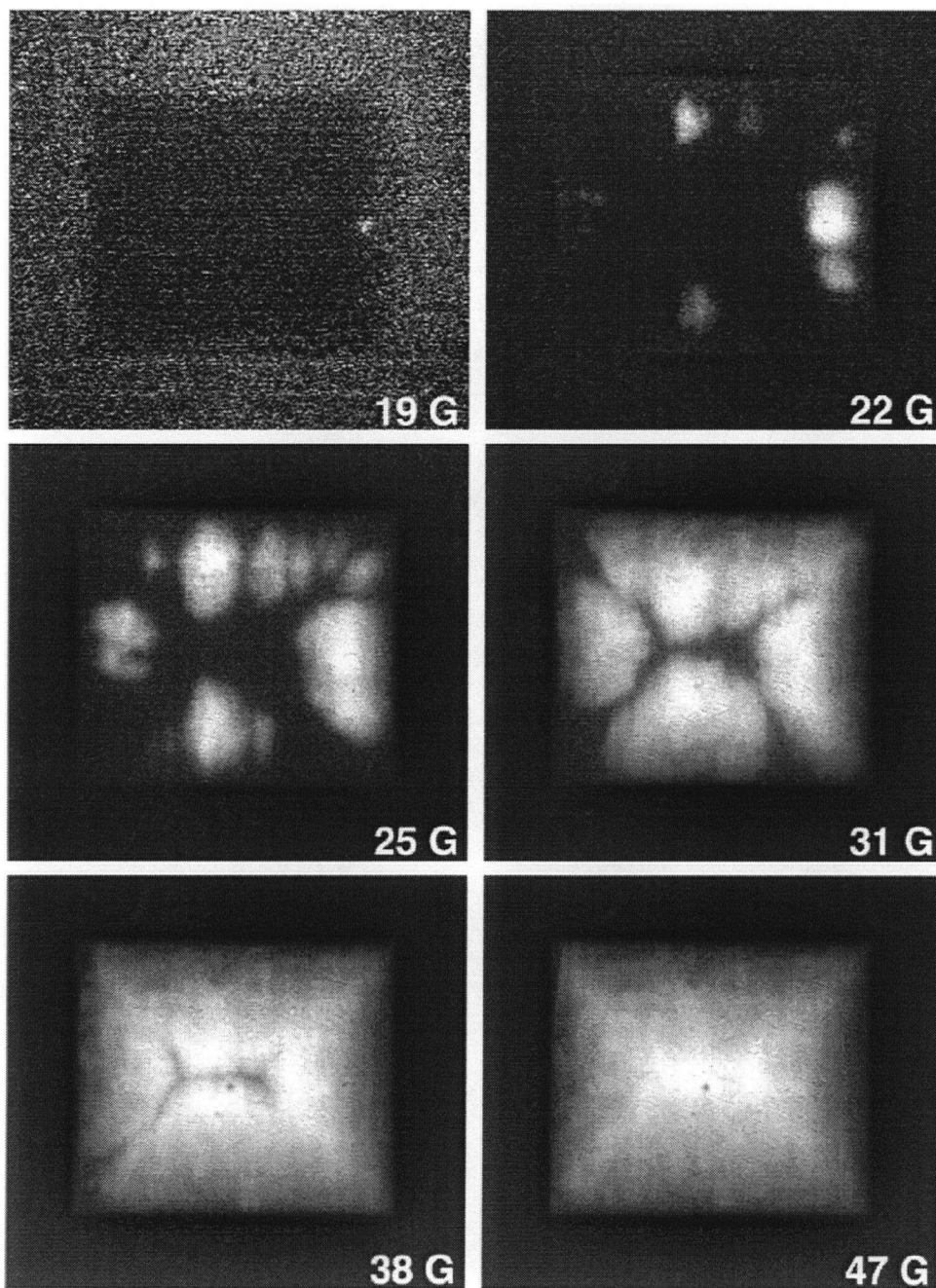
Figure 4.5: Remnant field distributions of crystal B caused by the indicated applied fields. These flux patterns were similar to the in-field patterns especially at the lower applied fields. At higher fields the shape of the crystal started to have an effect on the overall remnant flux patterns, resulting in a more critical remnant state distribution.

tical to the in-field patterns of Fig.(4.4) for the same applied field strengths. The effects of the crystal's rectangular geometry on the distribution of flux in the remnant state, however, became more apparent after the application of the higher fields. At 31 G the remnant fields started to conform to the edges of the crystal producing a slightly rectangular distribution with a central flux free region. This effect became more noticeable at 38 G. In this case the flux free central region shrank while the overall flux pattern acquired a distribution more like that observed for the critical remnant state. Eventually, at 47 G, the remnant fields acquired a distribution close to the one observed for the critical remnant state in Fig.(4.2) and with a similar central field maximum. These dynamics can be easily understood by considering the combined effects of pinning, mutual vortex repulsion and the overall influence of the crystal's rectangular geometry. The remnant field patterns associated with the lowest applied fields were similar to the in-field images simply because the penetrating vortices were pinned in place after the applied fields were removed. Applying higher fields, however, would have resulted in a greater vortex density and a larger vortex interaction throughout the crystal. As a result the remnant flux distribution produced by higher fields would have conformed more readily to the rectangular geometry resulting in a more critical state-like distribution.

The in-field flux penetration dynamics of sample A at 80K are displayed in Fig.(4.6) where again, the largest fields are depicted by the lightest areas and the weakest fields, by the darkest regions. At the lowest applied field of 15 G, vortices suddenly accumulated at the center of the crystal. Increasing the applied field up to 30 G caused this flux penetrated region to grow in size, out from the center of the sample, while leaving the inner edges flux free. This type of behaviour is typical of a geometrical barrier in a flat sample with virtually no pinning. Actually, the vortex filled regions produced at the lowest applied fields were a little wider than that predicted by Zeldov's theory[21] for an ideal zero pinning sample, which most likely indicates the presence of an extremely small yet still non-zero amount

59
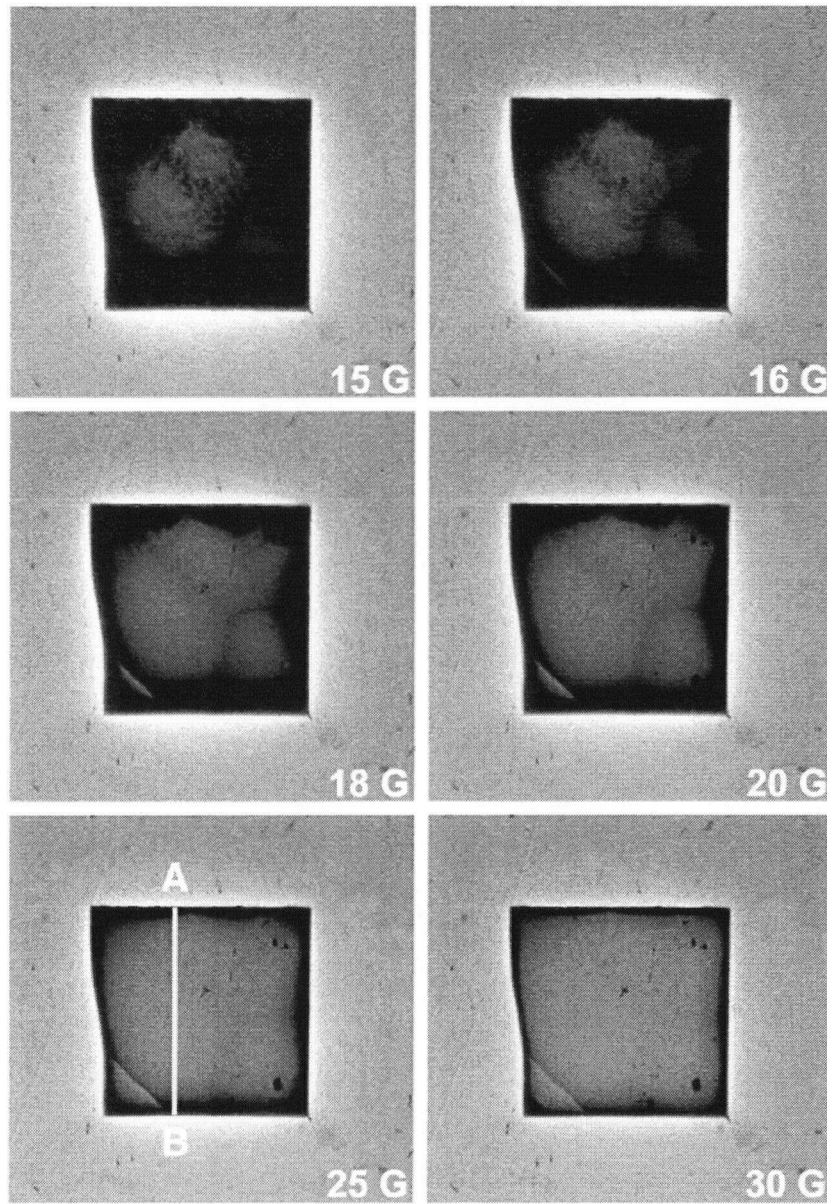
Figure 4.6: Flux penetration in crystal A caused by increasing applied fields. A concentration of vortices initially occurred near the central region of the sample and away from the edges at 15 Gauss which is a characteristic associated with flat samples that have extremely low pinning. Some entering vortices were blocked by the twin boundary in the lower left corner of the crystal, denoted by the light region along the boundary in the middle row images. Flux profiles were taken along the A-B line shown on the 25 Gauss image.

of pinning in sample A. This point is discussed further in the next section. Another interesting feature of the 18 and 20 G in-field images was the tendency of the twin boundary in the lower left corner of the crystal to act as a barrier to the penetrating vortices. This is noticeable as a light region along the boundary facing away from the center of the sample, indicating a buildup of vortices in this region. Obviously, some vortices were blocked by the twin boundary as they entered the sample, resulting in a buildup of flux on one side of the boundary and in a lack of flux on the opposite side. This is the same behaviour as that observed in Fig.(4.2) of the previous section except the barrier is now preventing the inward movement instead of the outward flow of vortices.

An additional important feature of the in-field penetration dynamics was the tendency at 80K, of flux penetration to occur in the untwinned regions of the sample and not along the twin boundary. Remnant field patterns, produced by the application of the lowest applied fields of 15-18G are displayed in Fig.(4.7). At 15 and 16 G the remnant fields were pinned in generally the same locations on the sample's surface as in the in-field case, although in this case they exhibited more dispersed flux patterns. At 17G the formation of a remnant peak was already noticeable along with a corresponding reduction of remnant field strengths towards the sample edges indicating that the sample geometry was already starting to have an effect on the flux distribution. This tendency was also observed for the 18 G image except the remnant fields were starting to acquire a critical state distribution with similar peak field values and twin boundary field values as those found in the critical state image of Fig.(4.2).

A very noticeable feature common to all four remnant images was the tendency of the vortices to form intricate branching structures comprised of flux penetrated and flux free regions. This effect, which is not seen in the critical remnant state image of Fig.(4.2) (a), was the product of slight inhomogeneities within the sample and not just random patterns. This was confirmed by repeatedly heating
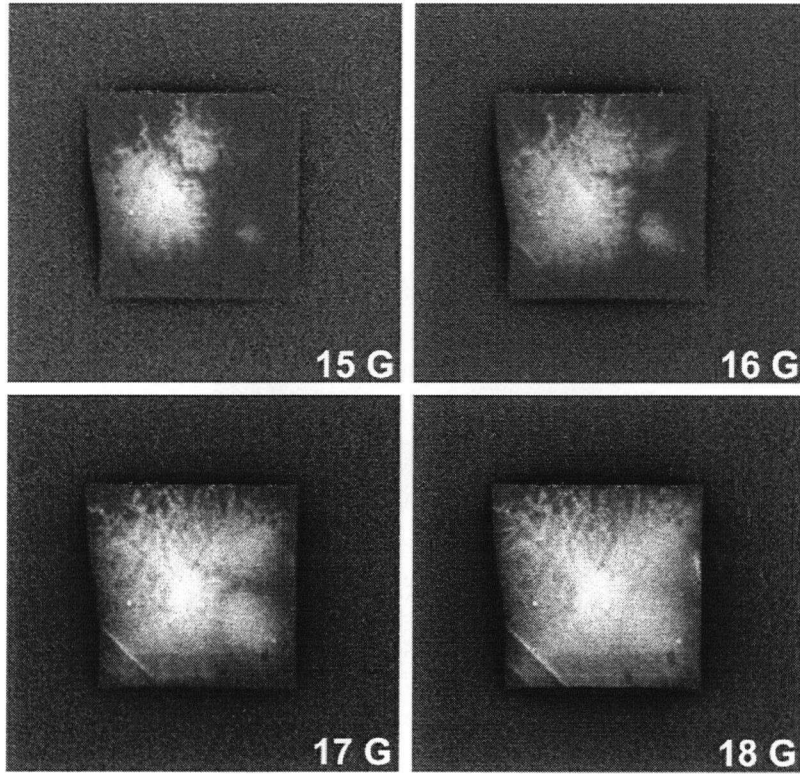
Figure 4.7: Remnant field distributions of crystal A caused by the indicated fields. These distributions tended to have a more dispersed structure compared to the in-field case, caused by local pinning inhomogeneities within the crystal.

the crystal above and below T_c and noting that the resulting field patterns did not change. The formation of these branch-like flux structures were primarily due to the absence of significant pinning. After removal of the applied field, vortices would have moved substantial distances from each other because of extremely low pinning, before they were trapped by Meissner currents or pinned by whatever little pinning was present in the sample. Consequently, small variations in pinning would then become noticeable due to the differential pinning of the vortices in the crystal resulting in the filamentary flux structures.

4.6 Discussion
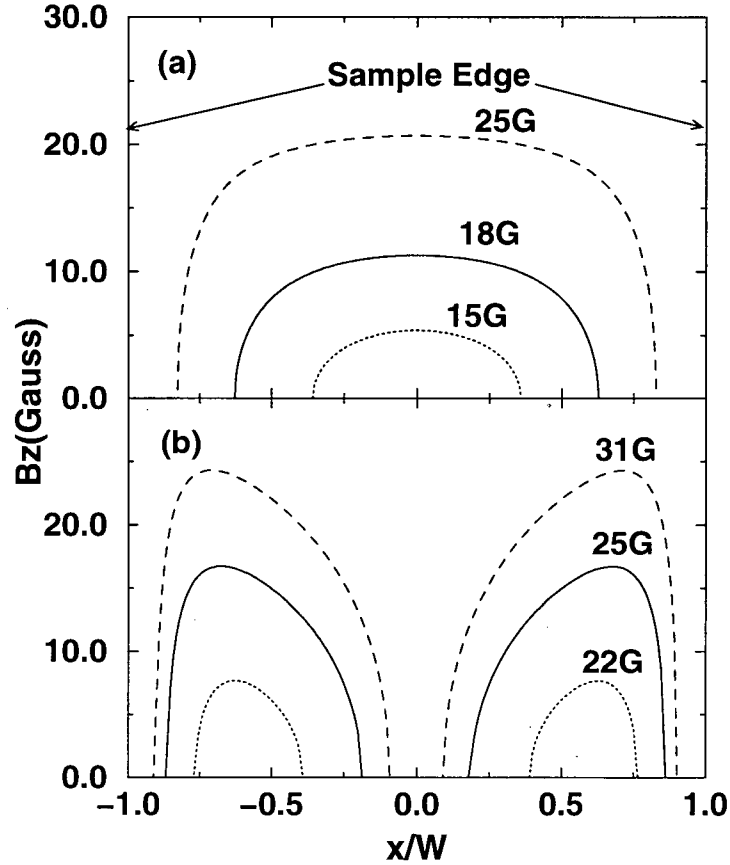
Figure 4.8: Theoretical penetration profiles calculated for a thin superconducting strip. In graph (a) are the profiles for a zero pinning sample and in graph (b) are the profiles for a low, non-zero pinning sample. In the zero pinning case, vortex accumulation initially occurs in the central regions while in the low pinning case, two areas of flux are initially formed away from the center. The applied fields are also indicated for each profile.

It is possible, using the model devised by Zeldov et al.[21], to make a comparison between theoretical field profiles of flux penetration in thin flat superconductors with our experimental observations. In Fig.(4.8) are theoretical B_z profiles of a thin strip superconductor of infinite length having a width of $2W$ and thickness d. In this

case, the field is applied perpendicular to the surface of the strip, along the z axis at the strengths indicated in both graphs (a) and (b) of Fig.(4.8). These profiles were calculated numerically using actual experimental applied field strengths and the observed flux penetration cross-sections from both samples while using Eq.(4.1) for the upper plots of Fig.(4.8) (a) and Eq.(4.3) for the lower plots of Fig.(4.8) (b). In the graph (a) are the field profiles of flux penetration in an ideal zero pinning thin strip superconductor and in graph (b) are the profiles of a similar superconductor having a small amount of pinning. In both cases flux penetration is indicative of the geometrical barrier effect. In the no pinning case, graph (a), flux initially accumulates in the center of the sample expanding outwards as the applied field is increased. In the low pinning case, vortices accumulate in two symmetric regions that tend to avoid the center and edges of the sample. Increasing the applied field causes these regions to expand in size and intensity while the flux free regions correspondingly diminish. Experimental field penetration profiles are displayed in Fig.(4.9) for both samples A and B produced by the indicated applied fields. The top plots in graph (a), in Fig.(4.9) are cross sections of experimental field penetration in sample A, the sample with extremely low pinning and the bottom plots in graph (b) are cross sections taken from sample B, the sample with higher pinning. In both cases, the profiles were taken along the A-B lines indicated in Figs.(4.4) and (4.6) where the ends of the lines correspond to the edges of the crystals. In order to get results that approximated the dynamics caused by a thin strip geometry special attention was given to the actual positioning of the A-B lines. Both lines were placed where the greatest symmetry in flux penetration was observed to occur, around the middle regions of both samples. In addition to this, the cross section of sample B was taken along the shortest width of the crystal's surface in a further attempt to approximate a thin strip geometry. Comparing the theoretical and experimental profiles of both crystals it is immediately apparent that, unlike the theoretical case, large edge fields were present near the inside edges of both samples,

64
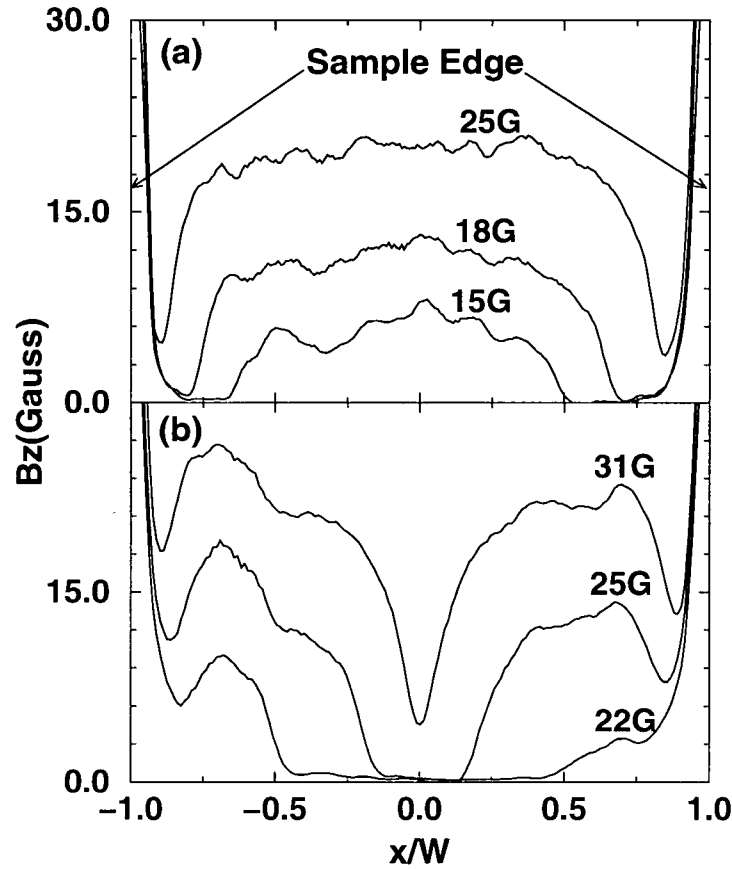
Figure 4.9: Experimental Bz penetration profiles taken along the A-B lines indicated in Figs.(4.4) and (4.6). In graph (a) are profiles from crystal A, an extremely low pinning sample and in graph (b), profiles from crystal B, a low pinning sample. Positions of vortex accumulation in both samples were similar to those predicted by theory in the last figure.

as indicated by both graphs in Fig.(4.9). This was caused by large dispersed fields passing through the garnet film in the vicinity of the edges and not a real phenomenon associated with any penetration dynamics. Since the garnet sensing film was at an effective height above both samples, due to its thickness, these fields would have passed through the film further in from the edges, producing the apparent edge profile peaks. By further examining the experimental profiles of sample

65

B in Fig.(4.9) it is also apparent, that unlike the theoretical case, the central flux free region started to disappear at an applied field of 31 G. Once again, this effect was most likely caused by fields spreading out from nearby flux penetrated regions. These fields would have intersected the garnet film further into the central regions, due to its effective height, resulting in the appearance of a nonzero field profile in these regions. Comparing the experimental field profiles of sample A with the theoretical profiles plotted in graph (a) of Fig.(4.8) it can be seen that while there is general agreement between the two the experimental profiles tended to be wider at the lowest applied fields. This effect was most likely caused by a small amount of pinning being present in sample A. At applied field strengths just above H_p, penetrating vortices would have been forced towards the center of the sample by Meissner currents. The presence of any pinning, however small, would have caused these vortices to become pinned before reaching the center, resulting in separate flux penetrated regions that quickly combined at slightly higher applied fields to form a field profile wider than that predicted for the zero pinning case. At the higher applied fields, these areas of vortex concentration formed a central region more comparable to that seen in a theoretical sample with no pinning. By comparing the experimental profiles of sample B with their theoretical counterparts in graph (b) of Fig.(4.8), it can be seen that there is also general agreement between the two, although less than that found in the sample A, no pinning case. The theoretical profiles in graph (b) of Fig.(4.8) were fitted to the corresponding experimental profiles of sample B in Fig.(4.9) (b). This was done by varying the ratio of the critical current density, J_c, with the edge current density, J_E and repeatedly evaluating Eqs(4.3), Eqs.(4.4) and (4.5) for x, the theoretical cross section of a sample. By varying this ratio in the theoretical model an optimum fit to the experimental profiles was found and consequently it was then possible to determine, approximately, the ratio of J_c/J_E for sample B. In doing this the value of the ratio was determined to be $J_c/J_E \approx 0.09$ or in other words, the sample's edge current

density was approximately 11 times larger than its bulk critical current density.

While overall agreement was achieved between the theoretical description and our experimental observations of flux penetration in low pinning samples, even better results could probably be obtained using a model that would take into account the effects of a rectangular surface geometry. It was observed that penetrating vortices had a tendency to avoid the corners of our rectangular samples, an effect that is not considered in the thin strip model devised by Zeldov et al.[21]. Since most samples do not have a long thin strip geometry, such an effect would have to be an intrinsic part of any general model describing flux penetration and the geometrical barrier in low pinning thin rectangular samples.

4.7   Conclusion

Observations of flux penetration in two high quality $YBa_2Cu_3O_{6.95}$ single crystals confirmed the presence of a geometrical barrier, a phenomenon usually masked by high pinning or heavy twinning in this particular material. Two distinct penetrating field patterns were observed caused by the different pinning characteristics of the crystals. In one case, vortices were observed to accumulate in the center of the sample, while avoiding the inside edges indicating an extremely low degree of pinning. In the other case, vortex accumulation tended to form away from the central regions of the sample as well as along the inner edges indicating a higher degree of pinning. Observations of these flux penetration dynamics was consistent with geometrical barrier effects as described by Zeldov et al.[21]. Reasonable agreement was found between our observations and Zeldov's theoretical model of flux penetration derived for thin superconducting strips with rectangular cross sections.

Chapter 5

Flux Penetration in a Circular Thin Film

5.1 Introduction

Of the many techniques available the magneto-optic imaging process provides the most direct and efficient means by which field penetration of a sample can be observed. Penetration of a thin film having a circular geometry can be especially interesting when an attempt is made to correlate experimental observations with the theoretical models developed specifically for this geometry. Additional computational techniques such as those described in chapter 3 help to further enhance the imaging technique providing quantifiable local current values. Of further interest are the effects of anisotropic superconductivity which is an important feature of many of the high temperature ceramic superconductors. The present sample under investigation described in section 5.3 was no exception as it was comprised of a thallium based compound which has been established in the past to be very anisotropic[33]. Thallium high temperature superconductors are also of special interest due to their low microwave losses and their relatively high critical currents. Using a circular thin film of this material, sample penetration by a magnetic field was observed, and a comparison was made with a two dimensional penetration model

developed by Mikheenko et al.[23] for a circular superconducting sample. Utilizing the augmented iteration of chapter 3, it was also possible to observe the effects of the anisotropic nature of this particular material on the sample critical current, and to observe the dependence of such effects on the sample temperature.

5.2 Summary of Theory Concerning Field Penetration of a Circular Thin Film.

The analytical modeling of flux penetration of a superconductor by a magnetic field can be a challenging problem mathematically. Complications arise when the external field is applied perpendicular to the sample's surface which causes substantial modification of the field, especially in the vicinity of the edges. The problem can be exacerbated even further by certain sample geometries, such as in rectangular crystals where sample corners tend to distort the local fields to a significant extent. An analytical solution to the problem, however, has been derived by P.N. Mikheenko et al.[23] using a simpler infinitesimally thin circular geometry. This derivation provides a solution for both current and field patterns in this geometry, for constant as well as periodically varying external fields. This theory has proven to be of some use when analyzing flux penetration of a circular thin film by a constant, weak, perpendicular magnetic field. In deriving the model Mikheenko assumed the superconductor in question was an infinitesimally thin disk of radius R with an axially symmetric current distribution. Sufficiently strong pinning was also assumed to prevent penetration by very weak fields. In addition to this Mikheenko employed critical state theory which asserts that surface currents must be at critical levels in regions wherever vortices are present in a superconductor. In adopting this theory, a variety of models can be employed concerning the dependence of the pinning force on the local vortex density. One of the simplest, termed the Bean model[34], involves assuming that the pinning force is independent of local field strength which
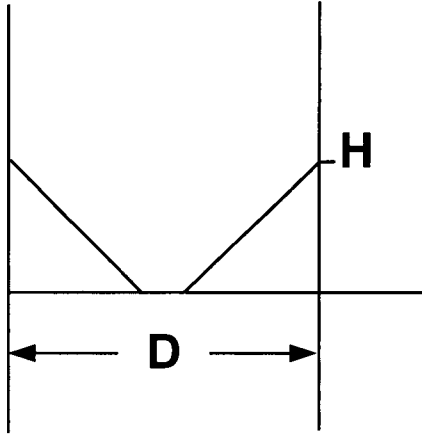
Figure 5.1: Demonstration of Bean's model for an infinitely long slab of width D with a magnetic field H applied parallel to its surface. In this case, due to the parallel field orientation, demagnetizing edge effects would be insignificant. The field strength drops linearly as it penetrates the sample. The slope of this drop corresponds to the local critical current strength which according to this model would be constant.

implies that a spatially constant critical current will be present in regions of flux penetration; see Fig.(5.1). In Mikheenko's model, a sufficiently strong magnetic field applied perpendicular to a circular thin film of radius R would produce a flux penetrated annular region encircling a flux free center. This central region, having a radius of a where $a < R$, would result from the central Meissner shielding currents effectively expelling the applied field. The outer annular region would, according to the Bean model, be associated with a uniform annular critical current. As the applied field was increased, more flux would enter the outer rim of the film, causing the penetrated annular region to grow in size towards the center of the sample. At a sufficiently strong field, this penetrated region would eventually cover the entire surface of the sample. The relation governing this behaviour was derived by Mikheenko[23] to be:

$$a = R/\cosh\left(\frac{H_0}{H_c}\right) \tag{5.1}$$

where H_0 is the applied field strength, $H_c = \mu_o \Lambda_c/2$ is the characteristic critical field, μ_o is the permeability of free space and Λ_c is the critical surface or sheet current

70

having units of Amps/m. Similar behaviour can also be seen by increasing the sample temperature causing a drop in the characteristic field value and a decrease in the Meissner radius. The shielding surface current of the central region was also found by Mikheenko to be:

$$\Lambda(r) = -\Lambda_c \frac{2}{\pi} \arctan\left[\frac{r}{R}\sqrt{\left(\frac{R^2 - a^2}{a^2 - r^2}\right)}\right] \tag{5.2}$$

for $r < a$. These relations were established using a standard equation that links the z-component of a magnetic field close to the surface of a thin disk to the radial configuration of its current where:

$$H_z(r, z \simeq 0)/H_0 = 1 + 1/(\pi(H_0/H_c)) \int_0^R G(r, \rho) f(r) d\rho \tag{5.3}$$

For this particular geometry the currents are represented by current loops centered at $r = z = 0$ where:

$$G(r, \rho) = \frac{1}{\sqrt{((\rho + r)^2 + z^2)}}\left[K(k) + \frac{\rho^2 - r^2 - z^2}{(\rho - r)^2 + z^2}E(k)\right] \tag{5.4}$$

and $k^2 = 4\rho r/((\rho+r)^2 + z^2))$. Also $K(k)$ and $E(k)$ are the standard complete elliptic integrals of the first and second kind and $f(r) = \Lambda(r)/\Lambda_c$. In addition to this the ratio of H_0/H_c is governed by the size of the Meissner radius according to Eq.(5.1) where in our case the applied field H_0 is held constant while the characteristic critical field H_c varies with sample temperature. In the flux expelled region where $r < a$ it must be true that $H_z/H_0 = 0$ while in the field penetrated annular region where $a < r < R$, $H_z/H_0 > 0$. These conditions must hold true in the presence of the applied field H_0 which includes the self fields produced by the sample. In adopting the Bean model for the current distribution in the field penetrated region Mikheenko[23] established that it was possible to determine an exact analytical solution to this problem using the radial current distribution represented by Eq.(5.2).

A theoretical profile of the surface currents associated with these dynamics is plotted in Fig.(5.2) for a general case of a film with radius R having an inner
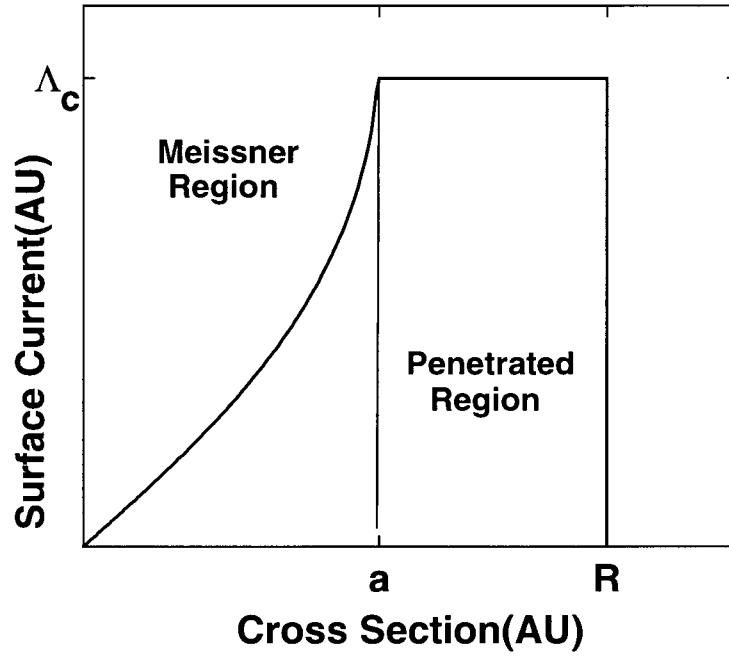
Figure 5.2: Theoretical plot of surface current for a thin superconducting disk. Both axes are given in arbitrary units. The penetrated annular region is, according to the Bean model, associated with a uniform critical surface current. In the Meissner region the surface current drops in strength away from the penetrated region and goes to zero in the center of the sample.

Meissner region of radius a. As indicated by the profile, the region of penetration, where $a < r < R$, would correspond to a uniform surface critical current Λ_c. Further in towards the film's center these currents would start to drop below the critical value at radius a defining the inner Meissner region and drop to zero at the center. Such behaviour can be understood physically by considering the geometrical aspects of a flat disk placed perpendicular to an applied field. In this case, fields near the edge of the Meissner region would be significantly enhanced due to demagnetizing edge effects inducing significant surface currents in these regions. Towards the center of the disk the applied field would tend to drop in strength resulting in a corresponding decrease of the surface shielding currents away from the penetrated region.

5.3 Sample and Experimental Procedure

The flux penetration characteristics of a $Tl_2Ba_2CaCu_2O_y$ circular thin film, provided by Superconducting Technologies Incorporated of Santa Barbara California, were observed using the magneto-optic imagining apparatus described in chapter 2. The film had a thickness of approximately 7000Å, was 4mm in diameter and had been deposited on a 0.38mm thick MgO substrate. The superconducting transition temperature of the sample was determined to be approximately T_c=100K using AC susceptibility measurements and was independently confirmed using the magneto-optic apparatus. This was achieved by conducting real time field penetration observations of the sample as it was slowly warmed up through T_c and noting the temperature that precipitated the onset of full field penetration. Thermal contact between the film and copper cooling block was established using high vacuum silicon grease which provided reliable results for this experimental setup. The uniformity and high quality of the sample under investigation was established by capturing its remnant field image at 78K displayed in Fig.(5.3) of the next section using the techniques described in chapter 2. In summary this image was produced by briefly applying a 200 gauss field to the sample then capturing the resulting trapped flux after the field was turned off. The field was then reapplied, but in the opposite direction and the process repeated. In-field images of the film displayed in Figs.(5.6) and (5.7) were acquired using a similar process, except the applied field was left on as the images were captured. In this case, the penetration dynamics caused by applying a relatively weak field of 10Gauss were observed for different sample temperatures. Imaging calibration and subtraction techniques were also employed to obtain quantifiable results for both types of images and are described fully in chapter 2.

5.4 Remnant Field Image
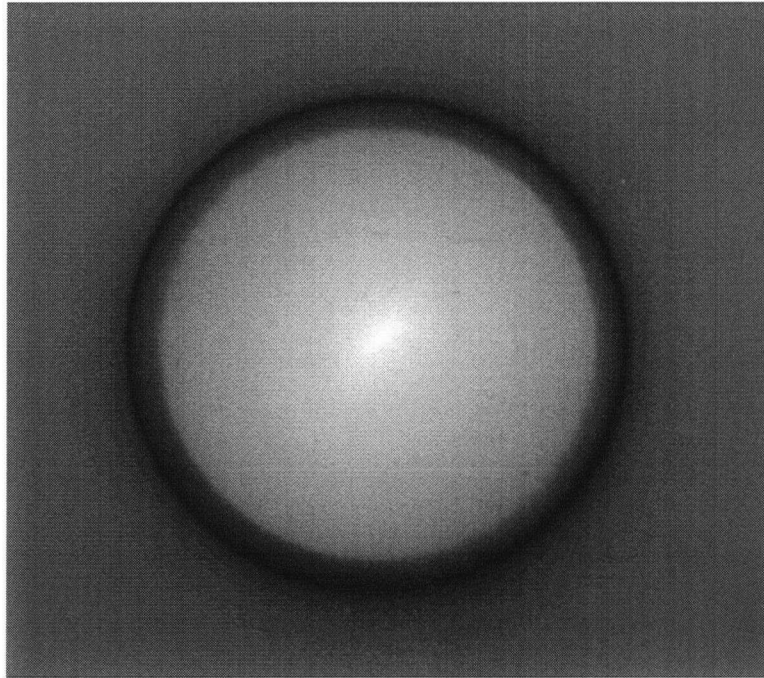
Figure 5.3: Remnant field image of circular thin film produced by STI. The strongest fields and their polarities are represented by the lightest and darkest regions. A central flux peak was present in the center of the sample, represented by the light point which was surrounded by an area of negative vortices indicated by the dark annular region. The high degree of flux symmetry and the lack of significant defects suggested a thin film of high quality.

A remnant field image of the sample is shown in Fig.(5.3) where the darkest and lightest regions indicate the presence of the strongest fields having opposite polarity. From this image it is apparent that the remnant flux readily conformed to the circular geometry of the sample producing a sharp peak field in its central region. Also present was a dark annular section situated around the inside edge of the film. This is an effect typically seen in many thin films and originates from negative flux produced by stray fields from the central flux peak being trapped by pinning in these regions. Such an effect is not seen in much thicker samples, such as in the single crystals studied in chapter 4 simply because the stray central remnant fields
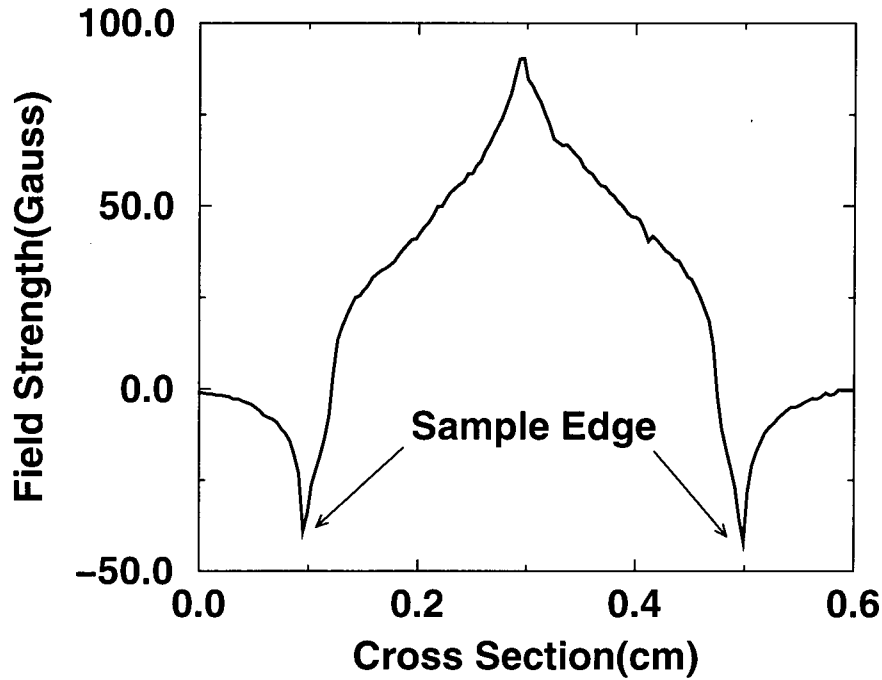
Figure 5.4: Cross section of remnant fields present in the thin film at 78K. The edges of the sample are depicted in the figure where it is indicated that negative flux was present around the inside edge of the thin film. The cross is very symmetrical indicating a uniform sample.

would have to be much stronger to penetrate the edges. A horizontal cross section taken of the remnant fields is displayed in Fig.(5.4). It is apparent that pinned flux from the stray central fields induced negative fields around the inside edge of the sample. This is in contrast to profile observations plotted in Fig.(4.3) of crystal (a) in chapter 4 where it can be seen that stray fields reversed polarity just outside the crystal edges. On closer inspection of the thin film profile it becomes apparent that remnant fields dropped from a central maximum peak of 82Gauss down to zero around the inside edge of the sample and then reversed polarity increasing in strength towards the edge. The fields then dropped quickly to negligible values outside the film away from the edge. The symmetry of the profile is also very apparent in this figure suggesting a sample of high quality. The uniformity of the
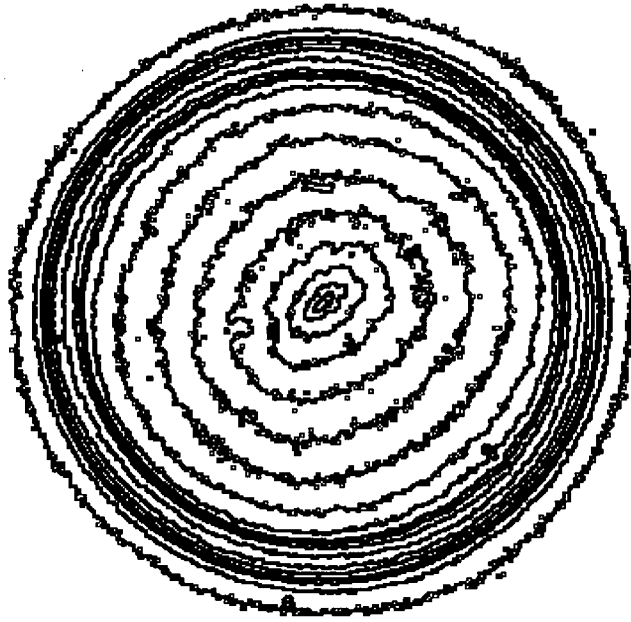
Figure 5.5: Field contour lines demonstrating the uniformity of the thin film sample. In this case the contour lines were not prefectly circular indicating a slightly imperfect sample.

sample can also be examined in Fig.(5.5)) using field contour lines. In this case it can be seen that while the sample is very uniform as demonstrated in Fig.(5.3), a very slight asymmetry in the field distribution is actually present which is indicated by the contour lines which are not perfectly circular. A perfectly uniform circular thin film would produce a perfectly circular field distribution that would conform to the sample geometry. This clearly demonstrates the power of field imaging to find even the smallest sample imperfections and validates its utility in the quality control of thin film superconductors.

5.5 In-Field Dynamics

Field penetration dynamics of the thin film at various temperatures are displayed in Figs.(5.6) and (5.7). A total of 23 in-field images were taken of the sample, from 78K up to and including 100K, its superconducting transition temperature. Only 12 images are actually displayed in the figures for brevity. In both figures the largest fields are depicted by the lightest image areas while the smallest fields are indicated by the darkest areas, with the black regions suggesting the absence of any flux. Also included in Fig.(5.8), are several field penetration profiles of the sample over the same temperature range. Profile position is represented in Fig.(5.6) by the horizontal line in the top left in-field image. The dark central region covering most of the sample's surface in the same image indicates that at 78K flux was largely expelled by the film. At increasing temperatures, this area of Meissner expulsion shrank leaving a partially field penetrated annular region around the inside edge of the sample that eventually covered the entire surface at 100K in Fig.(5.7). Penetration of the film with increasing temperature can be examined in the field profiles of Fig.(5.8). The expulsion of the field was very pronounced at the lowest temperature, where the sample profile in the figure indicates an almost complete lack of flux in the inner region. As the temperature was increased, the constant applied field began to penetrate the outer rim of the film and the central Meissner region correspondingly shrank in diameter. At 100K, full penetration of the sample was achieved and resulted in a flat field profile of 10Gauss, the strength of the applied field. A noticeable feature of the profiles and of most of the in-field images were significant fields on the edge of the sample. This phenomenon is observable as a light ring encircling the sample in the in-field images, indicating the presence of fields significantly larger than the applied field. It is also present in the in-field profiles of Fig.(5.8) where peaks larger than the applied field can be seen near the sample edge. Although these peaks did diminish as the sample temperature increased, they tended to persist almost up to the superconducting transition temperature. Physi-
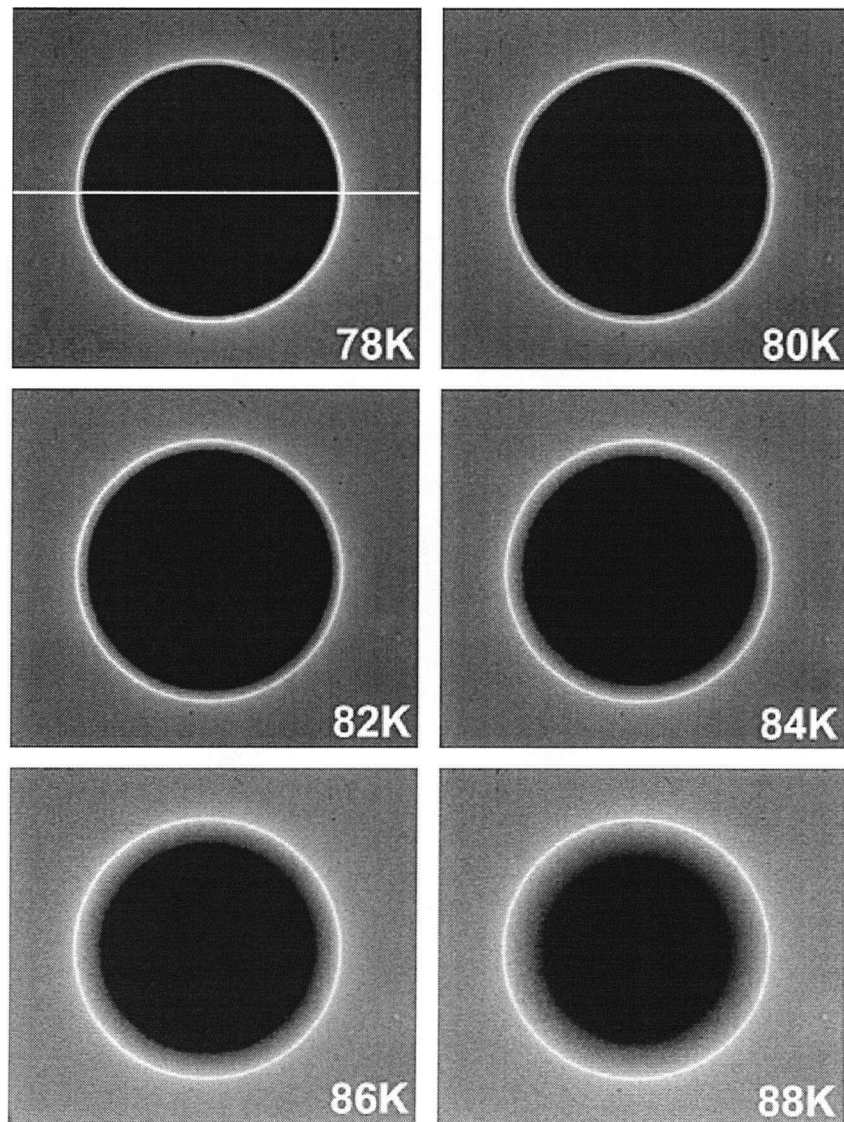
Figure 5.6: In-field images of flux penetration by a 10Gauss field with increasing temperature. At the lowest temperatures, flux was mostly expelled from the center of the sample, indicated by the dark central region. As the temperature was increased, partial penetration occurred in an annular region around flux expelled center.
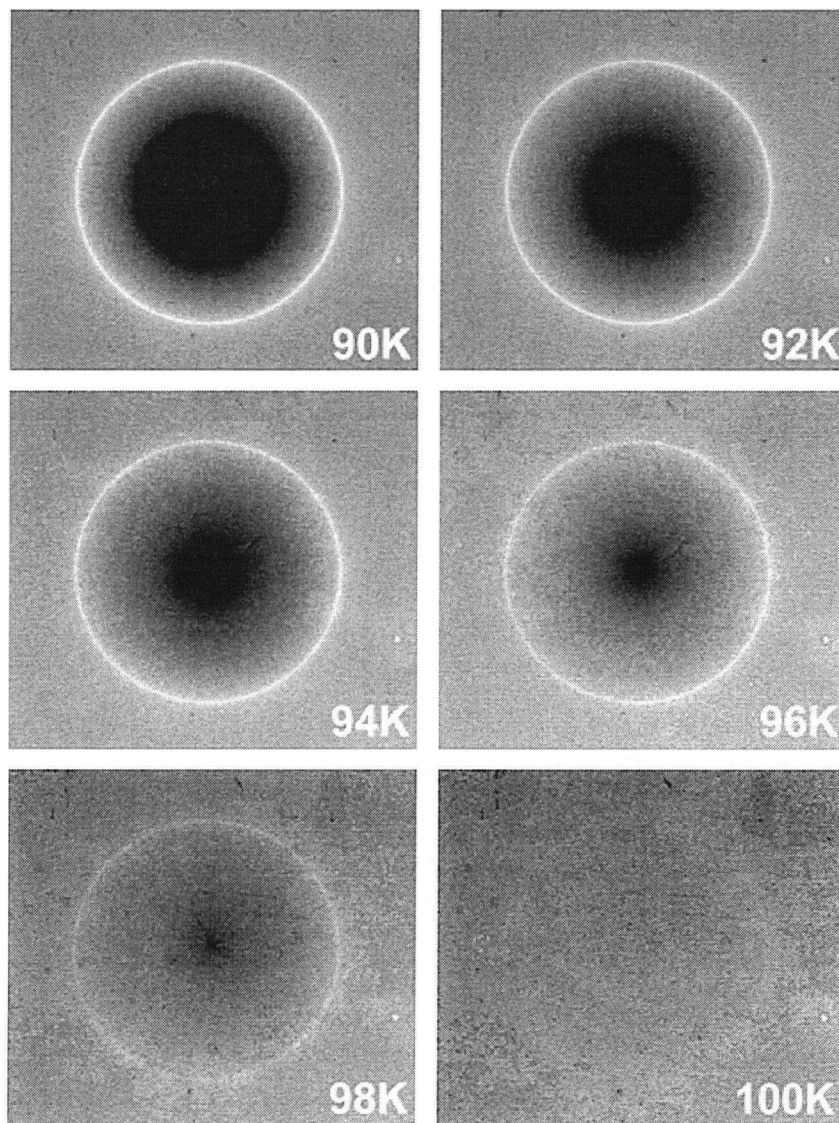
Figure 5.7: Continuation of penetration of the sample with increasing temperature. The annular penetrated region grew in size until it covered the entire sample surface at 100K. In almost all the images of both figures, significant edge fields were present, indicated by the light circle along the sample edge.
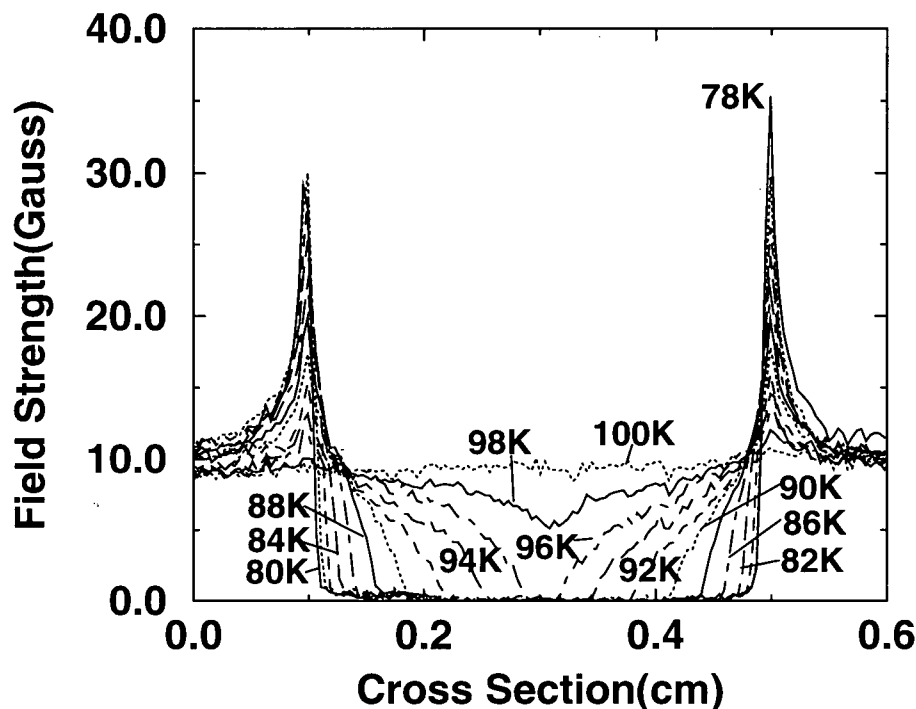
Figure 5.8: Cross section of field penetration of the sample from 78K to 100K. Penetration tended to occur more readily around the inner edges of the film than near the outer edge of the central flux expelled region as predicted by theory. Significant edge fields were also present which tended to diminish at higher temperatures.

cally this is probably due to the persistence of the mixed state in the annular region of the thin film. Some superconductivity would have still been present near the inner sample edge even with substantial penetration of its total surface area. As a result, local fields would continue to be influenced, even if only partially at higher temperatures, by demagnetizing edge effects. This effect is also well described by Eq.(5.3) for H_z using Mikheenko's model. Using the known radius of the Meissner region for various sample temperatures it is possible using Eq.(5.3) to calculate numerically the cross section of the penetrating z-field component. By carefully measuring the radius of the flux expelled region with changing sample temperature the dependence of radius size with temperature was found and is plotted in Fig.(5.9). This data can
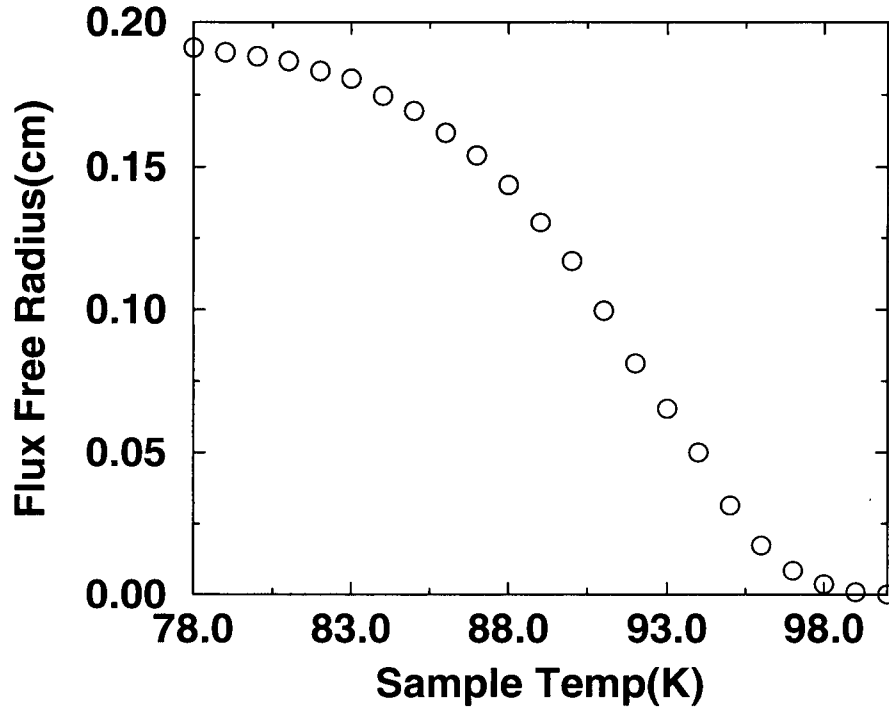
Figure 5.9: Radius of inner Meissner region with increasing temperature indicating a non-linear dependence with sample temperature.

also be used to calculate directly surface or sheet currents by substituting the size of the Meissner area into Eq.(5.1) and solving for the characteristic critical field. A comparison is conducted later in this chapter between critical surface currents calculated from the augmented iteration described in chapter 3 with values found using this more direct method. It is apparent from this figure that at the lowest temperature of 78K, the radius of the Meissner region was already slightly smaller than the radius of the film, since a small amount of penetration had already occurred. As the temperature was increased, this region slowly shrank at first and then, at more moderate temperatures, decreased more rapidly, indicating that the degree of flux expulsion had a non-linear dependence with temperature. Just below the transition temperature, the radius once again began to shrink less rapidly until at 100K it disappeared completely. Using this data and Eq.(5.3) the z-component of field pen-

81
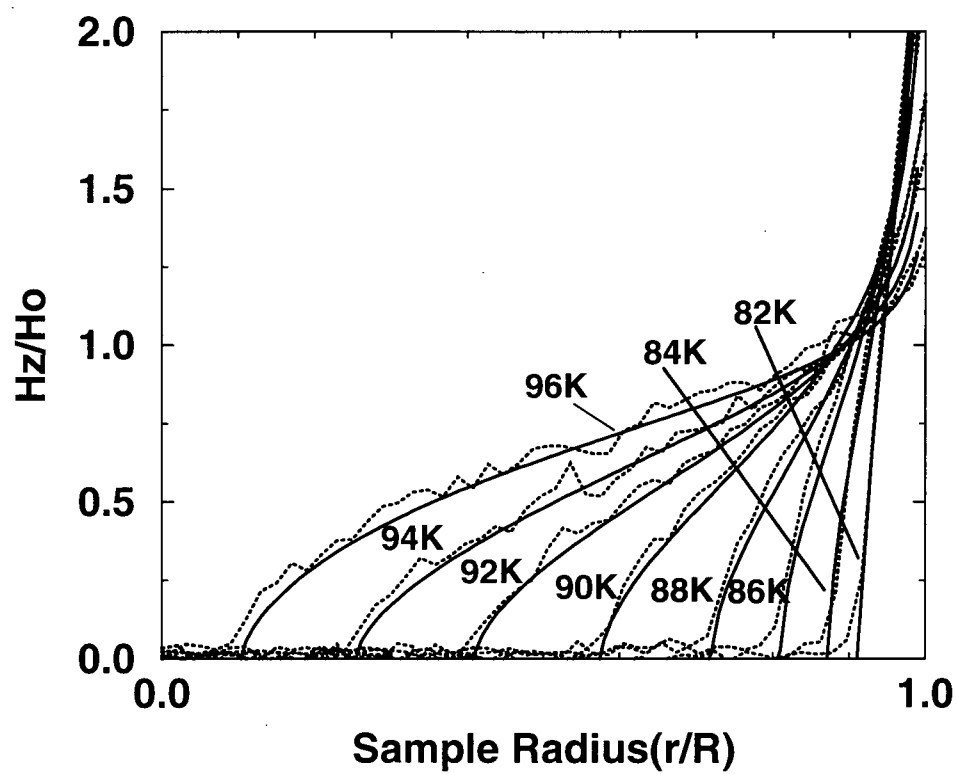
Figure 5.10: Comparison of the measured radial distribution of the normalized z-component, dotted lines, and calculated distribution, solid lines, for the indicated sample temperatures. It is apparent that both the experimental and theoretical distributions closely match.

etration was calculated for various sample temperatures and compared to some of the measured penetrating field cross sections displayed in Fig.(5.8). It was sufficient to use only the right half of the cross sections to make adequate comparisons with the calculated z-components in Fig.(5.10). Despite some imaging noise the measured cross sections of field penetration, dotted lines, compared well with the calculated distributions, solid lines. Also present and predicted by theory was the presence of substantial fields near the inner region of the sample with strengths greater than the applied field H_0. Noticeably, the highest edge fields occurred according to the theory at the lower sample temperatures where $H_z/H_0 \geq 2$. This was observed experimentally where for example $H_z \sim 50$Gauss at 78K and $H_0 = 10$Gauss.

5.6 In-field Surface Current Dynamics

Since the in-field images of Figs.(5.6) and (5.7) had been calibrated, it was possible to use the augmented iterative algorithm, described in chapter 3, to calculate the local sheet magnetization dynamics and the corresponding sample surface currents. In order to do so, we first subtracted the applied field from the measured local fields to get the sample self-induction, the quantity actually required for processing. The results are displayed in Figs.(5.11) and (5.12) for the same temperatures as those indicated in Figs.(5.6) and (5.7) of the last section. A half-cross section, indicated by the white line in the top left image of Fig(5.11), was also taken of the sheet currents over the sample temperatures of 78K to 96K. Cross sections at the highest temperatures were not included since the surface currents became lost in image noise. The data are analyzed and are discussed in the next section of this chapter. It should be noted that the lightest regions in both Figs.(5.11) and (5.12) indicate the presence of the largest surface currents. The outer black regions denote the absence of any detectable current surface current, which is a reasonable result, since the sample was not present in this area. It must also be noted that all the images in these figures have been normalized so that flux structures that became weaker with temperature could still be seen clearly. As a result, even though the outer current ring may seem not to change significantly in brightness over most of the sample temperatures, the sheet currents responsible for this region actually became substantially weaker with increasing temperature. This is made apparent by examining the cross sectional plots of Fig.(5.13) in the next section. Initially , at the lowest temperatures, sheet currents peaked around the inner edge of the sample while surface shielding currents covered most of the film, corresponding to the dark area in the sample center. The shielding currents tended to decrease towards the center of the film, as predicted by Mikheenko et al.[23], which is evident in most of the images of both Figs.(5.11) and (5.12) where the center of the Meissner region is noticeably darker compared to its inner edge. This effect, which is also confirmed in

84
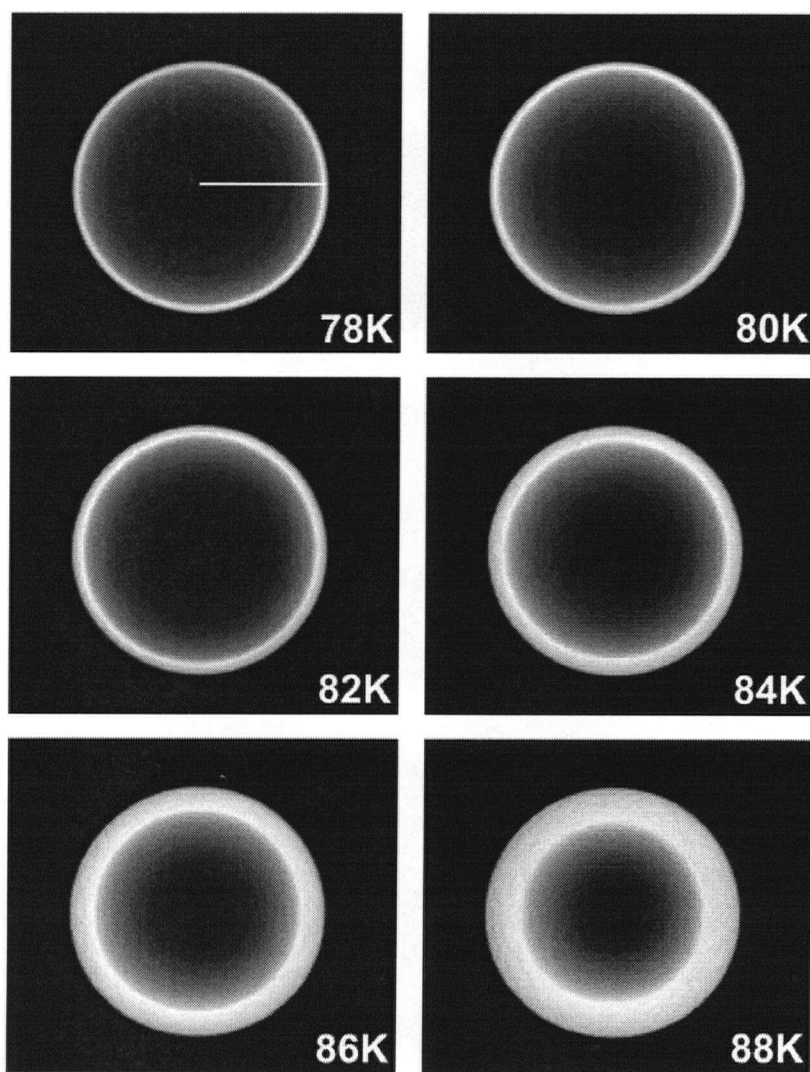
Figure 5.11: Sheet currents calculated using the augmented iteration of chapter 3. Significant surface currents were present around the edge of the film at the lower temperatures while shielding surface currents which decreased in strength towards the sample's center expelled the applied field producing the Meissner region.
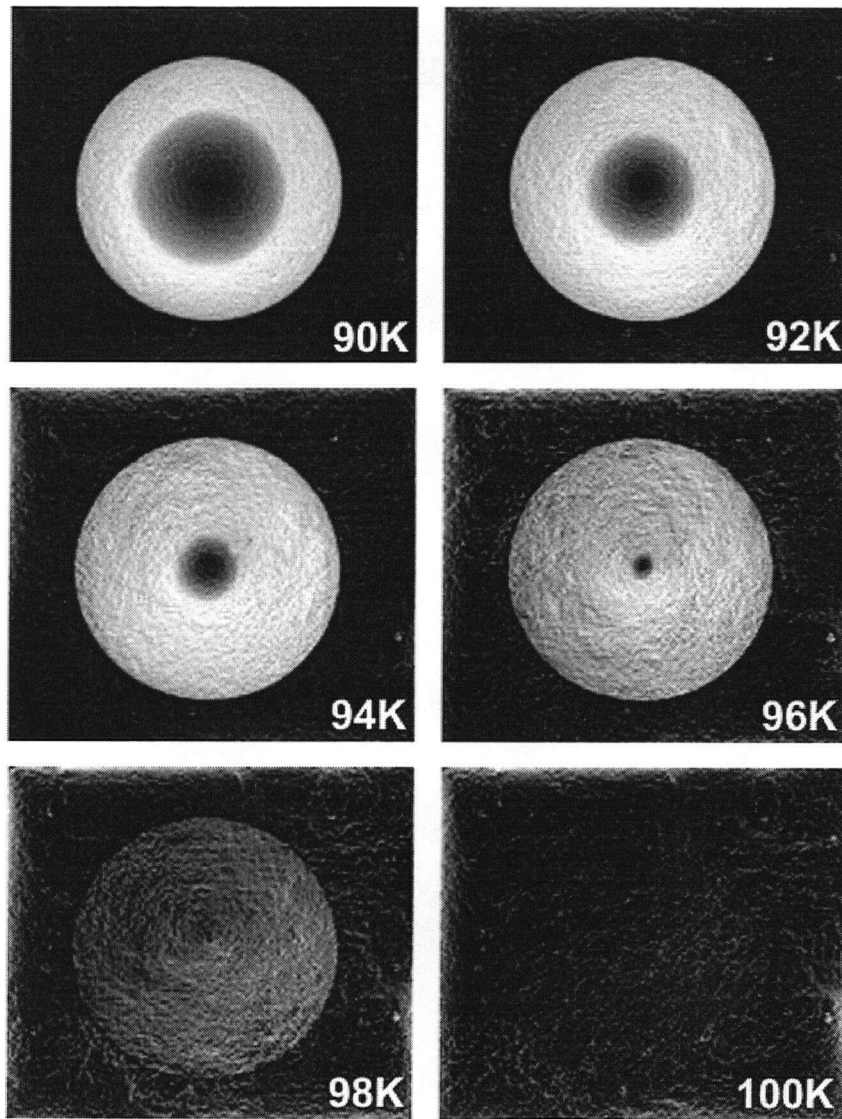
Figure 5.12: With increasing temperature, the central shielding currents became less extensive shrinking towards the central regions while the currents in the flux penetrated annular region covered more surface area. In this figure and Fig.(5.11), the largest sheet currents are indicated by the brightest regions, while the absence of any currents is depicted by the darkest or black areas.

the profiles of the next section, was the result of the decreased strength of the applied field due to sample geometry. The applied fields would have tended to be stronger near the edges of the sample and weaker near the center requiring smaller central shielding sheet currents. Increasing sample temperature caused the surface currents in the flux penetrated annular region to widen while the currents responsible for expelling the field from the center of the sample retreated back towards the center. At the highest temperatures, flux penetration covered almost all the sample surface and at the superconducting transition temperature of 100K, the surface currents disappeared below the image noise.

5.7   Quantitative Current Results.

By plotting cross sections of the surface sheet current distribution and comparing the results with the theory of Mikheenko it has been possible to acquire some insights into the behaviour associated with the penetration phenomenon. Specifically, the uniformity of the sheet currents in the outer penetrated rim of the sample can be compared with theory and the dependence of the critical current with temperature can be established. Half-cross sections of the sample sheet current calculated from the experimental B_z values are plotted in Fig.(5.13). The current cross sections are plotted at 2K increments starting at 78K corresponding to the highest edge current peak up to and including 96K the temperature at which the surface currents had dropped significantly. As observed previously in the current images of Figs.(5.11) and (5.12) surface currents were greatest around the inside penetrated rim of the sample. At the lowest temperature of 78K it can be seen in Fig.(5.13) that sheet currents up to 50A/cm were present along the edge region. Flux expulsion from the rest of the sample was associated with a screening surface current that decreased smoothly from critical current strengths at the penetrated rim down to zero at the center of the sample. With increasing temperature surface currents dropped significantly allowing more flux to enter the sample increasing the size of the penetrated
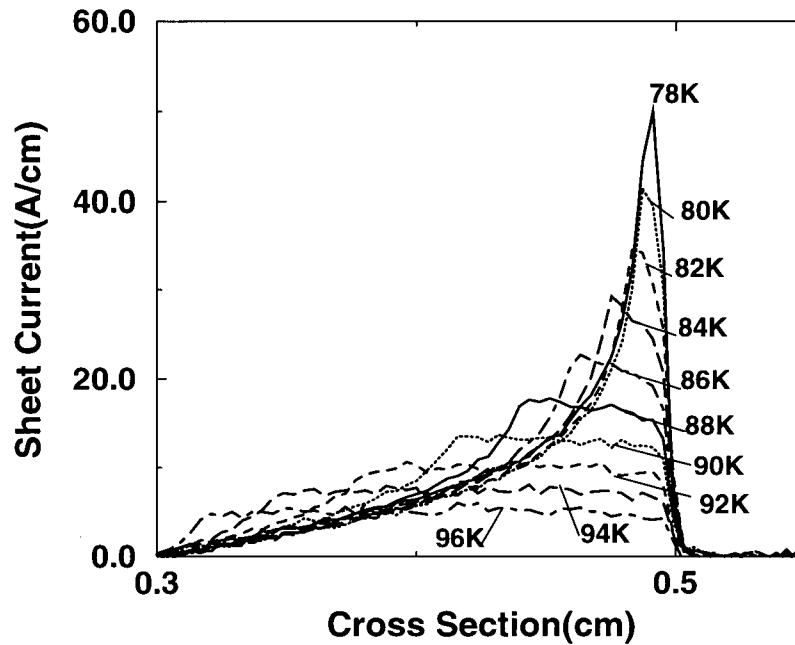
Figure 5.13: Half cross section taken of sample sheet currents for temperatures from and including 78K to 96K. Currents around the edge and in the penetrated region dropped quickly as the sample temperature was increased.

region. At 96K penetration of the sample was almost complete resulting in almost no Meissner region and a critical current in the penetrated region that had dropped to no more than 5A/cm. A comparison of experimental profiles with profiles calculated using the theory from Mikheenko et al is shown in Fig.(5.14) for two sample temperatures of (a) 84K and (b) 92K. It can be seen in both graphs that there was excellent agreement between the experimental and the theoretical profiles for the central flux expelled region. It should be noted that both graphs are representative of most of the data fits found for the Meissner region from 78K to 94K. At or above 96K the region of penetration covered almost the entire surface of the sample, resulting in virtually no Meissner region, making it difficult to perform a proper theoretical data fit. While the theoretical and the experimental current profiles for the flux expelled region were very similar, this did not appear to be the case for the flux penetrated
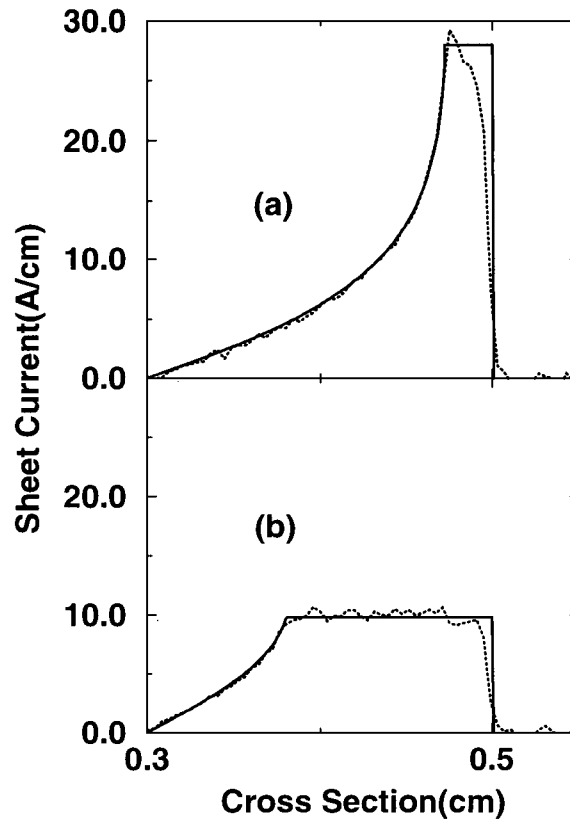
Figure 5.14: Comparison of experimental and theoretical cross sections of the surface sheet current for (a) 84K and (b) 92K. As can be seen in both plots, agreement between the two is excellent for the central flux expelled region. In (a), however, at the lower sample temperature, surface current does not appear to be radially uniform through the penetrated rim.

regions at the lower sample temperatures. Surface current strength did not appear to be uniform across the penetrated region as predicted by Bean's model. Instead, it tended to increase, in towards the outer rim of the Meissner region where the local penetrating fields were weaker. This tendency is very noticeable in Fig.(5.14) (a) for 84K, where it can be seen that sheet currents nearest the outer sample edge were lower than those near the inner Meissner region. It can also be seen in the many of the plots of current cross section of Fig.(5.13) at the lower temperatures. While it may be tempting to conclude from this that sheet current strength and local field

89
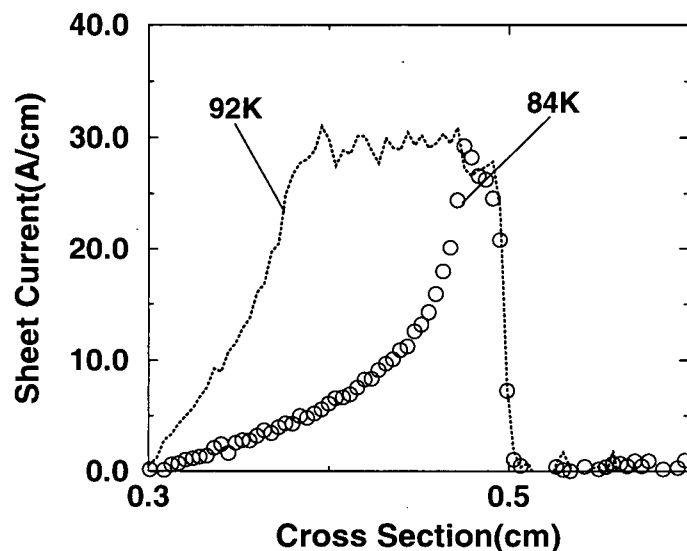
Figure 5.15: Comparison of 92K and 84K sheet current cross sections. The 92K data has been enhanced by a multiplicative factor of 2.5 to enable a comparison with the 84K data. It can be seen in this figure that any supposed position dependence of the sheet current is not significant when a comparison is made with a higher temperature profile having a larger flux penetrated radius.

strength are correlated in some way numerical errors caused by insufficient image resolution must also be considered. Significant edge fields were present at the lower temperatures and were confined along a relatively small radius of the sample since field penetration in this case was restricted along the inner rim region. Since the entire sample was imaged at once this would have limited the number of imaging pixels available to capture the fields along the edge causing data imaging spikes in this region. It has been observed by the author that such spikes, which indicate a loss of imaging resolution, have a tendency to cause anomalous sheet current distortions when processed by the augmented iteration. This effect also has a tendency to rapidly disappear further away from any field spikes in areas where imaging resolution is not a problem. The spurious nature of the apparent current variations is also emphasized in Fig.(5.15) where a comparison is made between the 84K and 92K current profiles of Fig.(5.14). In this figure the higher temperature data, repre-

90

sented by the dotted line, has been enhanced with an arbitrary multiplicative factor in order to make a comparison with the lower temperature data indicated by the small circles. Noticeably, the currents present in the flux penetrated region at 84K occupy only a small fraction of the sample compared to the region covered at 92K making any current variations appear insignificant. In addition to this, there appears to be a slight tendency for the 92K current data to also decrease towards the outer sample edge similar to the 84K data. Considering the potential problem of data spikes and their affects on the calculated local currents, it would seem that any variations of surface current can only be recorded in areas of good imaging resolution, away from any field spikes. With our data, this can be more easily achieved with the higher temperature current profiles where field penetration covered a significant part of the sample surface. By closely examining the higher temperature profiles, including the one displayed in Fig.(5.16), it can be concluded that there was a noticeable lack of any significant current variation with local field strength. This result is in contrast to the results found from a similar experiment performed on YBaCuO disks[24]. In that experiment, current in the flux penetrated part of a disk was found to diminish in areas where greater field penetration occurred, around the inside edge of the sample. The samples in that case, however, were cooled down to 4.2K while very strong magnetic fields were applied with increasing strengths up 1760 Gauss. This is in contrast to our experiment where the sample was cooled no lower than liquid nitrogen temperatures and because of this only a relatively weak field of 10 Gauss was needed to achieve significant penetration. It could be due to the low fields used in the present work that no variation of surface current in response to local field strength was observed. To determine if this was the case a stronger magnetic field was applied to the sample while it was held at a temperature low enough to prevent complete penetration. A 75Gauss field was found to produce an adequate degree of radial penetration while the sample was held at 76K. In doing this any problems caused by imaging edge data spikes were also effectively avoided
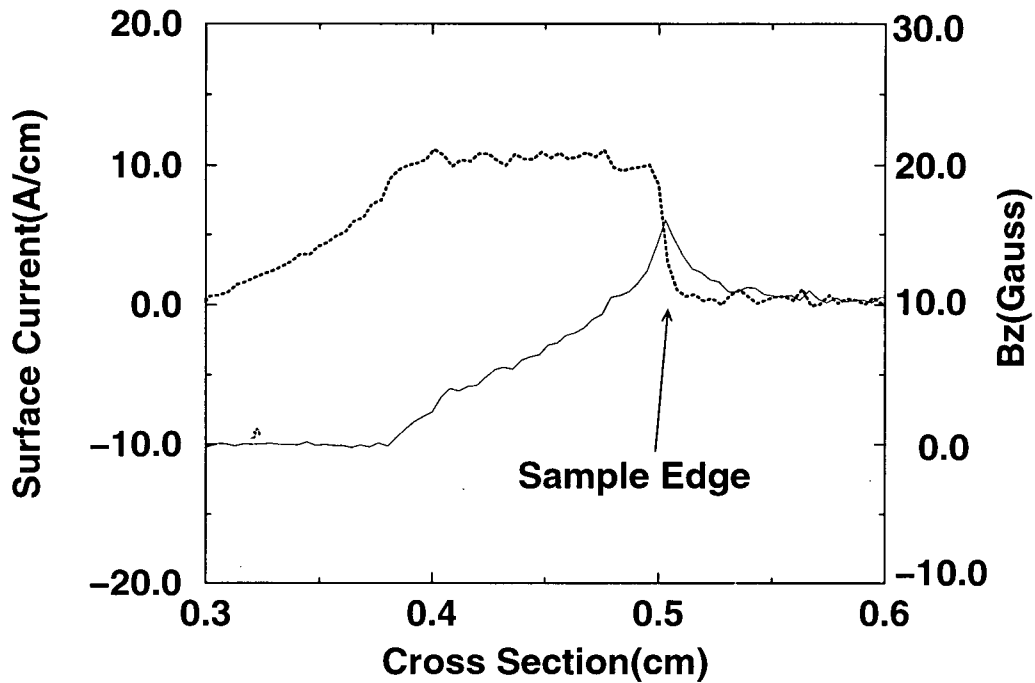
Figure 5.16: A Comparison of local surface current, dotted line, with local Bz-field, solid line, indicating a lack of a significant current-field dependence at a sample temperature of 92K using an applied field of 10Gauss.

since most of the profile data could be captured away from the edge. The result is displayed in Fig.(5.17) where a current-field dependence is immediately apparent. The solid line in that figure indicates the local surface current strength while the dotted line represents the local Bz-field. A distinct feature of the data in Fig.(5.17) was the tendency of the local current to increase as the local Bz-field decreased, in contradiction of Bean's model.
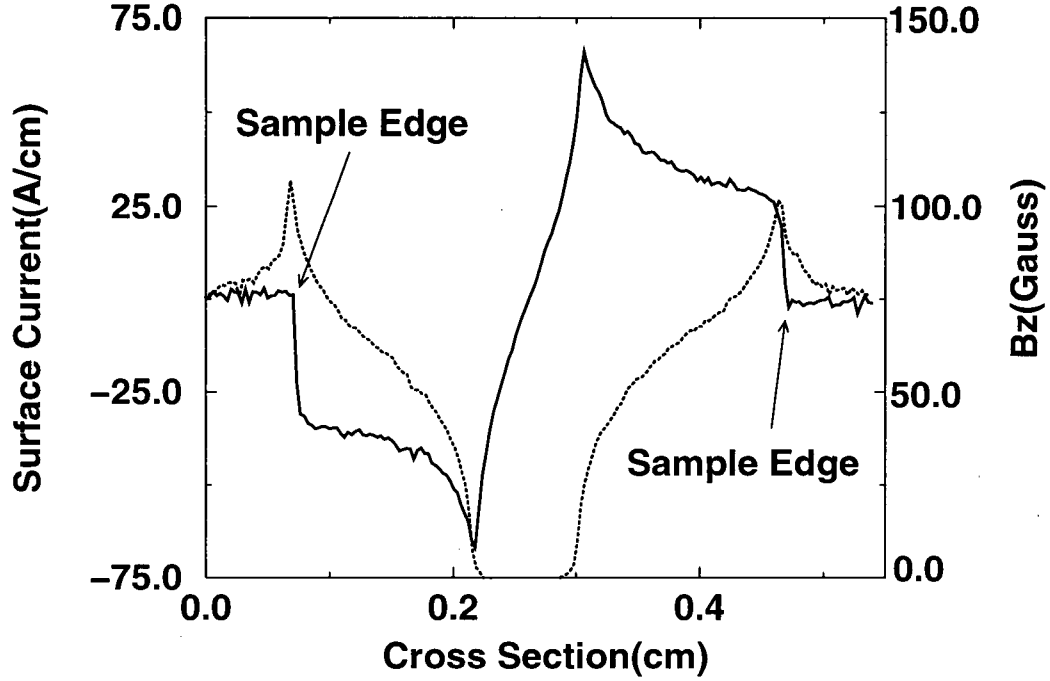
Figure 5.17: A Comparison of local surface current, solid line, with local Bz-field, dotted line, indicating a current-field dependence at a sample temperature of 76K with an applied field of 75Gauss.

5.7.1 Current-Field Dependence

The dependence of the critical current in a superconductor on local field strength has been addressed by Kim et al.[35] who first proposed a field dependent critical state model. In this model the critical current density can be written as:

$$J_c(T, B_z) = \frac{J_c(T)}{1 + B_z/H_0(T)} \tag{5.5}$$

where $J_c(T, B_z)$ indicates that the current is both temperature and field dependent, and where B_z is the local field strength, $J_c(T)$ is the critical current in zero field, and $H_0(T)$ is a variable having the units of Gauss. The variable $H_0(T)$ is dependent on the material pinning as is the critical current density and can vary even within the same material from the different pinning features of individual samples. In contrast,

93

Bean's model is represented by:

$$J_c(T, B_z) = J_c(T) \qquad (5.6)$$

indicating the absence of any current-field dependence. A more general form of Kim's model has also been devised by Xu et al.[36] where:

$$J_c(T, B_z) = \frac{J_c(T)}{(1 + B_z/H_0(T))^\beta} \qquad (5.7)$$

and where β is a dimensionless constant. The derivation of this last equation was motivated by the need to find a unified form of the critical state relation for all superconductors, including the high-Tc ceramics. With such a relation it is then possible to characterize superconductors by the parameters β and $H_0(T)$ expressed in Eq.(5.7). In the simplest case, Eq.(5.7) can represent either Bean's and Kim's models by simply setting the parameter β to either 0 or 1, respectively. Various other seemingly independent models used in the characterization of a field-current dependence where also found by Xu et al. to be fundamentally related through Eq.(5.7)[36]. This fact was established by applying various conditions where $B_z/H_0(T) \gg 1$ or $B_z/H_0(T) \ll 1$ or where $\beta \gg 1$. One model first used by Fietz et al.[37] describes the current-field dependence in a superconductor employing an exponential formula where:

$$J_c(T, B_z) = J_c(T) \exp(-B_z/\mathcal{H}) \qquad (5.8)$$

This equation may be derived from Eq.(5.7) for the case where $B_z/H_0(T) \ll 1$ and $\beta \gg 1$ where $H_0/\beta = \mathcal{H}$ and $\mathcal{H}$ is expressed in field units and has a finite value.

Both the local surface current in the penetrated region of the thin film and local field strength displayed in Fig.(5.17) were separately sampled and combined into a single graph where a fit was performed using Kim's model and the exponential relation of Eq.(5.8). The result may be seen in Fig.(5.18). The critical current density was determined by assuming the current was uniform through the sample thickness which enabled calculation of J_c by dividing the sample sheet current Λ_c by
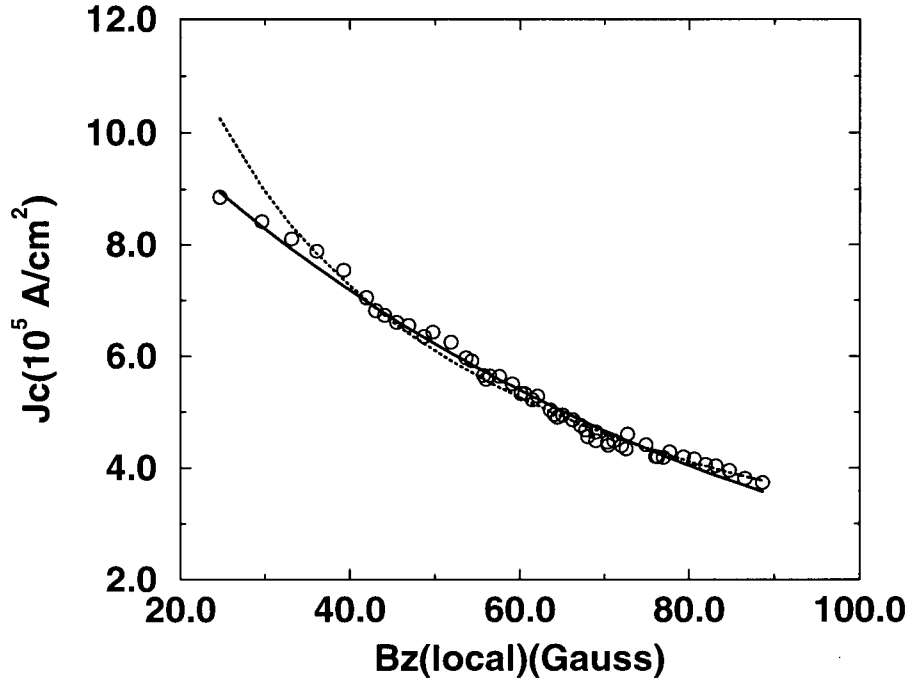
Figure 5.18: A fit of J_c versus local B_z using Eq.(5.5), dotted line and Eq.(5.8), solid line. The latter equation provides the best data fit while the first equation, commonly referred to as Kim's model, does not fit well at smaller local B_z values.

the sample thickness. In determining the best fit using this model it was established that $H_0(T) = 8.7\text{Gauss}$ for T=76K while $J_c(T) = 4.2 \times 10^6 \text{A/cm}^2$ in zero field. It can be seen from Fig.(5.18) that Kim's model, represented by the dotted line, tended to diverge away from the data at the lowest field values. Another problem with this model was related to the size of the zero-field critical current, which appeared to be excessive. By considering the trend in the zero-field critical current displayed in fig.(5.19) of the next section it is estimated that the critical current at 76K should be no larger than $J_c(T) = 2.0 \times 10^6 \text{A/cm}^2$. A more reasonable value was found by fitting the data in Fig.(5.18) with the empirical exponential model of Fietz et al.[37]. In using this model it was determined that $J_c(T) = 1.2 \times 10^6 \text{A/cm}^2$. In order to get the best possible fit it was also found that $\mathcal{H} = 70\text{Gauss}$. From Fig.(5.18) it can

be seen that the overall fit to the current-field data, using the empirical exponential model, tended to be better than the fit attempted with Kim's model.

5.7.2 Comparison of Iterated and Calculated Critical Currents
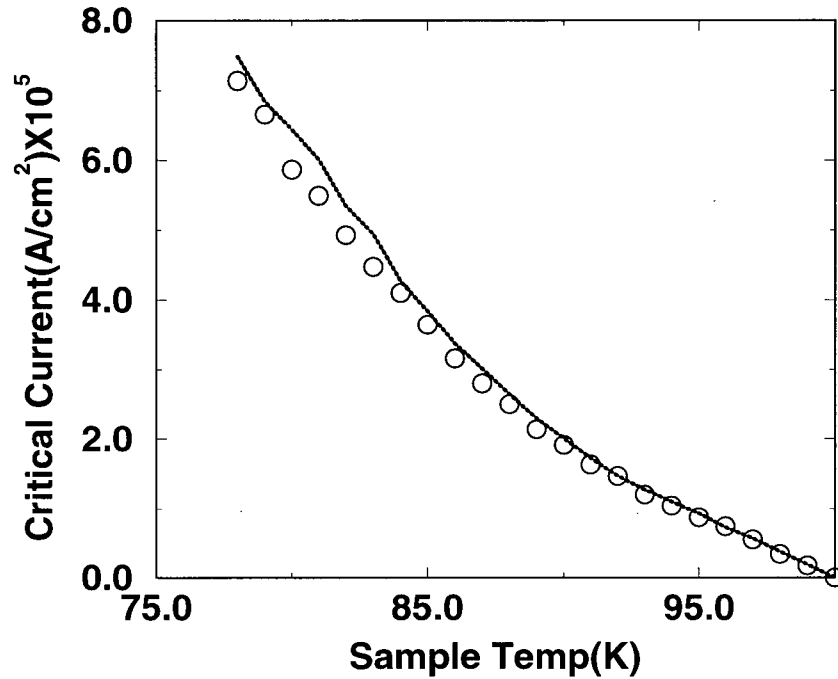
Figure 5.19: Temperature dependence of the sheet critical current for sample temperatures of 78K to 100K in 1K increments. The dotted line is the sheet current calculated using Eq.(5.1) and the measured radius of the Meissner region.

Using the augmented iteration to calculate local sheet currents it is also possible to observe the dependence of the critical current on sample temperature. By only sampling sheet currents near the inner Meissner region the data problems caused by field spikes near the sample edge were avoided. Since the local magnetic fields were lower in this region any field effects on the local current were also reduced. It can be seen in Fig.(5.19) from the experimental currents represented by open circles that the resulting critical current decreased non-linearly, from a maximum

at 78K of $7.1 \text{X} 10^5 \text{A/cm}^2$ down to zero at the sample's Tc of 100K. This behaviour was very closely matched by the currents calculated using Eq.(5.1) indicated by the dotted line in the same figure. The form of this curve was established by substituting the radius of the Meissner region from Fig.(5.8) into Eq.(5.1) and solving for H_c or equivalently the critical sheet current Λ_c. The critical current was then obtained by dividing the sheet current by the sample thickness. It is evident from Fig.(5.19) that the critical current could be adequately obtained by simply observing the degree of flux penetration in a circular thin film sample and applying Mikheenko's theory. By doing this the large amount of computation needed to determine the sheet current using the iterative method can be effectively avoided. This of course only applies to very uniform thin film samples that have no substantial defects. In addition to this, by using the iterative method no assumptions are made on the critical current dependence on local field strengths. As a result, any critical current field dependence will become evident on applying this technique to any measured field data.

An additional and rather important feature of the current temperature dependence of Fig.(5.19) is the presence of a slight kink in the data near 91K. Below this temperature the plotted data is curved upwards while above this temperature the data tended to have an almost linear dependence on temperature. This feature in the data is discussed further in the next section.

5.8 Critical Current Dependence on Temperature

Over the years a substantial amount of research has been conducted to determine the properties of high temperature superconducting thin films. One such property is the temperature dependence of the critical current in the superconducting state. Results have varied greatly, depending on the type of material used or on how the material was prepared. As a result many different models have been employed in an attempt to characterize the current temperature dependence with only limited success. One such model which has been found to hold at least close to the superconducting transition temperature utilizes a general phenomenological power law relation. This relation has the form $J(T) \propto (1 - T/T_c)^\alpha$ where in the past α has been measured to vary from 0.5 up to approximately 3. The thallium thin film critical current displayed in Fig.(5.19) can be examined more closely by attempting a data fit with this expression. In Fig(5.20) is displayed a log-log plot of $J(T)$ verses $(1 - T/T_c)$ used in the determination of the power law fit for the current temperature data. The slope of a linear fit in this figure corresponds to the size of the exponent in a power law equation. Due to the kink in the current temperature trend near 91K it was established that two separate fits were required to adequately represent all the data in the log-log plot of Fig(5.20). This result also implied that two power law relations with different exponents were needed to provide a complete fit to the data of Fig.(5.21). Similar behaviour has also been noted by Radovan et al. using a specially designed SQUID magnetometer to observe the critical current temperature dependence of a ring shaped thallium thin film superconductor[38]. In that investigation a distinct field-dependent critical current kink at 96.3K was observed in a sample having a Tc of 103.5K. At lower temperatures below the current data kink a quadratic power law was found to hold while above the kink a linear dependence best represented the critical current temperature trend. We have also observed similar tendencies in our critical current data. Below 91K a non-linear dependence was observed, where $\alpha = 1.74$ and $J(T) = 9.82 \times 10^5 \text{A/cm}^2 (1 -$
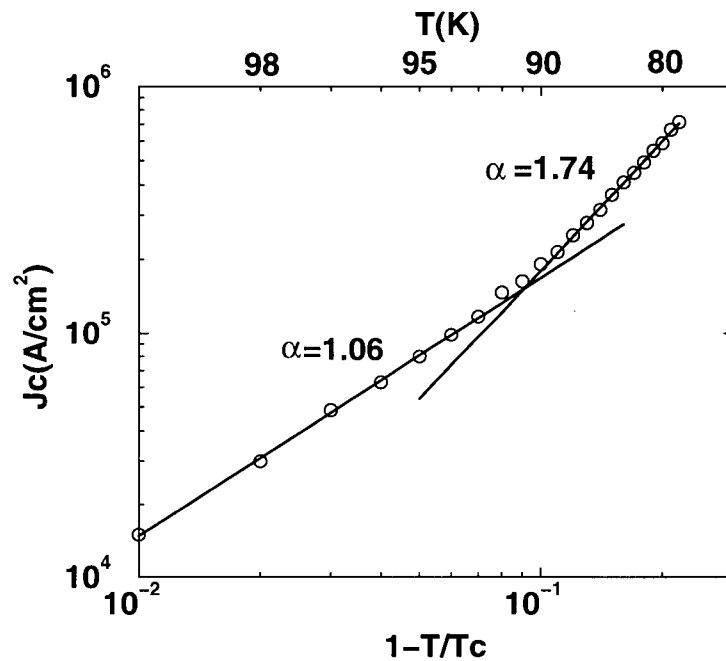
Figure 5.20: Log-log plot of critical current data from 78K to 100K. There was a sudden change in the exponent α of the standard power law equation $J(T) \propto (1 - T/T_c)^{\alpha}$.
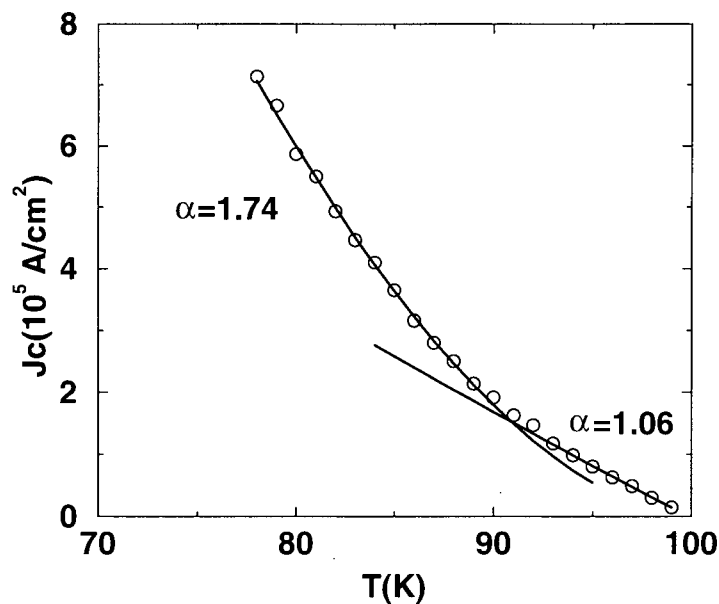
Figure 5.21: Current data from Fig.(5.19)was fitted to the relation $J(T) = 9.82 \times 10^5 \mathrm{A/cm^2}(1 - T/T_c)^{1.74}$ from 78K to 90K and fitted to $J(T) = 1.91 \times 10^6 \mathrm{A/cm^2}(1 - T/T_c)^{1.06}$ from 91K to 100K. Two different fits were required to accommodate the change in the critical current temperature dependence near 91K.

99

$T/T_c)^{1.74}$, while above this temperature the critical current was found to have an almost linear dependence on sample temperature, where $\alpha = 1.06$ and $J(T) = 1.91 \times 10^6 \text{A/cm}^2 (1 - T/T_c)^{1.06}$.

To better understand our data and the data of Radovan et al. consideration must be given to the anisotropic nature of the high temperature superconductors. This requires addressing the layered nature of the ceramic superconductors where currents are thought to flow along separate CuO_2 planes. Lawrence and Doniach[39] attempted to address this problem by introducing a model that approximates an anisotropic superconductor as a stack of weakly coupled superconducting layers. In each layer vortices acquire the form of magnetic pancakes and, depending on the degree of material anisotropy, are coupled to other vortices in adjacent layers. The amount of anisotropy can vary greatly depending on the type of material that comprises a superconductor. A useful quantity that describes this anisotropy is the dimensionless parameter γ where $\gamma = \xi_{ab}/\xi_c$ and where ξ_{ab} is the coherence length in the ab-plane and ξ_c is the coherence length along the c-axis[40]. It has been established that $YBa_2Cu_3O_y$ has an anisotropy parameter of $\gamma = 7.9$[41] while for $Tl_2Ba_2CaCu_2O_y$ it has been estimated to be $\gamma = 90$[33]. This strongly indicates that the latter material is a more anisotropic superconductor than the former material and as a result vortices tend to be less strongly coupled between the separate CuO_2 planes[42].

It has also been determined that the effective critical current density drops more rapidly with increasing temperature in more isotropic samples which is a result of the weaker coupling of pancake vortices between CuO_2 superconducting planes[43]. In this case weaker coupling between planes results in a greater tendency of vortices to be depinned by thermal effects, especially near the superconducting transition temperature where such effects are greatest. As a result, the size of the critical current in a very anisotropic material such as $Tl_2Ba_2CaCu_2O_y$ should drop considerably especially just below the superconducting transition temperature T_c.

This appeared not to be the case, however, with the present thin film sample nor with the sample investigated by Radovan et al. as was apparent from the onset of a linear current-temperature dependence near Tc in both cases. Radovan attempted to account for this anomaly by proposing a transition in the 2D characteristics of pancake vortices in highly anisotropic superconductors[38]. According to that author the observed current-temperature data kinks could reveal a point where there is a transition from single 2D vortex behaviour to a predominance of collective pancake vortex motion characterized by more sluggish dynamics at higher temperatures. This phenomenon, it was proposed, could correspond to a temperature dependent length scale of vortex interaction in the CuO_2 planes which grows with increasing sample temperature. Since individual vortex motion would tend to be suppressed by this interaction the dissipation of the critical current at higher temperatures would be less than that assuming a simple 2D creep of single pinned vortices. This would result in a smaller drop in the critical current which could account for the linear dependence observed near the superconducting transition temperature.

5.9 Conclusion

Using the magneto-optic technique it has been possible to observe flux penetration of a thallium-based circular thin film and to compare the results with a model of flux penetration developed by Mikheenko et al.[23] The results indicate that for a weak constant magnetic field the model holds up very well when describing Meissner expulsion of a sample. This applies to the distribution of field penetration of a circular sample as well as the corresponding current distribution. It was also observed that the critical current in the outer flux penetrated regions of the sample did not exhibit any significant field dependence in agreement with Bean's model when a very low applied field of 10Gauss was used to penetrate the sample. This was found

to change, however, with the application of a higher field of 75Gauss where an exponential dependence was observed to be present between the local critical current and local field strength. Applying the augmented iteration of chapter 3 and Mikheenko's model a change in current behaviour was observed with sample temperature. It was observed that below 91K the critical current exhibited a non-linear dependence with temperature while at higher temperatures current behaviour suddenly changed becoming more linear. This observation is in agreement with observations made by Radovan et al. of a similar superconductor material using a specially designed SQUID magnetometer[38]. It is thought that the change in current behaviour could be caused by a transition in the 2D characteristics of pancake vortices characterized by a crossover of individual vortex motion at lower temperatures to more collective behaviour at higher temperatures. This would result in more sluggish dynamics resulting in a less precipitous drop in the critical current and a more linear dependence on sample temperature just below the superconducting transition temperature, Tc.

Chapter 6

Conclusion

The dynamics associated with field penetration of single crystal and thin film superconductors were successfully studied using a specially designed magneto-optic apparatus that employed iron-garnet indicator films. The system has proven to be very flexible and efficient and is completely nondestructive to superconducting samples. The ability of iron-garnet films to remain active up to room temperature has enabled the observation of flux penetration dynamics at temperatures much higher than the temperatures reached by earlier magneto-optic systems[20].

The field penetration of two very high quality $YBa_2Cu_3O_{6.95}$ single crystals was observed and analyzed in the temperature range of 78K to 80K. A magnetic field of increasing strength which was used to penetrate the samples was applied perpendicular to the their surfaces, or equivalently along their c-axes. Evidence of a geometrical barrier effect was established to be present in both samples. The phenomenon is associated with a unique flux penetration pattern that is sensitive to the amount of pinning present in a thin flat superconducting sample. In one almost twin free ultra-low pinning sample flux was observed to accumulate in the central regions while avoiding the inside edges. Flux avoidance of the edges continued as the applied field was increased in strength and as the central flux accumulated region grew in size out from the sample's center. In another completely untwinned crystal that had slightly higher pinning characteristics penetrating fields tended to

initially avoid the central regions of the sample as well as the inside edges. Increasing the applied field caused regions of flux accumulation to grow in size towards the center and edges of the sample. This behaviour is consistent with a theoretical model devised by Zeldov et al.[21] that describes geometrical barrier effects on flux penetration in thin flat superconductors having moderate to no pinning. Cross sections taken of flux penetration of both samples tended to agree with predictions made by Zeldov's theory in terms of strength and position of the flux penetrated regions. This was the case even though the theory is modeled for an infinitely long strip superconductor while the samples under investigation tended to be square or slightly irregular. Since the flux penetration patterns predicted by Zeldov's model ultimately rely on the ratio of critical current density and edge current density, it was possible to adjust these values in the model until an optimum fit was found with experimental cross sections taken of flux penetration in the untwinned crystal. In doing this a quantitative ratio of these currents was established where it was determined that the edge current density was approximately 11 times greater than the crystal's critical current density. It was also established that a single twin boundary in one corner of the other ultra-low pinning sample acted as a barrier to transverse flux motion. Flux was observed to accumulate on one side of the boundary indicating the presence of a blocking action to flux motion. This result is found to be in agreement with previous studies[31] on twin boundaries. Another feature observed of the remnant flux state was the influence that the crystal geometry had on the overall distribution of remnant flux. It was found that the rectangular geometry of both crystals caused an X-like distribution of remnant flux with a central field maximum.

Flux penetration of a high quality circular thin film superconductor was also studied using the magneto-optic apparatus. The sample under investigation was comprised of $Tl_2Ba_2CaCu_2O_y$ which has been shown to have very anisotropic characteristics[33]. The uniformity of the sample was established by imaging it's

remnant field state and was found to be slightly asymmetrical. Penetration of the film was observed for increasing sample temperatures in a constant field applied perpendicular to the sample' surface. At the lowest temperature of 78K flux was almost completely expelled from the sample. As the sample temperature increased, penetrating fields tended to form an annular-like region that grew in size. The central flux expelled Meissner region also shrank accordingly. The degree and manner in which the field penetrated the film was found to agree very well with a field penetration model developed by Mikheenko et al.[23] for a circular thin film geometry. A special iterative inversion scheme was also developed and used to calculate local two dimensional currents from magneto-optically imaged penetrating fields in the circular thin film. This program was optimized and found to be almost 70 times faster than earlier inversion techniques while still providing the same degree of accuracy. Cross sections of the processed local current for different sample temperatures in the circular thin film were compared to the currents calculated with the flux penetration model developed by Mikheenko and found to be in good agreement. This was found to be especially true for the central Meissner region. Using a low field of 10Gauss to penetrate the sample any current field dependence was not observed in the outer flux penetrated annular region in agreement with Bean's critical state model which assumes an absence of any current-field dependence. This observation changed, however, when a stronger field of 75Gauss was applied to the circular thin film. In this case an exponential dependency was observed to be present between the local critical current and local magnetic B_z fields. By calculating the local currents using the iterative technique critical current values from the penetrated region were found for various sample temperatures, from 78K up to and including 100K, the sample's superconducting transition temperature. It was determined that the critical current fell from a maximum at 78K of 7.1×10^5A/cm down to zero at 100K. A small discontinuity in the current-temperature trend was also noted around 91K where above this temperature the critical current was almost linear with sample temperature. A

phenomenological power law model was employed to characterize the data requiring two separate data fits. Below 91K a non-linear dependence of current with sample temperature was observed where $J(T) = 9.82 \times 10^5 \text{A/cm}^2 (1 - T/T_c)^{1.74}$. Above this temperature it was determined that an almost linear power law relation best described the data where $J(T) = 1.91 \times 10^6 \text{A/cm}^2 (1 - T/T_c)^{1.06}$. The data discontinuity prevented the fitting of all the data to a single model or equation. The data trend above 91K implies that the critical current was more persistent and a little stronger than expected. This result may be a consequence of the very anisotropic nature of $Tl_2Ba_2CaCu_2O_y$ where, it is proposed, there may be a transition in the pancake vortex dynamics around 91K. Below this temperature current dynamics are thought to be dominated by the individual creep of single pinned vortices while at higher temperatures the dynamics could be affected by a transition to more collective vortex behaviour[38]. In the latter case greater vortex interaction would translate into a more sluggish dynamics and a less precipitous drop in the critical current near Tc.

Appendix A

Real time imaging program V_MON.C
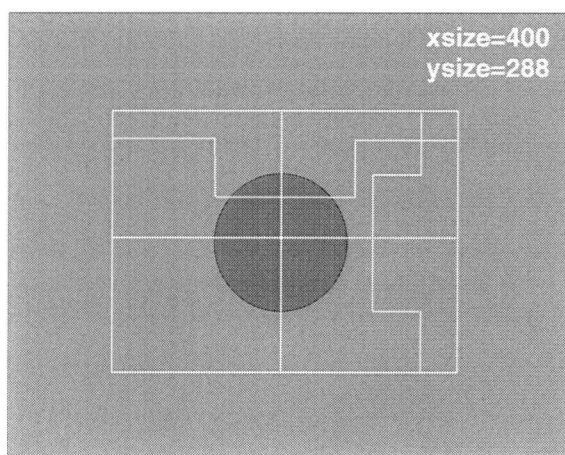
Figure A.1: Simulated display of the V_MON.C program format. The rectangular box outlines the imaging area and is used by other programs and defined by the user.

This program provides real time imaging of a sample at approximately 10 frames per second, provides light intensity profiles and stores parameters for a user defined image area in a file called "param" for use by other programs. The format of the running program is displayed in Fig.(A.1) where the rectangular outlined region can be adjusted by the user and defines the area of interest. Intensity profiles taken along the central x-y lines inside the imaging area are also included and are used to monitor the uniformity of illumination. The central dark circle of Fig.(A.1) demonstrates the profile response for simple object. Imaging size is also included in

the upper right corner of the screen. To move the upper edge of the box use ↑ ↓ and
to move the right edge use ← →. Adjusting the lower edge requires (ctrl ↑) (ctrl ↓)
and for the left edge (crtl ←) (crtl →). Parameters are stored in the file "param"
with (shift s) and include the upper left corner position of the imaging box and its
size, in numbers of pixles.

A.1 Program V_MON.C

```c
#include <stdio.h>
#include <stdlib.h >
#include <math.h>
#include <string.h>
#include <conio.h>
#include <mil.h>

#define FILE_DEBUG
#define length 15

MIL_ID   MilApplication;
MIL_ID   MilSystem     ;
MIL_ID   MilDigitizer  ;
MIL_ID   MilDisplay    ;
MIL_ID   MilImage[2]   ;
MIL_ID   MilImageDisp  ;
MIL_ID   MilLut        ;

void GlobalAlloc(void);
void GlobalDealloc(void);
```

```
// Main function.

void main(void)

{

 FILE *infile,*outfile;

 int   grabbuf=0,procbuf=1,incre=4,centrex,centrey,
               xsize,ysize,i=0,j;

 char c1,c2,param1[length],param2[length];

 unsigned char line1[640],line2[480];


 c1=c2=0;

 infile=fopen("param","r");

 fscanf(infile,"%*s %d %*s %d %*s %d %*s %d",
                     &xsize,&ysize,&centrex,&centrey);

 fclose(infile);

 GlobalAlloc();

 MdigReference(MilDigitizer,M_BRIGHTNESS_REF,135);

 MdispSelect(MilDisplay, MilImageDisp);

 // Do a first grab in the first buffer.

 MdigGrab(MilDigitizer, MilImage[grabbuf]);

 // Put digitizer in asynchronous grab mode.

 MdigControl(MilDigitizer, M_GRAB_MODE, M_ASYNCHRONOUS);

 // Process one buffer while grabbing the other.

  while(c1!=27){

while(!kbhit()){

// Grab second buffer during first buffer processing.

 if (grabbuf == 0) {

  grabbuf = 1;

  procbuf = 0;
```

```
} else {
 grabbuf = 0;
 procbuf = 1;
}
MdigGrab(MilDigitizer, MilImage[grabbuf]);
//MbufGet2d(MilImage[procbuf],10,(int) ypos,630,1,lttest);
MbufGet2d(MilImage[procbuf],1,centrey+(int)(ysize/2),638,1,line1);
MbufGet2d(MilImage[procbuf],centrex+xsize/2,1,1,478,
          line2);
MgraRect(M_DEFAULT,MilImage[procbuf],centrex,
centrey,centrex+xsize,centrey+ysize);
MgraLine(M_DEFAULT,MilImage[procbuf],centrex,centrey+ysize/2,
centrex+xsize,centrey+ysize/2);
MgraLine(M_DEFAULT,MilImage[procbuf],centrex+xsize/2,centrey,
centrex+xsize/2,centrey+ysize);
        for(j=2;j<=xsize;j+=2)
          MgraLine(M_DEFAULT,MilImage[procbuf],centrex+j-2,
            centrey+ysize/2-(long)(line1[j+centrex-2]/2),centrex+j,
            centrey+ysize/2-(long)(line1[j+centrex]/2));
        for(j=2;j<=ysize;j+=2)
  MgraLine(M_DEFAULT,MilImage[procbuf],
                centrex+xsize/2+(long)(line2[centrey+j-2]/2),
                centrey+j-2,centrex+xsize/2+(long)(line2[centrey+j]/2),
centrey+j);
sprintf(param1,"xsize=%d",xsize);
sprintf(param2,"ysize=%d",ysize);
MgraText(M_DEFAULT,MilImage[procbuf],500,5,param1);
MgraText(M_DEFAULT,MilImage[procbuf],500,25,param2);
```

```
if(c1==83){

  MgraText(M_DEFAULT,MilImage[procbuf],

350,450,"Saved parameters to param file");

  if(i==0){

outfile=fopen("param","w");

fprintf(outfile,"xsize %d\n",xsize);

fprintf(outfile,"ysize %d\n",ysize);

fprintf(outfile,"centrex %d\n",centrex);

fprintf(outfile,"centrey %d\n",centrey);

fclose(outfile);

++i;

    }

}

// Perform the a copy of the first buffer already grabbed.

// Note: Generally real time on fast PC.

MbufCopy(MilImage[procbuf], MilImageDisp);

  }

  c1=getch();

  if(c1==0){

c2=getch();

  switch(c2){

                          case 72:{

                          centrey-=incre;

ysize+=incre;

                          }

        break;

                          case 80:{

                          centrey+=incre;
```

```
                            ysize-=incre;
}

          break;
          case -115:
ysize-=incre;
 break;
 case -111:
ysize+=incre;
 break;
 case 77:
xsize+=incre;
 break;
 case 75:
xsize-=incre;
 break;
case 116:{

                              centrex+=incre;
                              xsize-=incre;

}
 break;
case 115:{

                              centrex-=incre;
                              xsize+=incre;

}
          break;
}
  }
  switch(c1){
```

```
case 117:

  centrey-=incre;

break;

case 100:

  centrey+=incre;

break;

case 114:

  centrex+=incre;

break;

case 108:

  centrex-=incre;

break;

  }

  switch(c1){

case 105:

 ++incre;

break;

        case 9:{

          if(incre>1)

            --incre;

        }

break;

  }

}

// Wait last grab end.

MdigGrabWait(MilDigitizer, M_GRAB_END);

MdispDeselect(MilDisplay, MilImageDisp);

GlobalDealloc();
```

```
}


void GlobalAlloc(void)
{
   MappAlloc(M_DEFAULT, &MilApplication);

   MsysAlloc(M_DEF_SYSTEM_TYPE, M_DEFAULT, M_DEFAULT, &MilSystem);

   MdigAlloc(MilSystem, M_DEFAULT, M_DEF_DIGITIZER_FORMAT,
        M_DEFAULT, &MilDigitizer);

   MdispAlloc(MilSystem, M_DEFAULT,M_DISPLAY_SETUP,

                                           M_DEFAULT, &MilDisplay);


// Allocate 2 grab buffers.

MbufAlloc2d(MilSystem,

MdigInquire(MilDigitizer, M_SIZE_X, M_NULL),

                     MdigInquire(MilDigitizer, M_SIZE_Y, M_NULL),

8L+M_UNSIGNED,

M_IMAGE+M_GRAB+M_PROC, &MilImage[0]);

MbufAlloc2d(MilSystem, MdigInquire(MilDigitizer, M_SIZE_X, M_NULL),

     MdigInquire(MilDigitizer, M_SIZE_Y, M_NULL),

8L+M_UNSIGNED,

M_IMAGE+M_GRAB+M_PROC, &MilImage[1]);


// Allocate 1 display buffer and clear it.

MbufAlloc2d(MilSystem, MdigInquire(MilDigitizer, M_SIZE_X, M_NULL),

MdigInquire(MilDigitizer, M_SIZE_Y, M_NULL),

8L+M_UNSIGNED,

M_IMAGE+M_GRAB+M_PROC+M_DISP, &MilImageDisp);
```

```
MbufClear(MilImageDisp, 0x0);


}


void GlobalDealloc(void)
{
    MbufFree(MilImageDisp);
    MbufFree(MilImage[0]);
    MbufFree(MilImage[1]);
    MdispFree(MilDisplay);
    MdigFree(MilDigitizer);
    MsysFree(MilSystem);
    MappFree(MilApplication);
}
```

Appendix B

Linerization Program LIN.C
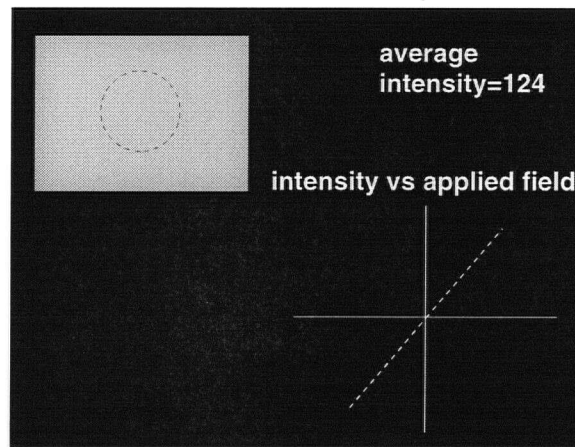
Figure B.1: Simulated display of the LIN.C program format. The imaged area is displayed in the upper left corner of the screen and it's intensity measured while the sample is not superconducting. This program is used to determine the response of the garnet film to known applied fields.

This program finds the average illuminated intensity of a pre-defined area supplied by the user from the program V_MON.C. The imaged area is displayed in the upper left corner of the screen and the average intensity can be found in the upper right corner. The maximum intensity displayed is 255 corresponding to the 256 greyscale imaging provided by the CCD camera. The user has the option of applying a scaled applied magnetic field to the garnet film where the average intensity response is plotted on the lower right screen quadrant. Axes for the plotted

graph are displayed by keying d and plotting commences by typing s. The results may be cleared by typing c. The maximum intensity of the applied field along with the field increments and its duration are entered by the user as parameters in a file called "lin.par". On typing s, the applied field is cycled once up to the maximum intensity by the defined increments, then down to the same maximum intensity with opposite polarization and then back up to zero ending the cycle. The resulting plotted average intensity determines the linear response of the garnet film. This process may be repeated as many times as necessary until the optimum response is achieved.

B.1 Program LIN.C

```c
#include <stdio.h>
#include <stdlib.h>
#include <math.h>
#include <string.h>
#include <conio.h>
#include <mil.h>
#include <bios.h>
#include <dos.h>

#define CMD 0
#define FILE_DEBUG
#define length 25
#define IMAGE_DEPTH 8L

MIL_ID    MilApplication;
MIL_ID    MilSystem;
MIL_ID    MilDigitizer;
```

```c
MIL_ID    MilDisplay;

MIL_ID    MilImage[2];

MIL_ID    MilImage1;

MIL_ID    MilImage2;

MIL_ID    MilParentImage;

MIL_ID    MilImageDisp;

MIL_ID    MilImageDisp2;

MIL_ID    MilImageDisp3;


void      GlobalAlloc(void);

void      GlobalDealloc(void);

void       imdis(void);

void      dely(float);

void      fieldapp(float);

int        grabbuf=0,procbuf=1,xcolumns,yrows,centrex,
            centrey,i,average=0,tog=0,tog2=0,average1=0,
            pas=0,delay0,delay1,data,H_byte,L_byte,Port;

float     maxfield,fieldjump,incre=0.0,incre1=0.0,maxin,field=0.0,
            th0,th1,fcal;

long      t1,t2;

char      c1,param1[length];

unsigned    char *area;

double       d;


main()
{
 FILE *infile1,*infile2;
 infile1=fopen("param","r");
```

```c
infile2=fopen("lin.par","r");
if(infile1==NULL){
 printf("Cannot open param file!\n");
 exit(1);
}
if(infile2==NULL){
 printf("Cannot open lin.par file!\n");
 exit(1);
}
fscanf(infile1,"%*s %d %*s %d %*s %d %*s %d",&xcolumns,&yrows,
&centrex,&centrey);
area=calloc(yrows*xcolumns,sizeof(unsigned char));
fclose(infile1);
fscanf(infile2,"%*s %g %*s %g %*s %d %*s %d %*s %g",
            &maxfield,&fieldjump,&delay0,&delay1,&fcal);
fclose(infile2);
Port = 0x2C0;
th0=((float)delay0)/((float)1000);
th1=((float)delay1)/((float)1000);
incre=300/(maxfield/fieldjump);
maxin=((int)(maxfield/fieldjump))*incre;
c1=0;
GlobalAlloc();
MdigReference(MilDigitizer,M_BRIGHTNESS_REF,135);
MdigReference(MilDigitizer,M_CONTRAST_REF,255);
MdispSelect(MilDisplay, MilParentImage);
MdigGrab(MilDigitizer, MilImage[grabbuf]);
MdigControl(MilDigitizer, M_GRAB_MODE, M_ASYNCHRONOUS);
```

```
MgraFontScale(M_DEFAULT,2,2);

MbufClear(MilImage1,0);

MgraText(M_DEFAULT,MilImage1,125,125,"Intensity vs. Applied field");

MgraLine(M_DEFAULT,MilImage1,320,160,320,640);

MgraLine(M_DEFAULT,MilImage1,0,400,640,400);

while(c1!=27){

  while((!kbhit())&&(pas==0)){

      imdis();

      if((c1==115)&&(tog2==0)){

        average1=average;

        tog2=1;

      }

      if(c1==115){

        if(((int)(incre1))==((int)(maxin)))

          tog=1;

        if(((int)(incre1))==((int)(-maxin)))

          tog=0;

        if(tog==0){

          incre1+=incre;

          field+=fieldjump;

          if(((int)(incre1))==0)

            pas=1;

          fieldapp(field);

          dely(th0);

          dely(th1);

          imdis();

          imdis();

          MgraArcFill(M_DEFAULT,MilImage1,320+(int)incre1,
```

```
                400-2*(average-average1),1,1,0.0,360.0);
}

        if(tog==1){
            incre1-=incre;
            field-=fieldjump;
            fieldapp(field);
            dely(th0);
            dely(th1);
            imdis();
            imdis();
            MgraArcFill(M_DEFAULT,MilImage1,320+(int)incre1,400-2*
                    (average-average1),1,1,0.0,360.0);
         }
        MbufCopy(MilImage1, MilImageDisp2);
}
average=0;
}
data =2048;
H_byte = data/256;
L_byte = data-H_byte*256;
outportb(Port+0, H_byte);
outportb(Port+1, L_byte);
c1=getch();
tog2=0;
tog=0;
incre1=0;
pas=0;
field=0.0;
```

```
   if((c1==99)||(c1==100)){

        MbufClear(MilImage1,0);

        MgraText(M_DEFAULT,MilImage1,125,125,"Intensity

                         vs. Applied field");

        MgraLine(M_DEFAULT,MilImage1,320,160,320,640);

        MgraLine(M_DEFAULT,MilImage1,0,400,640,400);

        MbufCopy(MilImage1, MilImageDisp2);

        c1=0;

    }

}

data =2048;

H_byte = data/256;

L_byte = data-H_byte*256;

outportb(Port+0, H_byte);

outportb(Port+1, L_byte);

// Wait last grab end.

MdigGrabWait(MilDigitizer, M_GRAB_END);

MdispDeselect(MilDisplay, MilParentImage);

GlobalDealloc();

free(area);

return 0;

}



void GlobalAlloc(void)

{


 MappAlloc(M_DEFAULT, &MilApplication);
```

```
      MsysAlloc(M_DEF_SYSTEM_TYPE, M_DEFAULT,
                        M_DEFAULT, &MilSystem);
      MdigAlloc(MilSystem, M_DEFAULT, M_DEF_DIGITIZER_FORMAT,
                        M_DEFAULT, &MilDigitizer);
      MdispAlloc(MilSystem, M_DEFAULT,"1280x1024x8pp",
                        M_DEFAULT, &MilDisplay);
// Allocate 2 grab buffers.
      MbufAlloc2d(MilSystem,1280,1024,
        IMAGE_DEPTH+M_UNSIGNED, M_IMAGE+

                                        M_DISP+M_PROC, &MilParentImage);
      MbufAlloc2d(MilSystem,640,480,IMAGE_DEPTH+M_UNSIGNED,
        M_IMAGE+M_GRAB+M_PROC,&MilImage[0]);
      MbufAlloc2d(MilSystem,640,480,IMAGE_DEPTH+M_UNSIGNED,
M_IMAGE+M_GRAB+M_PROC,&MilImage[1]);
      MbufAlloc2d(MilSystem,640,640,IMAGE_DEPTH+M_UNSIGNED,
        M_IMAGE+M_PROC,&MilImage1);
      MbufAlloc2d(MilSystem,640,480,IMAGE_DEPTH+M_UNSIGNED,
        M_IMAGE+M_PROC,&MilImage2)
        // Allocate 1 display buffer and clear it.
      MbufChild2d(MilParentImage,0,0,640,480,&MilImageDisp);
      MbufChild2d(MilParentImage,640,380,640,640,&MilImageDisp2);
      MbufChild2d(MilParentImage,740,200,335,30,&MilImageDisp3);
      MbufClear(MilImageDisp, 0x0);
      MbufClear(MilImageDisp2, 0x0);
      MbufClear(MilImageDisp3, 0x0);



}
```

```c
void GlobalDealloc(void)

{

MbufFree(MilImageDisp);

MbufFree(MilImageDisp2);

MbufFree(MilImageDisp3);

MbufFree(MilImage[0]);

MbufFree(MilImage[1]);

MbufFree(MilImage1);

MbufFree(MilImage2);

MbufFree(MilParentImage);

MdispFree(MilDisplay);

MdigFree(MilDigitizer);

MsysFree(MilSystem);

MappFree(MilApplication);

}

void imdis(void)

{

 if (grabbuf == 0){

  grabbuf = 1;

  procbuf = 0;

 } else {

  grabbuf = 0;

  procbuf = 1;

 }

 MdigGrab(MilDigitizer, MilImage[grabbuf]);

 MbufGet2d(MilImage[procbuf],centrex,centrey,xcolumns,yrows,area);

 for(i=0;i<(xcolumns*yrows);++i)
```

```c
  average+=(int)(area[i]);
 average=(int)(average/(xcolumns*yrows));
 MgraRect(M_DEFAULT,MilImage[procbuf],centrex,centrey,
                   xcolumns+centrex, yrows+centrey);
 sprintf(param1,"Average Intensity=%3d",average);
 MgraText(M_DEFAULT,MilImage2,0,0,param1);
 MbufCopy(MilImage[procbuf], MilImageDisp);
 MbufCopy(MilImage2, MilImageDisp3);
}
void fieldapp(float hh)
{
  data = (hh/fcal*2048)+2048;
  H_byte = data/256;
  L_byte = data-H_byte*256;
  outportb(Port+0, H_byte);
  outportb(Port+1, L_byte);
}
void dely(float tt)
{
 t1=biostime(CMD,0);
 t2=biostime(CMD,0);
 while((t2-t1)<=(tt*18.2))
  t2=biostime(CMD,0);
}
```

Appendix C

Calibration Program REFF.C

This program is used primarily in the calibration process described in chapter 2 and is controlled by a parameter file called reff.par. This file contains several parameters which include the strength of an applied field, in units of Guass, and its duration, in units of millseconds. The field is applied in alternating directions at the inputted strengths to the garnet film and the film's average intensity responses recorded with a user defined number of image frames and loops. This intensity response is then used to calculate an average intensity versus field strength parameter and stored in a separate file for use by the SUBF.C, outlined in the appendix D. Another parameter includes a digital contrast control which runs from 0-255, with 255 being the maximum contrast provided by the system. This parameter, as mentioned in chapter 2, is useful when imaging weak dynamics which can be overwhelmed by the response of small inperfections from the garnet film. Also included is a calibration factor for the Helmholtz coil which is used as a conversion factor by the program to correlate the applied field strength with the output supplied by the digital-to-analog board to the power supply. The user first has to raise the sample just above its transition temperature before initiating the program so that only the garnet film intensity responses are recorded. Also, a polarizer on the end of the microscope must be adjusted to get the most linear response from the garnet film.

C.1 Program REFF.C

```c
#include <stdio.h>

#include <stdlib.h>

#include <math.h>

#include <conio.h>

#include <string.h>

#include <bios.h>

#include <dos.h>

#include <mil.h>


#define CMD 0
#define length 15


MIL_ID              MilApplication;

MIL_ID              MilSystem;

MIL_ID              MilDisplay;

MIL_ID              MilImageDisp;

MIL_ID              MilImage;

MIL_ID              MilImage2;

MIL_ID              MilImage3[2];

MIL_ID              MilDigitizer;


void      GlobalAlloc(void);

void      GlobalDealloc(void);

void      fieldapp(float,float);

void      imdis(float,float,float);

void      divide(void);

void      aloc(void);
```

```
void        daloc(void);

void        maxmin(double *,double *,double *);

FILE        *infile1,*infile2,*outfile,*outfile2;

float       h0,h1,fcal,th0,th1,zero,pslope,nslope,paverg;

int         grabbuf=0,procbuf=1,rows,columns,centrex,centrey,
            delay0,delay1,frames,i,j,k,loops,data,H_byte,
            L_byte,Port,cont;

double  *aver,*posaverf,*negaverf,posavf,negavf,zro;

unsigned char    *Image,*Image2,*norm;

long                 *maxaver,*minaver,*dv,t1,t2;

char                 param1[length],param2[length],param3[length];


main()
{

 infile1=fopen("param","r");
 if(infile1==NULL){
  printf("Cannot open param file!\n");
  exit(1);
 }
 fscanf(infile1,"%*s %d %*s %d %*s %d %*s %d",&columns,&rows,
 &centrex,&centrey);
 fclose(infile1);
 infile2=fopen("ref.par","r");
 if(infile2==NULL){
  printf("Cannot open ref.par file!\n");
  exit(1);
 }
```

```
fscanf(infile2,"%*s %g %*s %d %*s %g %*s %d %*s %g
                %*s %d %*s %d %*s %d",
           &h0,&delay0,&h1,&delay1,&fcal,&frames,&loops,&cont);
fclose(infile2);
Port = 0x2C0;
th0=((float)delay0)/((float)1000);
th1=((float)delay1)/((float)1000);
aloc();
GlobalAlloc();
MdigReference(MilDigitizer,M_BRIGHTNESS_REF,135);
MdigReference(MilDigitizer,M_CONTRAST_REF,cont);
MdigControl(MilDigitizer,M_GRAB_MODE,M_ASYNCHRONOUS);
MdispSelect(MilDisplay,MilImageDisp);
delay(1000);
divide();
getch();
for(i=frames;i>0;--i){
  fieldapp(h0,h1);
  for(k=0;k<loops;++k){
   MdigGrab(MilDigitizer,MilImage);
   MdigGrab(MilDigitizer,MilImage);
   MdigGrabWait(MilDigitizer,M_GRAB_END);
   MbufCopy(MilImage,MilImageDisp);
   MgraArcFill(M_DEFAULT,MilImageDisp,575,25,5,5,0.0,360.0);
   MbufGet2d(MilImage,centrex,centrey,columns,rows,Image);
   for(j=0;j<(rows*columns);++j)
        maxaver[j]+=(long)(Image[j]);
 }
```

```
   fieldapp(-h0,-h1);
   for(k=0;k<loops;++k){
     MdigGrab(MilDigitizer,MilImage);
     MdigGrab(MilDigitizer,MilImage);
     MdigGrabWait(MilDigitizer,M_GRAB_END);
     MbufCopy(MilImage,MilImageDisp);
     MgraArcFill(M_DEFAULT,MilImageDisp,575,25,5,5,0.0,360.0);
     MbufGet2d(MilImage,centrex,centrey,columns,rows,Image);
     for(j=0;j<(rows*columns);++j)
       minaver[j]+=(long)(Image[j]);
   }
   if(kbhit())
if(getch()==27)
 i=0;
 }
 data =2048;
 H_byte = data/256;
 L_byte = data-H_byte*256;
 outportb(Port+0, H_byte);
 outportb(Port+1, L_byte);
 for(j=0;j<(rows*columns);++j){
   posaverf[j]=((double)maxaver[j])/((double)dv[j])*zro;
   negaverf[j]=((double)minaver[j])/((double)dv[j])*zro;
   posavf+=posaverf[j]/((double)(rows*columns));
   negavf+=negaverf[j]/((double)(rows*columns));
 }
 pslope=(posavf-zro)/h0;
 nslope=(zro-negavf)/h1;
```

```c
for(j=0;j<(rows*columns);++j)

    norm[j]=(unsigned char)(posaverf[j]);

MbufClear(MilImageDisp,0);

MbufPut2d(MilImageDisp,0,0,columns,rows,norm);

getch();

MbufAlloc2d(MilSystem,columns,rows,8L+M_UNSIGNED,
                         M_IMAGE+M_DISP,&MilImage2);

MbufCopyClip(MilImageDisp,MilImage2,0,0);

MbufExport("av",M_TIFF,MilImage2);

MbufClear(MilImageDisp,0);

daloc();

MbufFree(MilImage2);

MdispDeselect(MilDisplay,MilImageDisp);

GlobalDealloc();

outfile=fopen("history","a");

fprintf(outfile,
  "ref(%d,%d),h0=%g h1=%g,posi=%g negi=%g,av. zero=%lg\n",

frames,loops,h0,h1,pslope,nslope,zro);

fclose(outfile);

paverg=pslope+nslope;

outfile2=fopen("commd","w");

fprintf(outfile2,"%g\n",paverg);

fclose(outfile2);

return 0;

}

void GlobalAlloc(void)

{

MappAlloc(M_DEFAULT,&MilApplication);
```

```
MsysAlloc(M_DEF_SYSTEM_TYPE,M_DEFAULT,
                M_DEFAULT,&MilSystem);

MdigAlloc(MilSystem,M_DEFAULT,M_DEF_DIGITIZER_FORMAT,
                M_DEFAULT,&MilDigitizer);

MdispAlloc(MilSystem,M_DEFAULT,M_DISPLAY_SETUP,
                M_DEFAULT,&MilDisplay);

MbufAlloc2d(MilSystem,MdigInquire(MilDigitizer,M_SIZE_X,M_NULL),
    MdigInquire(MilDigitizer,M_SIZE_Y,M_NULL),
    8L+M_UNSIGNED,M_IMAGE+M_GRAB+M_PROC,&MilImage);

MbufAlloc2d(MilSystem,
  MdigInquire(MilDigitizer, M_SIZE_X, M_NULL),
  MdigInquire(MilDigitizer, M_SIZE_Y, M_NULL),
    8L+M_UNSIGNED,
  M_IMAGE+M_GRAB+M_PROC, &MilImage3[0]);

MbufAlloc2d(MilSystem,
  MdigInquire(MilDigitizer, M_SIZE_X, M_NULL),
  MdigInquire(MilDigitizer, M_SIZE_Y, M_NULL),
        8L+M_UNSIGNED,
  M_IMAGE+M_GRAB+M_PROC, &MilImage3[1]);

MbufAlloc2d(MilSystem,MdigInquire(MilDigitizer,M_SIZE_X,M_NULL),
  MdigInquire(MilDigitizer,M_SIZE_Y,M_NULL),
  8L+M_UNSIGNED,M_IMAGE+M_GRAB+M_PROC+M_DISP,
                &MilImageDisp);

}
void GlobalDealloc(void)
{
MbufFree(MilImageDisp);
```

```
 MbufFree(MilImage);

 MbufFree(MilImage3[0]);

 MbufFree(MilImage3[1]);

 MdispFree(MilDisplay);

 MdigFree(MilDigitizer);

 MsysFree(MilSystem);

 MappFree(MilApplication);

}

void fieldapp(float hh0,float hh1)

{

 data = (hh0/fcal*2048)+2048;

 H_byte = data/256;

 L_byte = data-H_byte*256;

 outportb(Port+0, H_byte);

 outportb(Port+1, L_byte);

 imdis(hh0,hh1,th0);

 data = (hh1/fcal*2048)+2048;

 H_byte = data/256;

 L_byte = data-H_byte*256;

 outportb(Port+0, H_byte);

 outportb(Port+1, L_byte);

 imdis(hh0,hh1,th1);

}

void imdis(float hh0,float hh1,float tt)

{

 t1=biostime(CMD,0);

 t2=biostime(CMD,0);

 MdigGrab(MilDigitizer, MilImage3[grabbuf]);
```

```c
while((t2-t1)<=(tt*18.2)){
  if (grabbuf == 0) {
    grabbuf = 1;
    procbuf = 0;
  } else {
    grabbuf = 0;
    procbuf = 1;
  }
  MdigGrab(MilDigitizer, MilImage3[grabbuf]);
if(hh0>0){
  sprintf(param1,"h0=+%g",hh0);
  sprintf(param2,"h1=+%g",hh1);
  sprintf(param3,"frame=%d",i);}
else{
  sprintf(param1,"h0=%g",hh0);
  sprintf(param2,"h1=%g",hh1);}
MgraText(M_DEFAULT,MilImage3[procbuf],550,5,param1);
MgraText(M_DEFAULT,MilImage3[procbuf],550,20,param2);
MgraText(M_DEFAULT,MilImage3[procbuf],550,35,param3);
MbufCopy(MilImage3[procbuf], MilImageDisp);
t2=biostime(CMD,0);
}
MdigGrabWait(MilDigitizer,M_GRAB_END);
}
void divide(void)
{
for(i=(frames);i>0;--i){
  for(k=0;k<(loops);++k){
```

```c
        MdigGrab(MilDigitizer,MilImage);

        MdigGrab(MilDigitizer,MilImage);

        MdigGrabWait(MilDigitizer,M_GRAB_END);

        MbufCopy(MilImage,MilImageDisp);

        sprintf(param3,"frame=%d",i);

        MgraText(M_DEFAULT,MilImageDisp,550,35,param3);

        MbufGet2d(MilImage,centrex,centrey,columns,rows,Image2);

        for(j=0;j<(rows*columns);++j)

            dv[j]+=(long)(Image2[j]);

  }

 }

 for(j=0;j<(rows*columns);++j)

   zro+=((double)dv[j])/((double)(rows*columns*frames*loops));


}

void aloc(void)

{

 Image=calloc(rows*columns,sizeof(unsigned char));

 Image2=calloc(rows*columns,sizeof(unsigned char));

 maxaver=calloc(rows*columns,sizeof(long));

 minaver=calloc(rows*columns,sizeof(long));

 posaverf=calloc(rows*columns,sizeof(double));

 negaverf=calloc(rows*columns,sizeof(double));

 dv=calloc(rows*columns,sizeof(long));

 norm=calloc(rows*columns,sizeof(unsigned char));

}

void daloc(void)

{
```

```
  free(Image);

  free(Image2);

  free(maxaver);

  free(minaver);

  free(posaverf);

  free(negaverf);

  free(dv);

  free(norm);

}
void maxmin(double *hold,double *maxim,double *minim)

{
 *maxim=*minim=hold[0];
 for(j=0;j<(rows*columns);++j){
   if(hold[j]>*maxim)
     *maxim=hold[j];
   if(hold[j]<=*minim)
     *minim=hold[j];
 }
}
```

Appendix D

Subtraction and Averaging Program SUBF.C

This program produces in-field or remnant field images using the subtraction and averaging alogrithm described in chapter 2. The program is controlled by a set of parameters in a file called subf.par. These values include the strength of the field in Guass applied using opposite polarities and their duration in units of milliseconds. Also included, as previously noted in chapter 2, is a digital contrast control parameter,which can be useful when imaging weak flux structures and parameters for the number of imaged frames and loops required. The inputted contrast parameter can range from 0-255 with 255 corresponding to the maximum contrast. An additional parameter is a calibration factor for the Helmholtz coil used to correlate the applied field strength with the digital-to-analog board. There is also a image division option, where an input of 1, indicating true, will direct the program to first take a series of averaged images of the illuminated intensity of the garnet film surface. To use this option properly, the user must first raise the sample above its superconducting transition temperature. The program will then wait after taking the intensity images until the user has cooled the sample to the required temperature before proceeding to the image subtraction process. As previously mentioned in chapter 2, image division is used to even out any unwanted light intensity variations. Inputting 0 will cause the program to skip this option producing an uncalibrated uneven subraction image used for quick examination of a sample. Calibration of an image is

performed by inputting 1 for the calibration option in the parameter file. In this case, the program will use the averaged calibration factor supplied by the program REFF.C to append four parameters at the end of a tiff file. Doing this does not affect the performance of other imaging packages such as XV or Adobe photshope which can also be used to display the tiff images. The parameters appended include those described in chaper 2 used for equation Eq.(2.1) in the VG.C program, see appendix E. The SUBF.C program, if instructed to produce a calibrated image, will first write #cali# at the end of the image file, then the four parameters. This is done so that the visualization program described in appendix E will know that the next four numbers are calibration factors to be used for displaying local fields from local intensity values. Finally, there is also a parameter called fout which runs on true or false, 1 or 0 and outputs on 1, a calibrated ascii file of field strengths.

D.1   Program SUBF.C

```
#include <stdio.h>
#include <stdlib.h>
#include <conio.h>
#include <string.h>
#include <math.h>
#include <dos.h>
#include <bios.h>
#include <mil.h>


#define CMD 0
#define length 15


MIL_ID              MilApplication;
MIL_ID              MilSystem;
```

```c
MIL_ID              MilDisplay;

MIL_ID              MilImageDisp;

MIL_ID              MilImage;

MIL_ID              MilImage2;

MIL_ID              MilImage3[2];

MIL_ID              MilDigitizer;


void    GlobalAlloc(void);

void    GlobalDealloc(void);

void    aloc(void);

void    daloc(void);

void    imdis(float,float,float);

void    divide(void);

void    maxmin(double *,double *,double *);

void    fieldapp(float,float);

FILE    *infile1,*infile2,*infile3,*outfile,*outfile2,*outfile3;

int     grabbuf=0,procbuf=1,rows,columns,centrex,
            centrey,delay0,delay1,frames,i,j,k,l,loops,zero,data,
            divi,H_byte,L_byte,Port,cali,fout,done=0,cont;

float   h0,h1,VREF,th0,th1,pslope;

double  *aver,max,min,maxi,mini,zro,mc1,mc2,normal;

unsigned char    *Image1,*Image2,*Image3,*norm;

long             *average,*dv,*add1,*add2,t1,t2;

char             param1[length],param2[length],param3[length];


main()
{
 zero=127;
```

```c
infile1=fopen("param","r");
if(infile1==NULL){
 printf("Cannot open param file!\n");
 exit(1);
}
fscanf(infile1,"%*s %d %*s %d %*s %d %*s %d",&columns,&rows,
&centrex,&centrey);
fclose(infile1);
infile2=fopen("sub.par","r");
if(infile2==NULL){
 printf("Cannot open sub.par file!\n");
 exit(1);
}
fscanf(infile2,"%*s %g %*s %d %*s %g %*s %d
        %*s %g %*s %d %*s %d %*s %d %*s %d %*s %d %*s %d",
        &h0,&delay0,&h1,&delay1,&VREF,&frames,&loops,&divi,
        &cali,&fout,&cont);
fclose(infile2);
if(cali==1){
 infile3=fopen("commd","r");
 if(infile3==NULL){
  printf("Cannot open commd file!\n");
  exit(1);
 }
 fscanf(infile3,"%g",&pslope);
}
Port = 0x2C0;
th0=((float)delay0)/((float)1000);
```

```
th1=((float)delay1)/((float)1000);
aloc();
GlobalAlloc();
MdigReference(MilDigitizer,M_BRIGHTNESS_REF,135);
MdigReference(MilDigitizer,M_CONTRAST_REF,cont);
MdigControl(MilDigitizer, M_GRAB_MODE, M_ASYNCHRONOUS);
MdispSelect(MilDisplay,MilImageDisp);
delay(1000);
if(divi==1){
 divide();
 getch();
}
for(i=frames;i>0;--i){
 fieldapp(h0,h1);
 for(k=0;k<loops;++k){
    MdigGrab(MilDigitizer,MilImage);
    MdigGrab(MilDigitizer,MilImage);
    MdigGrabWait(MilDigitizer,M_GRAB_END);
    MbufCopy(MilImage,MilImageDisp);
    MgraArcFill(M_DEFAULT,MilImageDisp,575,25,5,5,0.0,360.0);
    MbufGet2d(MilImage,centrex,centrey,columns,rows,Image1);
    for(l=0;l<(rows*columns);++l)
      add1[l]+=(long)Image1[l];
 }
 fieldapp(-h0,-h1);
 for(k=0;k<loops;++k){
    MdigGrab(MilDigitizer,MilImage);
    MdigGrab(MilDigitizer,MilImage);
```

```
        MdigGrabWait(MilDigitizer,M_GRAB_END);

        MbufCopy(MilImage,MilImageDisp);

        MgraArcFill(M_DEFAULT,MilImageDisp,575,25,5,5,0.0,360.0);

        MbufGet2d(MilImage,centrex,centrey,columns,rows,Image2);

        for(l=0;l<(rows*columns);++l)

            add2[l]+=(long)Image2[l];

    }

    if(kbhit())

    if(getch()==27)

        i=0;

}

data =2048;

H_byte = data/256;

L_byte = data-H_byte*256;

outportb(Port+0, H_byte);

outportb(Port+1, L_byte);

if(divi==1){

    for(j=0;j<(rows*columns);++j){

        average[j]=(long)(add1[j]-add2[j]);

        aver[j]=(((((double)(average[j]))/((double)(2*dv[j])))+1)*zro;

    }

}

else{

    for(j=0;j<(rows*columns);++j){

        average[j]=(long)(add1[j]-add2[j]);

        aver[j]=(double)(average[j])/2.0;}

}

maxmin(aver,&max,&min);
```

```
normal=max-min;
for(j=0;j<(rows*columns);++j){
 norm[j]=(unsigned char)(((aver[j]-min)/(normal))*255+0.5);
}
MbufClear(MilImageDisp,0);
MbufPut2d(MilImageDisp,0,0,columns,rows,norm);
getch();
MbufAlloc2d(MilSystem,columns,rows,8L+M_UNSIGNED,
                  M_IMAGE+M_DISP,&MilImage2);
MbufCopyClip(MilImageDisp,MilImage2,0,0);
MbufExport("av",M_TIFF,MilImage2);
MbufClear(MilImageDisp,0);
daloc();
MbufFree(MilImage2);
MdispDeselect(MilDisplay,MilImageDisp);
GlobalDealloc();
outfile=fopen("history","a");
if((divi==1)){
 fprintf(outfile,
 "sub(%d,%d),h0=%g h1=%g,ac. max=%g ac. min=%g mm=%g,
              \n        zero=%g app. zero=%g\n",
 frames,loops,h0,h1,max,min,(max-min),zro,
              fabs((zro-min)/normal*255));}
else{
    fprintf(outfile,"sub(%d,%d),h0=%g h1=%g\n",frames,
loops,h0,h1);}
fclose(outfile);
if(cali==1){
```

```c
    outfile2=fopen("av","a");
    fprintf(outfile2,"#cali# %g %g %g %g\n",(max-min)/255,
                           pslope,min,zro);
    fclose(outfile2);
}
if((fout==1)&&(divi==1)&&(cali==1)){
 outfile3=fopen("av.n","w");
 for(i=0;i<rows;++i)
    for(j=0;j<columns;++j){
       fprintf(outfile3,"%g",(aver[j+i*columns]-zro)/pslope);
       if(j==(columns-1))
         fprintf(outfile3,"\n");
       else
       fprintf(outfile3,",");
         }
 fclose(outfile3);
 }
 if(done==1)
 printf("yes\n");
 return 0;
}
void GlobalAlloc(void)
{
 MappAlloc(M_DEFAULT,&MilApplication);
 MsysAlloc(M_DEF_SYSTEM_TYPE,M_DEFAULT,
                     M_DEFAULT,&MilSystem);
 MdigAlloc(MilSystem,M_DEFAULT,M_DEF_DIGITIZER_FORMAT,
                     M_DEFAULT,&MilDigitizer);
```

```
  MdispAlloc(MilSystem,M_DEFAULT,M_DISPLAY_SETUP,M_DEFAULT,
&MilDisplay);
  MbufAlloc2d(MilSystem,MdigInquire(MilDigitizer,M_SIZE_X,M_NULL),
                      MdigInquire(MilDigitizer,M_SIZE_Y,M_NULL),
   8L+M_UNSIGNED,M_IMAGE+M_GRAB+M_PROC,&MilImage);
  MbufAlloc2d(MilSystem,MdigInquire(MilDigitizer, M_SIZE_X, M_NULL),
                      MdigInquire(MilDigitizer, M_SIZE_Y, M_NULL),
       8L+M_UNSIGNED,M_IMAGE+M_GRAB+
                       M_PROC, &MilImage3[0]);
  MbufAlloc2d(MilSystem,
MdigInquire(MilDigitizer, M_SIZE_X, M_NULL),
MdigInquire(MilDigitizer, M_SIZE_Y, M_NULL),
8L+M_UNSIGNED,
M_IMAGE+M_GRAB+M_PROC, &MilImage3[1]);
  MbufAlloc2d(MilSystem,MdigInquire(MilDigitizer,M_SIZE_X,M_NULL),
MdigInquire(MilDigitizer,M_SIZE_Y,M_NULL),
8L+M_UNSIGNED,M_IMAGE+M_GRAB+
               M_PROC+M_DISP,&MilImageDisp);

}
void GlobalDealloc(void)
{
 MbufFree(MilImageDisp);
 MbufFree(MilImage);
 MbufFree(MilImage3[0]);
 MbufFree(MilImage3[1]);
 MdispFree(MilDisplay);
 MdigFree(MilDigitizer);
```

```c
 MsysFree(MilSystem);

 MappFree(MilApplication);

}

void aloc(void)

{

 Image1=calloc(rows*columns,sizeof(unsigned char));

 Image2=calloc(rows*columns,sizeof(unsigned char));

 Image3=calloc(rows*columns,sizeof(unsigned char));

 dv=calloc(rows*columns,sizeof(long));

 average=calloc(rows*columns,sizeof(long));

 aver=calloc(rows*columns,sizeof(double));

 add1=calloc(rows*columns,sizeof(long));

 add2=calloc(rows*columns,sizeof(long));

 norm=calloc(rows*columns,sizeof(unsigned char));

}

void daloc(void)

{

 free(Image1);

 free(Image2);

 free(Image3);

 free(average);

 free(aver);

 free(dv);

 free(norm);

 free(add1);

 free(add2);

}

void fieldapp(float hh0,float hh1)
```

```
{
 data = (hh0/VREF*2048)+2048;

 H_byte = data/256;

 L_byte = data-H_byte*256;

 outportb(Port+0, H_byte);

 outportb(Port+1, L_byte);

 imdis(hh0,hh1,th0);

 data = (hh1/VREF*2048)+2048;

 H_byte = data/256;

 L_byte = data-H_byte*256;

 outportb(Port+0, H_byte);

 outportb(Port+1, L_byte);

 imdis(hh0,hh1,th1);
}
void imdis(float hh0,float hh1,float tt)
{
 t1=biostime(CMD,0);

 t2=biostime(CMD,0);

 MdigGrab(MilDigitizer, MilImage3[grabbuf]);

 while((t2-t1)<=(tt*18.2)){

  if (grabbuf == 0) {

    grabbuf = 1;

    procbuf = 0;

  } else {

    grabbuf = 0;

    procbuf = 1;

  }

  MdigGrab(MilDigitizer, MilImage3[grabbuf]);
```

```c
if(hh0>0){
  sprintf(param1,"h0=+%g",hh0);
  sprintf(param2,"h1=+%g",hh1);
  sprintf(param3,"frame=%d",i);}
else{
  sprintf(param1,"h0=%g",hh0);
  sprintf(param2,"h1=%g",hh1);}
MgraText(M_DEFAULT,MilImage3[procbuf],550,5,param1);
MgraText(M_DEFAULT,MilImage3[procbuf],550,20,param2);
MgraText(M_DEFAULT,MilImage3[procbuf],550,35,param3);
MbufCopy(MilImage3[procbuf], MilImageDisp);
t2=biostime(CMD,0);
}
MdigGrabWait(MilDigitizer,M_GRAB_END);
}
void divide(void)
{
for(i=(frames);i>0;--i){
  for(k=0;k<(loops);++k){
    MdigGrab(MilDigitizer,MilImage);
    MdigGrab(MilDigitizer,MilImage);
    MdigGrabWait(MilDigitizer,M_GRAB_END);
    MbufCopy(MilImage,MilImageDisp);
    sprintf(param3,"frame=%d",i);
    MgraText(M_DEFAULT,MilImageDisp,550,35,param3);
    MbufGet2d(MilImage,centrex,centrey,columns,rows,Image3);
    for(l=0;l<(rows*columns);++l)
      dv[l]+=(long)Image3[l];
```

```
    }
  }
  for(i=0;i<(rows*columns);++i)
      zro+=((double)dv[i])/((double)(rows*columns*frames*loops));
}
void maxmin(double *hold,double *maxim,double *minim)
{
  *maxim=*minim=hold[0];
  for(j=0;j<(rows*columns);++j){
    if(hold[j]>*maxim)
        *maxim=hold[j];
    if(hold[j]<=*minim)
        *minim=hold[j];
  }
}
```

Appendix E

Visualizing program VG.C

field=1 Gauss
xvalue=298
yvalue=210
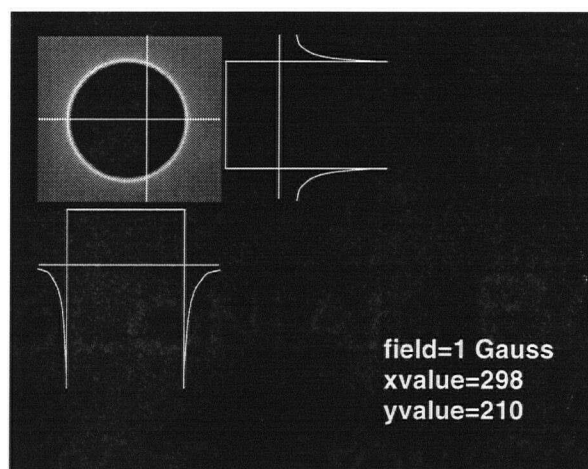
Figure E.1: Format of visualization program which reads special tiff files processed by the program SUBF.C. These files have appended parameters which are used by the visualization program to calculate field strengths for each point. Field points and their strengths can be easily found by simply moving a cursor to the point of interest with the mouse or arrow keys.

This program displays tiff images that have been processed by the program SUBF.C. The images can be seen in the upper left corner of the screen and the field intensity at which a cursor is placed along with its coordinates are indicated in the lower right corner of the screen and are displayed by typing d . The program is initiated by typing its name a space then the name of the tiff image file. The user also has the option of including a field strength value in Gauss after the tiff

150

file name for setting two field level indicator lines for comparison with the displayed x-y field profiles. The cross sectional lines can be controlled by either the computer mouse or through the keyboard arrow keys. The field values at the cursor point are calculated using the parameters of Eq.(2.1) appended to the end of each tiff file by the SUBF.C program. An image may also be displayed in reverse grey scale mode by typing r which causes the image and the indicated field strengths to be reversed.

E.1 Program VG.C

```c
#include <stdio.h>
#include <stdlib.h>
#include <math.h>
#include <mil.h>
#include <conio.h>
#include <dos.h>
#include <string.h>
#define IMAGE_DEPTH                 8L
#define length 20


MIL_ID MilApplication,
    MilSystem,
    MilDisplay,
    MilParentImage,
    MilImage,
    MilSubImage1,
    MilSubImage2,
    MilSubImage3,
    MilSrcSubImage;
```

```
void        mdriver(void);

void        sw(int);

double   d;

float       slope,pslope,acmin,aczro,intens;

int         rows,columns,yrows=0,xcolumns=0,incre=1,
              increx=1,increy=1,i,j,k=0,dd=0,dis=0,tog=0,flag=1,
              status1,status2,status3,TRUE=0,TRUE2=0,skip=0;

char       c1=0,c2=0,c3=0,param1[length],param2[length],
              param3[length];

unsigned   char linex[640],liney[480],*holder,C;

unsigned   port=0x2f8;


main(int argc,char **argv)
{
 FILE *infile,*infile2;
 long   KeyOnAlloc,       /* Enable keying on alloc          */
          KeyOnFree;       /* Disable keying on free           */

 KeyOnAlloc = M_DEF_DISPLAY_KEY_ENABLE_ON_ALLOC;
 KeyOnFree  = M_DEF_DISPLAY_KEY_DISABLE_ON_FREE;
 if(argc<2){
   printf("Usage: v <filename>\n");
   printf("Info: Program displays tiff files.\n");
   exit(1);
 }
 infile=fopen(argv[1],"rb");
 if(infile==NULL){
   printf("No such file %s\n",argv[1]);
```

```
  exit(1);

  }

rpt: while((C=fgetc(infile))!='#');

  if((fgetc(infile))!='c') goto rpt;

  if((fgetc(infile))!='a') goto rpt;

  if((fgetc(infile))!='l') goto rpt;

  if((fgetc(infile))!='i') goto rpt;

  if((fgetc(infile))!='#') goto rpt;

  fscanf(infile,"%g %g %g %g",&slope,&pslope,&acmin,&aczro);

  printf("%g %g %g %g\n",slope,pslope,acmin,aczro);

/*  aczro=acmin=0;

  pslope=slope=1;*/

  fclose(infile);

  if(argc==3){

d=strtod(argv[2],NULL);

dd=(int)d;

        dd=(dd*pslope+aczro-acmin)/slope;

  }

  MappAlloc(M_DEFAULT,&MilApplication);

  MsysAlloc(M_SYSTEM_METEOR,M_DEFAULT,M_DEFAULT,

                  &MilSystem);

  MdispAlloc(MilSystem,M_DEFAULT,"1280x1024x8PP",M_DEFAULT,

&MilDisplay);

  MbufDiskInquire(argv[1],M_SIZE_X,&columns);

  MbufDiskInquire(argv[1],M_SIZE_Y,&rows);

  holder=calloc(rows*columns,sizeof(unsigned char));

   /* Allocate a two-dimensional, displayable image buffer. */

  MbufAlloc2d(MilSystem,1280,1024,IMAGE_DEPTH+M_UNSIGNED,
```

```
                M_IMAGE+M_DISP+M_PROC, &MilParentImage);
      /* Allocate two child buffers from the displayable parent buffer. */
      MbufChild2d(MilParentImage, OL, OL, columns, rows,
                              &MilSrcSubImage);
      MbufChild2d(MilParentImage,columns,0,256,rows,&MilSubImage1);
      MbufChild2d(MilParentImage,0,rows,columns,256,&MilSubImage2);
      MbufChild2d(MilParentImage,740,740,260,125,&MilSubImage3);
      MbufAlloc2d(MilSystem,columns,rows,IMAGE_DEPTH+
              M_UNSIGNED,M_IMAGE+M_DISP+M_PROC,&MilImage);
    /* Clear the parent buffer. */
      MbufClear(MilParentImage, OL);
     /* Display the parent buffer. */
      MdispSelect(MilDisplay, MilParentImage);
      /* Load the entire source image into the source sub-image buffer. */
      MbufLoad(argv[1], MilImage);
      MbufGet(MilImage,holder);
      MbufCopy(MilImage,MilSrcSubImage);
      MgraLine(M_DEFAULT,MilSrcSubImage,
      0,(int)(rows/2)+yrows,columns-1,(int)(rows/2)+yrows);
      MgraLine(M_DEFAULT,MilSrcSubImage,
(int)(columns/2)+xcolumns,0,(int)(columns/2)+
                  xcolumns,rows-1);
      MbufGet2d(MilImage,0,(int)(rows/2)+yrows,columns,1,linex);
      MbufClear(MilSubImage2,0);
      MgraLine(M_DEFAULT,MilSubImage2,0,dd,columns,dd);
      for(j=2;j<columns;j+=2)
        MgraLine(M_DEFAULT,MilSubImage2,
            j-2,(long)((linex[j-2])),j,(long)((linex[j])));
```

```
MbufGet2d(MilImage,(int)(columns/2)+xcolumns,0,1,rows,liney);
MbufClear(MilSubImage1,0);
MgraLine(M_DEFAULT,MilSubImage1,dd,0,dd,rows);
for(j=2;j<rows;j+=2)
    MgraLine(M_DEFAULT,MilSubImage1,
(long)((liney[j-2])),j-2,(long)((liney[j])),j);
MgraFontScale(M_DEFAULT,2,2);
while(c1!=27){
    MbufGet2d(MilImage,0,(int)(rows/2)+yrows,columns,1,linex);
    MbufGet2d(MilImage,(int)(columns/2)+xcolumns,0,1,rows,liney);
    MbufCopy(MilImage,MilSrcSubImage);
    if((!skip)){
      MgraLine(M_DEFAULT,MilSrcSubImage,
      0,(int)(rows/2)+yrows,columns-1,(int)(rows/2)+yrows);
      MgraLine(M_DEFAULT,MilSrcSubImage,
      (int)(columns/2)+xcolumns,0,(int)(columns/2)+xcolumns,rows-1);
    if(((c3==72)||(c3==80)||(c1==114))){
      MbufClear(MilSubImage2,0);
      MgraLine(M_DEFAULT,MilSubImage2,0,dd,columns,dd);
      for(j=2;j<columns;j+=2)
        MgraLine(M_DEFAULT,MilSubImage2,j-2,(long)((linex[j-2])),j,
            (long)((linex[j])));
     }
    if(((c2==77)||(c2==75)||(c1==114))){
      MbufClear(MilSubImage1,0);
      MgraLine(M_DEFAULT,MilSubImage1,dd,0,dd,rows);
      for(j=2;j<rows;j+=2)
        MgraLine(M_DEFAULT,MilSubImage1,(long)((liney[j-2])),j-2,
```

```c
                       (long)((liney[j])),j);
                    }
                 }
              else{
                 MgraLine(M_DEFAULT,MilSrcSubImage,(int)(columns/2)
                          +xcolumns-2,(int)(rows/2)+yrows,(int)(columns/2)
                          +xcolumns+2,(int)(rows/2)+yrows);
                 MgraLine(M_DEFAULT,MilSrcSubImage,(int)(columns/2)
                          +xcolumns,(int)(rows/2)+yrows-2,(int)(columns/2)
                          +xcolumns,(int)(rows/2)+yrows+2);
              }
              if(dis==1){
                 intens=(slope*liney[(int)(rows/2)+yrows]+acmin-aczro)/pslope;
                 sprintf(param1,"field=%4d Gauss",(int)intens);
                 sprintf(param2,"xvalue=%3d",(int)(columns/2)+xcolumns);
                 sprintf(param3,"yvalue=%3d",(int)(rows/2)+yrows);
                 MgraText(M_DEFAULT,MilSubImage3,1,0,param1);
                 MgraText(M_DEFAULT,MilSubImage3,1,40,param2);
                 MgraText(M_DEFAULT,MilSubImage3,1,80,param3);
              }
              c1=c2=c3=0;
              skip=0;
              status1=inportb(port);
              while(!TRUE){
               TRUE=kbhit();
               mdriver();
              }
              if(!TRUE2)
```

```
                  c1=getch();
if(c1==100){
 dis=1-dis;
}
if((c1==100)&&(dis==0))
 MbufClear(MilSubImage3,0);
if(c1==114){
 for(i=0;i<(rows*columns);++i)
    holder[i]=255-holder[i];
MbufPut(MilImage,holder);
}
 if(c1==0){
 if(!TRUE2){
  c2=getch();
  sw(c2);
  c3=c2;
 }
 else{
  sw(c2);
  sw(c3);
 }
}
switch(c1){
 case 105:{
  ++incre;
 }
 break;
 case 9:{
```

```
            if(incre>1)

                  --incre;

            }

break;

 }

   TRUE=0;

   TRUE2=0;

   increx=incre;

   increy=incre;

 }

  MdispDeselect(MilDisplay, MilParentImage);

 /* Free all allocations. */

  free(holder);

  MbufFree(MilImage);

  MbufFree(MilSubImage1);

  MbufFree(MilSubImage2);

  MbufFree(MilSubImage3);

  MbufFree(MilSrcSubImage);

  MbufFree(MilParentImage);

  MdispFree(MilDisplay);

  MsysFree(MilSystem);

  MappFree(MilApplication);

  return 0;

}

void mdriver(void)

{

 if((status1==96)||(status1==108)||

 (status1==99)||(status1==111)||
```

```
        (status1==64)||(status1==76)||
        (status1==79)||(status1==67)){
         status2=inportb(port);
         while(status2==status1)
            status2=inportb(port);
         status3=inportb(port);
         while((status3==status2)&&(flag)){
            if(k>4000)
               flag=0;
               status3=inportb(port);
               ++k;
             }
            flag=1;
            k=0;
         if((status2<64)&&(status3<64)){
           c1=0;
           switch(status1){
         case 96:{
             if((increx=(int)(status2*1.2))!=0)
c2=77;
             if((increy=(int)(status3*1.2))!=0)
c3=80;
             if((status2==0)&&(status3==0)){
c2=77;
c3=80;
               }
            }
            break;
```

```
      case 64:{
        if((increx=(int)(status2*1.2))!=0)
          c2=77;
        if((increy=(int)(status3*1.2))!=0)
          c3=80;
        if(!((status1==64)&&(status2==0)&&(status3==0)))
skip=1;
        }
        break;
        case 99:{
        if((increx=(int)((64-status2)*1.2))!=0)
          c2=75;
        if((increy=(int)(status3*1.2))!=0)
          c3=80;
        }
        break;
        case 67:{
        if((increx=(int)((64-status2)*1.2))!=0)
          c2=75;
        if((increy=(int)(status3*1.2))!=0)
          c3=80;
          skip=1;
}
        break;
        case 108:{
        if((increx=(int)(status2*1.2))!=0)
          c2=77;
        if((increy=(int)((64-status3)*1.2))!=0)
```

```
                c3=72;
        }
        break;
        case 76:{
        if((increx=(int)(status2*1.2))!=0)
        c2=77;
        if((increy=(int)((64-status3)*1.2))!=0)
            c3=72;
            skip=1;
        }
        break;
        case 111:{
        if((increx=(int)((64-status2)*1.2))!=0)
            c2=75;
        if((increy=(int)((64-status3)*1.2))!=0)
            c3=72;
        }
        break;
        case 79:{
        if((increx=(int)((64-status2)*1.2))!=0)
            c2=75;
        if((increy=(int)((64-status3)*1.2))!=0)
            c3=72;
            skip=1;
        }
        break;
    }
TRUE=1;
```

```c
    TRUE2=1;
  }
}
status1=inportb(port);
}
void sw(int cc)
{
 switch(cc){
  case 72:{
  if((yrows-increy)>(-(rows-1)/2))
     yrows-=increy;
  else
     yrows=-rows/2;
  }
  break;
  case 75:{
       if((xcolumns-increx)>(-(columns-1)/2))
         xcolumns-=increx;
       else
         xcolumns=-columns/2;
  }
  break;
  case 80:{
  if((yrows+increy)<((rows+1)/2))
     yrows+=increy;
  else
     yrows=(int)((rows-0.5)/2);
  }
```

```
  break;
  case 77:{
  if((xcolumns+increx)<((columns+1)/2))
    xcolumns+=increx;
  else
    xcolumns=(int)((columns-0.5)/2);
  }
  break;
 }
}
```

Bibliography

[1] H. Kamerlingh Onnes, *Leiden Comm.* **120b,122b,124c**, (1911).

[2] J. G. Bednorz, and K. A. Müller, *Z. Phys.* **B64**, 189 (1986).

[3] H. Träuble, and U. Eßmann, *Phys. Status Solidi* **18**, 813 (1966).

[4] E. H. Brandt, and U. Eßmann, *Phys. Status Solidi b* **144**, 13 (1987).

[5] P. L. Gammel, D. J. Bishop, G. J. Dolan, J. R. Kwo, C. A. Murray, L. F. Schneemeyer, and J. V. Waszczak, *Phys. Rev. B* **36** 2592 (1987).

[6] L. Ya. Vinnikov, L. A. Gurevich, G. A. Emelchenko, and Yu. A. Ossipyan, *Solid State Commun.* **67** 421 (1988).

[7] H. F. Hess, R. B. Robinson, R. C. Dynes, J. M. Valles, and J. V. Waszczak, *Phys. Rev. Lett.* **62** 214 (1989).

[8] H. F. Hess, C. A. Murray, and J. V. Waszczak, *Phys. Rev. Lett.* **69** 2138 (1992).

[9] P. Leiderer, P. Brüll, T. Klumpp, and B. Stritzker, *physica B* **165 & 166** 1387 (1990).

[10] A. M. Chang, H. D. Hallen, H. F. Hess, H. L. Kao, J. Kwo, A. Sudbo, and T. Y. Chang, *Europhys. Lett.* **20** 645 (1992).

[11] Z. Koziol, Z. Tarnawski, and J. J. M. Franse, *Solid State Commun.* **85** 991 (1993).

[12] D. A. Brawner, and N. P. Ong, *J. Appl. Phys* **73** 3890 (1993).

[13] M. Faraday em Phil. Trans. **136** 1 (1846).

[14] P. B. Alers, *Phys. Rev.* **105** 104 (1957).

[15] E. Batalla, E. G. Zwartz, R. Goudreault, and L. S. Wright, *Rev. Sci. Intrum.* **61** 2194 (1990).

[16] H. Kirchner, *Phys. Lett.* **30A** 437 (1969).

[17] M V. Indenbom, V. I. Nikitenko, A. A. Polyanskii, and V. K. Vlasko-Vlasov, *Cryogenics* **30** 747 (1990).

[18] L. A. Dorosinskii, M. V. Indenbom, V. I. Nikitenko, Yu. A. Ossip'yan, A. A. Polyanskii, and V. K. Vlasko-Vlasov, *Physica C* **203** 149 (1992).

[19] A. A. Polyanskii, V. K. Vlasko-Vlasov, M. V. Indenbom, and V. I. Nikitenko, *Pis'ma v JTF* **15** 1 (1989).

[20] M. R. Koblischka, and R. J. Wijngaarden, *Supercond. Sci Technol.* **8** 199 (1995).

[21] E. Zeldov, A. I. Larkin, V. B. Geshkenbein, M. Konczykowski, D. Majer, B. Khaykovich, V. M. Vinokur, and H. Shtrikman, *Phys. Rev. Lett.* **73** 1428 (1994).

[22] M. W. Gardner, S. A. Govorkov, R. Liang, D. A. Bonn, J. F. Carolan, and W. N. Hardy, *J. Appl. Phys.* **83** 3714 (1998).

[23] P. N. Mikheenko, and Yu. E. Kuzovlev, *Physica C* **204** 229 (1993).

[24] Ch. Jooss, R. Warthmann, A. Forkl and H. Kronmüller, *Physica C* **299** 215 (1998).

[25] S. A. Govorkov, *Private communication.*

[26] P. D. Grant, M. W. Denhoff, W. Xing, P. Brown, S. Govorkov, J. C. Irwin, B. Heinrich, H. Zhou, A. A. Fife, and A. R. Cragg, *Physica C* **229** 289 (1994).

[27] R. J. Wijngaarden, H. J. W. Spoelder, R. Surdeanu, and R. Griessen, *Phys. Rev. B* **54** 6742 (1996).

[28] W. H. Press, B. P. Fannery, S. A. Teukolsky, and W. T. Vetterling, *Numerical Recipes In C*, Cambridge University Press, pp. 54 (1989).

[29] R. Liang, P. Dosanjh, D. A. Bonn, D. J. Barr, J. F. Carolan, and W. N. Hardy, *Physica C* **195** 51 (1992).

[30] R. Liang, D. A. Bonn, and W. N. Hardy, *Phys. Rev. Lett.* **76** 835 (1996).

[31] V. K. Vlasko-Vlasov, L. A. Dorosinkii, A. A. Polyanskii, and V. I. Nikitenko, *Phys. Rev. Lett.* **72** 3246 (1994).

[32] Th. Schuster, M. V. Indenbom, M. R. Koblishka, H. Kuhn, and H. Kronmüller, *Phys. Rev. B* **49** 3443 (1994).

[33] K. E. Gray, R. T. Kampwirth, and D. E. Farell, *Phys. Rev. B* **41** 819 (1990).

[34] C. P. Bean, *Phys. Rev. Lett.* **8** 250 (1962).

[35] Y. B. Kim, C. F. Hempstead, and A. R. Strnd, *Phys. Rev. Lett.* **9** 306 (1962); Y. B. Kim, C. F. Hempstead, and A. R. Strnd, *Phys. Rev.* **129** 528 (1963).

[36] M. Xu, D. Shi, and R. F. Fox, *Phys. Rev. B* **42** 10773 (1990).

[37] W. A. Fietz, M. R. Beasley, J. Silcox, and W. W. Webb, *Phys. Rev.* **136** A335 (1964).

[38] H. A. Radovan, H. H. Wen, and P. Ziemann, *Eur. Phys. J.* B **7** 533-540 (1999).

[39] W. E. Lawrence and, S. Doniach, in E. Kanda (ed.), *Proc. 12th Int. Conf. Low Temp. Phys.*, Kyoto, Japan 361 (1970).

[40] M. Tinkham, *Introduction To Superconductivity* 2n ed. Chap 9, pp. 320. (1996).

[41] D. E. Farrell, J. P. Rice, D. M. Ginsberg, and J. K. Liu, *Phys. Rev. Lett.* **64** 1573 (1990).

[42] J. R. Clem, *Phys. Rev. B* **43** 7837 (1991).

[43] J. R. Clem, *Supercond. Sci. Technol.* **11** 909 (1998).